Development of Wideband Circularly Polarized Antennas for Remote Sensing Microsatellite

January 2018

Asif Awaludin

Graduate School of Advanced Integration Science
CHIBA UNIVERSITY

Submitted in partial fulfillment of the requirements for the degree of
Doctor of Engineering

(千葉大学学位申請論文)

Development Of Wideband Circularly Polarized Antennas For Remote Sensing Microsatellite

超小型リモートセンシング衛星用広帯域円偏波アンテナの開発

2018 年 2 月

Asif Awaludin

アシフ アワルディン

千葉大学大学院融合科学研究科

情報科学専攻 知能情報コース

Abstract

Chiba University is developing the GAIA–I microsatellite which makes use of the Global Navigation Satellite System (GNSS) Radio Occultation (RO) and the Electron Density – Temperature Probe (EDTP) sensors. The mission is to provide global coverage vertical resolution of pressure, temperature, refractivity, and water vapor in the atmosphere, also electron temperature and density in the ionosphere. The atmospheric parameters data will be used in numerical weather prediction (NWP) for climate modeling, while the ionospheric data will be beneficial to investigate the relationship between global land deformation and the electron density.

In this research, two novel methods to generate wideband circularly polarized (CP) based on equilateral triangular ring slot (ETRS) antenna for the GNSS–RO receiver and command communication satellite of the GAIA–I are proposed. The first method is the introduction of a pair of slits to improve the CP bandwidth of equilateral triangular slot (ETS) antenna which technically is a wide slot but employs the ring slot CP excitation technique thanks to the basic shape. The small size antennas introduce chamfered corners, triangular perturbation patch and feed line with additional branches to produce wideband CP operation. A further 3–dB ARBW improvement close to its impedance bandwidth is obtained by attaching a pair of slits. It can be confirmed that the pair of slit has a significant impact to double the 3-dB ARBW and decrease the antenna size. A study on several parameters influencing the shape transformations to the impedance and axial ratio bandwidth is presented. The designed ETS antennas for both applications are fabricated to verify the simulated results. The measured antenna for communication satellite presents good agreement with the simulated one by presenting CP bandwidth of 52%. Meanwhile, the measured design for the GNSS–RO receiver performs 3–dB ARBW of 41.6%. A truncated cone reflector manufactured using 3D printer

offers unidirectional radiation pattern for the proposed antenna and improves the performance by delivering a maximum gain of 11.9 dBic.

The second method is the insertion of two diagonal line slots to improve CP bandwidth of ETS antenna. In this second antenna type, the linearly polarized (LP) ETRS is converted to circular by truncating only two slot corners and attaching grounded perturbation patch. Since technically become a wide slot, it is then referred as ETS as well. However, it performs smaller 3-dB ARBW than its reflection coefficient bandwidth. Thus, an improvement is required to equalize both bandwidths. For this purpose, the two diagonal line slots are introduced on the left and right side of ETS. The length of both line slots related to the lowest and highest CP frequencies of the ETS. The two diagonal line slots significantly enhanced CP bandwidth of ETS antenna to 680 MHz or 37% fractional bandwidth. They also enhance the RHCP gain with a recorded average is around 4.9 dBic. The measured performances of x–z and y–z plane radiation patterns verify the bi-directional radiation pattern and show good achievement on CP operation.

概要

千葉大学では、全球測位衛星システム掩蔽（GNSS-RO）搭載の超小型衛星GAIA-Iを開発している。このミッションの目的は、中性大気中の温度、圧力、屈折率、水蒸気の垂直プロファイル、電離層の電子密度を全球範囲で観測することである。本研究ではGAIA-IのGNSS-RO観測及び通信システム用の広帯域円偏波（CP）を生成する正三角形リングスロット（ETRS）アンテナの性能向上のため、2つの新規手法を提案した。第一は、正三角形スロット（ETS）アンテナのCP帯域幅を広帯域化するために、スリット、またはリングスロットアンテナによるCPアンテナを提案したことである。アンテナの測定結果は52％のCP帯域幅を示し、シミュレーション結果と一致した。一方、GNSS-RO用のアンテナのバンド幅は41.6％を得た。また、このアンテナに円錐反射器を取り付けると、最大利得11.9dBicに性能改善ができた。第二は、2つの対角線スロットの挿入によってETSアンテナのCP帯域幅の改善ができたことである。ここで、直線偏波（LP）のアンテナの2つのスロットコーナーと、接地された摂動パッチの導入によって円偏波アンテナの特性改良をした。さらに、2つの対角ラインスロットをアンテナの左右に配置して特性改善をした。この二本の対角線スロットで37％の帯域幅を取得して、ETRSアンテナの3dB 軸比帯域幅（ARBW）の改善を示した。また、放射パターンの測定結果は双方向放射で、その3dB　ARBW内で良好なCP性能を有した。本研究においてGNSS-ROと通信システム用の広帯域CPを確立した点は、今後の電離層観測用の小型衛星開発において極めて大きな意義をもつ。

Contents

List of Tables

List of Figures

Chapter 1

Introduction

1.1 Motivation and Objectives

Josaphat Microwave Remote Sensing Laboratory (JMRSL) is conducting research on the development of the GAIA–I microsatellite which makes use of the GNSS–RO and the EDTP sensors [SSI15]. The mission is to provide global coverage vertical resolution of precipitable water (PW) and temperature in the neutral atmosphere, and also the ionospheric electron density and temperature. The atmospheric parameters data will support numerical weather prediction (NWP) for research in climate modeling, while the ionospheric data will be beneficial to investigate the relationship between global land deformation and the electron density. The GNSS–RO measures the paths along with propagation velocity of L–band radio frequency signals emitted by the GNSS satellites which pass and refracted through the atmosphere [YFC$^+$10].

The GNSS–RO remote sensing sensor requires a CP antenna working at 1150–1300 MHz and 1559–1611 MHz to receive the intended signals. Considering

the frequency span, this antenna can be developed as a single wideband or a dual–band. Various CP antennas designed for the GNSS receivers are six–turns equiangular spiral incorporated with ground [IGB10], helix antenna with the bifilar design [SR14], and slot antenna having annular–ring shape perturbed by hat–shaped disturbance [SC11]. Some dualband antennas are also reported for the GNSS receiver such as stacked–patch fed by a branch line hybrid incorporated with proximity probes [IGB10] and dual connected probes in parallel attached on a microstrip antenna [SZL15]. Meanwhile, the GAIA–I communication system also adopts a CP antenna for its command system. Several CP antennas have been presented for a communication system in S-band such as helix with the quadrifilar design [GGTC12], [GLZ14], spiral with conical shape [Hus12], and antenna with isoflux pattern[CLLL14], [CLL13].

A printed slot antenna has many advantages than the above–mentioned types for a space-based application which demands low profile, light, and CP bandwidth more than 33% of the center frequency. According to its feeding method, printed slot antenna has two main categories, coplanar waveguide (CPW) feed with its wider bandwidth and microstrip–line feed with its better gain. The first type is classified into wide and ring slot. Generally, a ring slot offers smaller bandwidth compared with a wide slot, but provide a more compact size. However, by enlarging the slot size, the 3–dB ARBW can be improved as much the wide slot. It is reported that a slot antenna with annular–ring shape possessing a slot size of $0.068\lambda_0$ and a hat–shaped perturbation fabricated on an RT5880 laminate successfully reaches CP bandwidth of 65% at 1638 MHz center frequency[SC11]. A slot antenna with square-ring design presenting a slot size of $0.02\lambda_0$ printed on an FR4 laminate manages to gain CP bandwidth of 6.3% at a center frequency of 1630 MHz [RW08]. On the other hand, more extensive 3–dB ARBW (68%) is performed by a CPW–fed wide slot antenna

with symmetric–aperture [NCQ11]. It is also presented that a CPW–fed antenna with square slot design and three inverted–L–shape fragments secure CP bandwidth of 86.4% [FNGP11].

Meanwhile, only few printed wide slot antennas for wideband CP application use equilateral triangular shape. One of them is an ETS antenna excited by an L–shaped fragment feeding performs CP bandwidth of 3.2% [HCR08]. 3-dB ARBW enhancement is obtained by bringing up its inner triangular patch which then becomes a parasitic patch for a wide slot performing the CP bandwidth of 31%. However, a bulky dimension and fragile construction are the drawbacks. It had been reported also a coplanar waveguide fed ETRS antenna makes use of a stub for impedance matching cannot achieve a CP radiation [CCR05].

Basically, a ring slot without modification presents a linear polarization (LP) operation. Transformation of its polarization to circular can be conducted by introducing several modifications, for example, an insertion of a disturbance patch into the slot incorporated with a lopsided feed line [SC11], [WHC02]. A conjunction of two ring slots [CL11] and the use of stripline hybrid coupler as a feed line [QC99] produce similar alteration. In a similar way, the application of a slit delivers small 3–dB ARBW. As being reported, a slit introduced into an annular–ring slot fed by a curved feed line produces CP operation [SHHO07] with less than 10% 3–dB ARBW. Introduction of two slits to an annular–ring patch has produced less than 1% 3–dB ARBW [CW99]. Additionally, there is no report on the implementation of the slit in improving 3-dB ARBW of a slot antenna. Meanwhile, an asymmetrical dipole fed by microstrip feed line completed with a slit projected on the center of feed line [BAM10] has presented CP bandwidth of 23%.

The aim of this research is to present a novel ETS antenna design by transforming a conventional ETRS to present a wide CP operation which meets requirements of the GNSS–RO sensor and command communication system of GAIA–I. The antennas must be low profile and have CP bandwidth similar to those in [SC11], [NCQ11]. Since the conventional ETRS offers small bandwidth [HCR08], the initial bandwidth improvement can be produced by increasing the slot size, delivering wider bandwidth comparable to the wide slot. To generate CP operation, some techniques implemented to a ring slot are applied, for example truncating each corner of ETS, inserting grounded disturbance patch, and deforming the feed line. As a consequence of the large slot size, these methods diminishing the impact of the inner triangular patch to the antenna performance lead to the transformation of ETRS antenna from a ring slot to a wide slot. Therefore they are called ETS antenna. Since the geometry of the antenna is different from antenna with a square or annular–ring mentioned in [SC11], [WHC02], the chamfered parts and the disturbance form that enhance CP performance needs to be investigated. To modify the feed line, a transformed feed line with several deformations to improve the CP radiation is preferred than an L-shaped strip line applied [HCR08]. The novel method proposed in this research which significantly improves CP bandwidth is the introduction of a pair slits with equal length into the transformed ETS. This structure delivers gain enhancement and performs unidirectional radiation thanks to 3D printed truncated cone ground plane.

1.2 Contributions

The contributions of this research to the related topics are summarised as follows:

- We have designed and developed a novel method to widen CP bandwidth of an ETS antenna to achieve coverage of GNSS frequencies by making use of a pair of slits incorporated with three truncated corners and grounded perturbation.
- We have designed and developed novel method to broaden the CP bandwidth of an ETS antenna to achieve coverage of GNSS frequencies by making use of diagonal line slots incorporated with two truncated corners and grounded perturbation.
- We have designed and developed technique to enhance the gain of a wideband CP antenna that exceeds the performance of conventional metal reflector and close to required GNSS antenna gain.
- We have measured the performance of the developed antennas and compared to the simulated results which show good agreement even though several weaknesses were founded.

1.3 Outline

This thesis is presented in five chapter as described below:

- Chapter 2 provides the background information and context related to the materials discussed in the subsequent chapters. This covers a de-

scription of GAIA-I microsatellite and its GNSS–RO sensor including the CP printed slot antenna.

- Chapter 3 presents the several methods to generate wideband CP antenna for GNSS. Gain improvement of the wideband antenna is also presented.

- Chapter 4 describes the experimental setup and measurement results of the presented antenna.

- Chapter 5 draws the conclusion and further research.

Chapter 2

Background and Related Works

2.1 GNSS Radio Occultation

The operational of GNSS, such as GPS, Galileo, Glonas, and Beidou, have given a great contribution to the observation of atmospheric parameters. Initially, ground-based GNSS receivers have been installed to build a geodetic ground network which provides an abundant quantity of perceptible water (PW) data useful for NWP. These observation results contribute significantly to weather and climate modeling. However, there is a drawback and also challenge as the vertical profile of the data cannot be produced and the coverage is limited to the GNSS network area. Therefore, space-based observation is required as a supporting solution [YFC+10].

RO offers a sounding method in which an electromagnetic wave transmitted from a satellite goes over an impending planetary atmosphere then reaches the receiver, and is employed to observe the atmospheric parameters of the planet. In this case, the atmosphere will refract the track and propagation

velocity of the wave due to the variation of refractive index on it. This technique can be implemented to observe earth's atmosphere including ionosphere by utilizing refracted radio frequency signals transmitted from GNSS received by an occulting GNSS–RO satellite orbiting in low earth orbit, as illustrated in Fig. 2.1. Since the path of the signal is bent and arrival time is delayed, the highly accurate phase and magnitude measurement of the signals can be calculated to obtain precise retrieval of the vertical resolution of the atmospheric refractive index. As a result, the atmospheric parameters such as temperature, humidity, air density, and pressure can be achieved. The bending angle caused by ionospheric refraction can be used to obtain total electron content (TEC) and ionosphere inversion [JCX13].

The refractivity at the occultation tangent point n(a) has a relation with impact parameter a (as depicted in Fig. 2.1). α is the bending angle due to the refractivity variation in the atmosphere. Bouguers formula, Equation 2.1, expresses the relationship between bending angle and refractive index profile, considering spherical symmetry near the tangent point [MAM+08].

$$\alpha(a) = -2a \int_0^\infty \frac{1}{\sqrt{a'^2 - a^2}} \frac{d\ln(n(a'))}{da'} da' \tag{2.1}$$

The Abel transform, as explained by Equation 2.2, can be used to get vertical profiles of refractive index versus impact parameter.

$$\ln(n(a)) = \frac{1}{\pi} \int_0^\infty \frac{\alpha(a')}{\sqrt{a'^2 - a^2}} da' \tag{2.2}$$

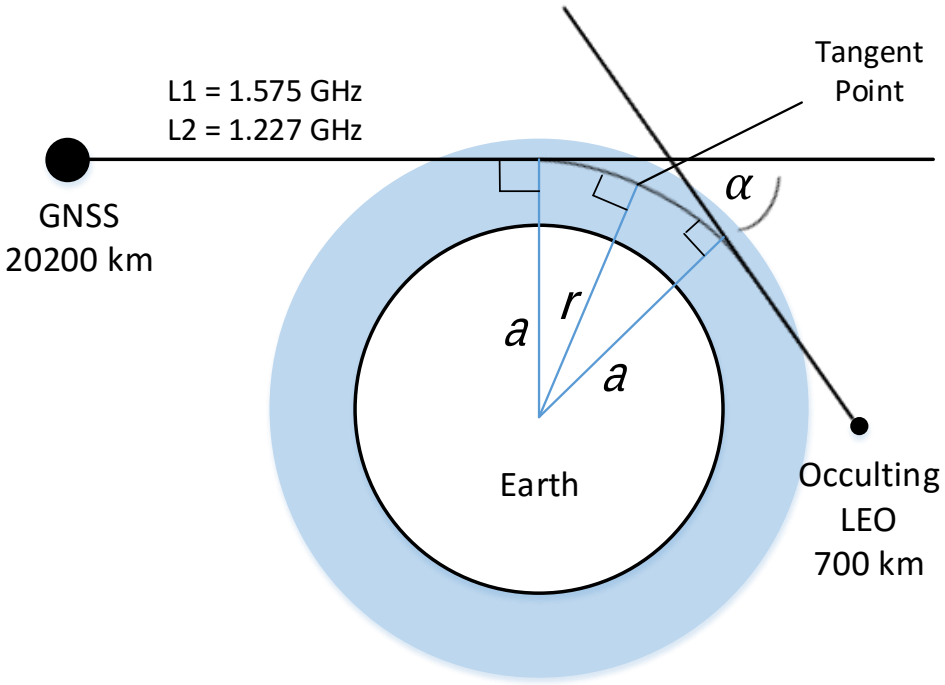

Figure 2.1: Illustration of GNSS–RO remote sensing. The COSMIC (LEO satellite) receives refracted radio frequency signals from the GPS

Refractivity N, equal to $(n-1)10^6$, is related to the pressure P (mbar), temperature T and water vapor partial pressure P_{w} (mbar) according to the Equation 2.3.

$$N = a_1 \frac{P}{T} + a_2 \frac{P_w}{T} \tag{2.3}$$

where a1 and a2 are constants (a1 = 77.6 K/mbar; a2 = 3.73x10^5 K^2/mbar). Geometrical calculations are performed to compute the profile altitude at each impact parameter, based on highly accurate (cm–level) orbits of the GPS satellites and LEO. By using the calculated refractivity, each temperature and pressure profiles are derived assuming hydrostatic equilibrium [MAM+08].

There are several satellites have been launched to do GNSS–RO mission, such as the GPS/MET (1995-1997), the Ørsted (1999), the SUNSAT (in 1999), the SAC-C (2001), the GRACE (2002), METOP/B (2006), FORMOSAT-3/COSMIC (2006), FORMOSAT-7/COSMIC-II (2016) [YFC+10, JCX13]. Since some of them have ended their mission, therefore the launch of new GNSS-RO satellites are on demand to maintain and improve their significant contributions.

2.2 GAIA-I Microsatellite Development

The GNSS–RO remote sensing technique has become a powerful method for measuring the atmosphere with high precision, accuracy, and vertical resolution. It offers a compact, low-power, and low-cost sensor that can operate in all weather condition and over both land and ocean and with long-term stability [AEH+08]. The mission is to persistently archive ionospheric and tropospheric data as a support for operational daily weather forecasts, investigating climate, and studying space weather.

Chiba University through Josaphat Microwave Remote Sensing Laboratory (JMRSL) is conducting research on the GAIA–I development to increase the number of GNSS–RO soundings contributing atmospheric research, operational weather prediction, and study of the relation between the global land deformation and the ionospheric electron density. The GAIA–I payload is equipped with GNSS–RO sensor to detect the refracted signals emitted by navigational satellites such as GPS (altitude 19,300 km), Galileo (24,000 km), GLONASS (19,100 km), Quasi–Zenith Satellite (QZS, 35,786 km) which will start it service start from 2018, and telecommunication satellite O3B (Ka–

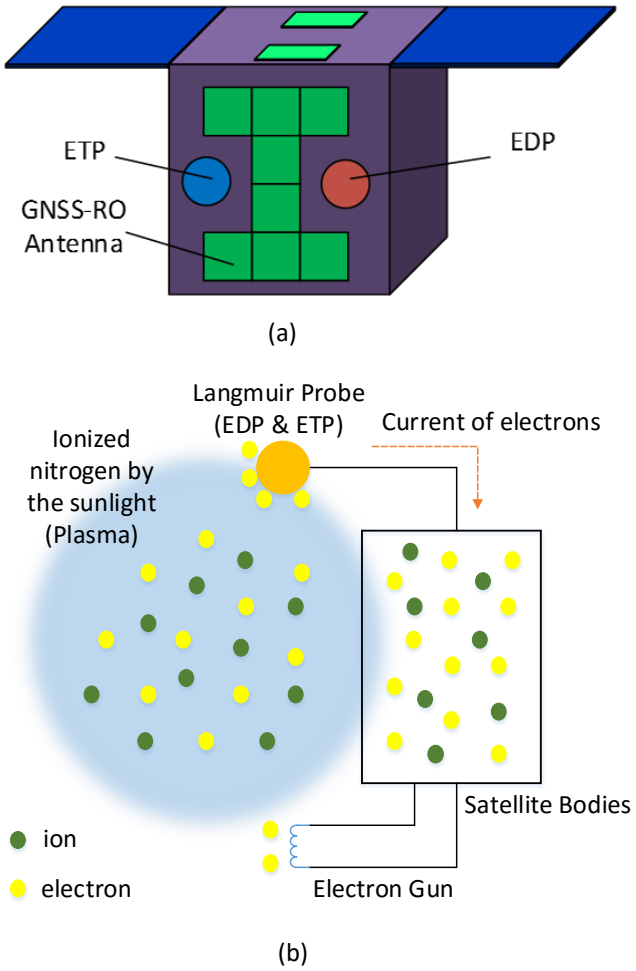

Figure 2.2: The GAIA-I microsatellite and its sensors (a) Design of GAIA-I microsatellite with GNSS–RO Antenna, EDP and ETP, (b) Langmuir probe for EDP and ETP sensors [SSI15][MSSA+16].

band, 8,063km). The received data is processed by implementing occultation method to derive earth gravity, atmospheric neutron distribution, ionospheric electron density, and atmospheric parameters such as pressure, temperature, humidity, and water vapor. Beside the GNSS, the GAIA–I is planned also to receive Ka–band signal of O3b communication satellite to increase the number of RO observation. The satellite also makes use of EDTP sensor to conduct in situ measurement of electron density and its temperature which useful for validation of GNSS–RO sensor and monitoring ionosphere parameter along the

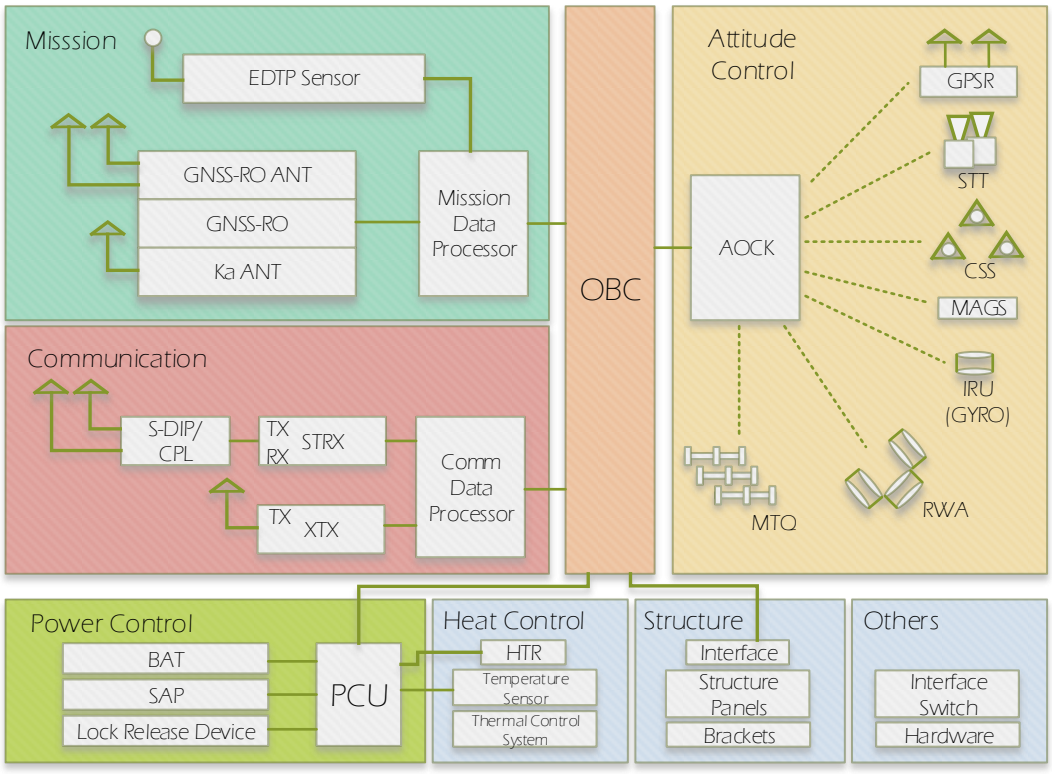

Figure 2.3: Structure of GAIA-I microsatellite system[SSI15].

orbit. The EDTP sensor is developed base on Langmuir probe by integrating Electron Density Probe and Electron Temperature Probe into a compact sensor unit controlled by FPGA [SSI15]. The Langmuir probe is excited with a triangular wave to attract ions and electrons from plasma in the ionosphere. The calculated current of electrons can be used to compute electron temperature and density. There is a condition when the triangular wave reachs its higher voltage, the probe will attract more electron until the satellite bodies is also fulfilled with electrons, as the result the probe cannot attract electrons properly and the satellite cannot measure the current of electrons. To tackle this problem, an electron gun which has tungsten filament heated to about 2000 ^{o}K, thus the electrons in the satellite bodies have enough kinetic energy to escape from the surface of the wire [MSSA^{+}16]. These sensors are employed to measure electron temperature and density as a comparison data to verify the

GNSS-RO sensor data. Description of GAIA–I microsatellite and its sensors are depicted in Fig. 2.2.

The GAIA-I is completed with the bus system and mission instruments. The bus system is supported by a battery, a control unit for power management, distribution unit of power (PDU), solar battery paddle, S–band antenna and receiver-transmitter (STRX). It is also connected to X band antenna and transmitter (XTX), data processing unit, attitude control unit, reaction wheel (RWA), magnetic torque (MTQ), inertial reference unit (IRU) or Gyro, GPS receiver (GPSR), star sensor (STT), coarse solar sensor (CSS), magnetometric sensor (MAGS), heater controller, body structure, electrical circuit, mechanical equipment and other supporting materials. Mission instrument which is the main arms consisted of GNSS–RO sounding sensor (L–band and Ka–band receivers), EDTP sensor, and mission data processing unit [SSI15]. The structure of the GAIA–I system is illustrated in Fig. 2.3, while its specification is summarized in Table 2.2.

2.3 CP Antenna for GNSS–RO

The GNSS–RO satellite is a receiver to the GNSS signals. Therefore, there are several requirements should be satisfied in order to receive the best RO signals. Some important parameters are polarization, gain, and radiation pattern. The material of the antenna is an important consideration as well since it will be launched into the space. Thus, several space environment requirements should be satisfied.

The gain of the antenna has to be sufficient to reach the demanded sensitivity and obtain good signal to noise ratio (SNR) for a better quality of

Table 2.1: The GAIA-I Microsatellite Specifications [SSI15]

Component	Items	Details
Satellite Size	Height	450 mm
	Length	460 mm
	Width	500 mm
Payload	Weight	$<$ 50 kg
GNSS–RO	Band Frequency	L (GNSS) and Ka (O3b)
	Accuracy	$<$ 15 minutes
	Sensitivity on cold start	-130.9 dBm
	Input voltage	28 Vdc
	Power	mean 25 W, max 30 W
	Receiver Weight	4 kg
	Receiver Size	200 x 170 x 120 mm
	RO Antenna Weight	0.75 kg
	RO Antenna Size	350 x 450 x 30 mm
	POD Antenna Weight	0.4 kg
	POD Antenna Weight	130 x 130 x 6 mm
EDTP Sensor	Type	Langmuir Probe
Command Comm	Receiver Frequency	2025-2125 MHz, LHCP
	Transmitter Frequency	2200-2300MHz, LHCP
	Modulation	FSK 9600 bps
Mission Comm	Transmitter Frequency	8025 - 8400 MHz, LHCP
	Modulation	QPSK 20 Mbps

Table 2.2: GNSS–RO Antenna Requirement

Parameters	Requirement
Frequency	Dual-band (1150–1300 MHz and 1559–1611 MHz) Wideband (1150–1611 MHz)
Gain	9 dBic (much higher is better) [RSW$^+$13]
Axial Ratio	$<$ 3-dB RHCP
Field of View	through earth's limb -25 $\pm$5 degree elevation $\pm$55 degree azimuth of scan angle [TYM12]

processed signals. The required gain of GNSS–RO receiver is 9 dBic, but the higher is better [RSW+13]. However much higher gain is necessary for the RO sounding system to get the best possible measurement results. For example, FORMOSAT-7/COSMIC2-2 RO antenna has gain around 17.3 dBic, approximately 10 dBic more than the previous version in the form of FORMOSAT-3/COSMIC. GNSS signals perform the RHCP sense, which is orthogonal to the orientation of the cross-polarized LHCP signals. Therefore, the receiver antenna should have a specification of high RHCP gain in the main beam and suppressed cross-polarized LHCP gain. This cross-polarization suppression can eliminate unwanted multipath waves due to reflection on GNSS signals [TYM12].

The radiation pattern of antenna determines the quality of the signal reception, as an accurate beam pointing results in the best measurement. As the RO signals are refracted by the atmosphere, the origin of signals is not at the zenith of satellite view, but it follows the earth's limb. Therefore, usually, the beam of RO antenna is steered -255–degree in elevation and has 55–degree scan angle in azimuth to get the RO signal field of view [TYM12]. The beam direction can be adjusted mechanically or electronically.

To receive all GNSS signals, the RO antenna should cover 12.2% bandwidth at L2 and L5 (1150-1300 MHz) of GNSS band and receive L1 band at 1559–1611 MHz or 3.2% bandwidth. Therefore, the design of GNSS receiver antenna has two approaches, single wideband or dual band. The first option is probably the simplest design since there are a lot of presented wideband antenna in the literature, for example conical, bow-tie dipole, slot, and a spiral antenna. The advantages of wideband performance are low dispersion and insensitive to frequency diversion. However, the wide bandwidth reception of 1150 to 1611

MHz make it depend merely on the correlator located in the satellite receiver system to divide different channels and resist interference [IGB10].

An antenna developed for satellite is subjected to high degree variation of temperature. The thermal condition depends upon the satellite orbit, the thermo–optical properties, incidence of solar radiation, radiative and conductive couplings with the peripheral parts of the satellite, and the heat released by equipment or components inside. Therefore, the antenna design should consider temperature variation typically in the range between –190 and 160 °C. To anticipate this condition, it requires a surface coating that has suitable coefficients of thermal expansion (CTEs) to avoid cracking and debonding. Passive thermal control devices composed of multilayer insulation (MLI), sunshields, coatings, and paints are also applied to confine temperature range, the heat coupling with the peripheral parts, and the thermoelastic distortions. For this purpose, aluminized Kapton, black Kapton, white paint or Betacloth are utilized [IGB10].

2.4 CP Printed Slot Antenna

Performance of an antenna, including slot antenna, is determined by its reflection coefficient (S_{11}), gain, polarization, bandwidth, and radiation pattern. The reflection coefficient of an antenna describes represents how much power is reflected from the antenna due to unmatched impedance. If it is 0 dB, , then all the power is reflected from the antenna and nothing is radiated. This can damage the RF source system. The ideal value of S_{11} is below -10 dB which means at least 90% input power is delivered to antenna and reflected power is less than 10% (radiation efficiency is 90%).

The gain of antenna determines the portion of power from the source radiated to the main direction. The measure of gain usually compared to an isotropic antenna which has 0 dB gain thanks to its equal distribution of power radiation to all direction. If an increasing amount of power emitted to certain direction then the gain will increase. According to the portion of radiated power, the region is divided into main beam and side lobe. The main beam is a region that has maximum radiation, usually the beamwidth is within 3 dB of its top beam and determines the gain of an antenna. The side lobe is regions outside the main beam and usually has a low portion of transmitted power, as outlined in Fig. 2.4. Meanwhile, bandwidth is the frequency coverage of the antenna from the lowest to the highest frequency where the antenna can transmit and receive electromagnetic wave. The center frequency usually located in the middle of the bandwidth.

The radiation pattern describes the distribution of power radiation as a function of direction and illustrated in three–dimensional coordinates. Due to a characteristic of the antenna, there are many patterns of radiation, such as isotropic (similar pattern in all direction), omnidirectional (the patterns similar in all azimuthal angle but differs in elevation angle), and directional (has the asymmetric pattern and most power in the main beam).

The orientation of electric field emitted by an antenna determines its polarization. To generate CP radiation, it is necessary to produce electric fields with two orthogonal components in the far field area, as explained by Equation 2.4 [GLZ14].

$$\overrightarrow{E}(\theta,\varphi) = \overrightarrow{\theta}\, E_\theta(\theta,\varphi)e^{j\phi_1} + \overrightarrow{\varphi}\, E_\varphi(\theta,\varphi)e^{j\phi_2} \tag{2.4}$$

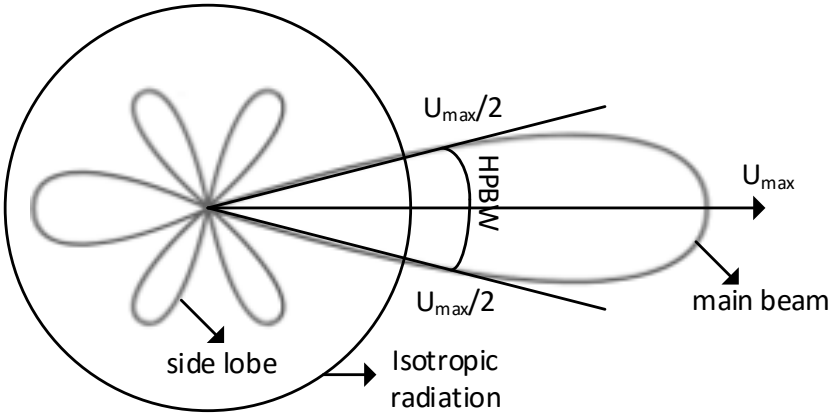

Figure 2.4: Illustration of isotropic radiation and gain of antenna

where $E_\theta(\theta, \varphi)$ and $E_\varphi(\theta, \varphi)$ indicate the amplitude of two electric field components in the far field. ϕ_1 and ϕ_2 indicate the phase shift of both components respectively.

CP operation is achieved if both orthogonal components have identical magnitude and a 90° phase divergence. In this case, the vector of the electric field at a specified point observed in time distribution constitute a circle. The orientation of rotation can be described by monitoring direction of the rotation of the field along the course of propagation. A clockwise rotation indicates that the sense is RHCP; otherwise, it is LHCP. In fact, perfect circular polarization is impossible to obtain, thus the curve of both electric field in time distribution is normally ellipse. The proportion of major axis over the minor axis of the curve is called an axial ratio (AR), as depicted in Fig. 2.5. To differentiate the type of polarization can be determined by measuring AR value. A circular polarization usually has AR under 3 dB [GLZ14].

The geometry of a microstrip slot antenna is modest, lightweight, and easy to

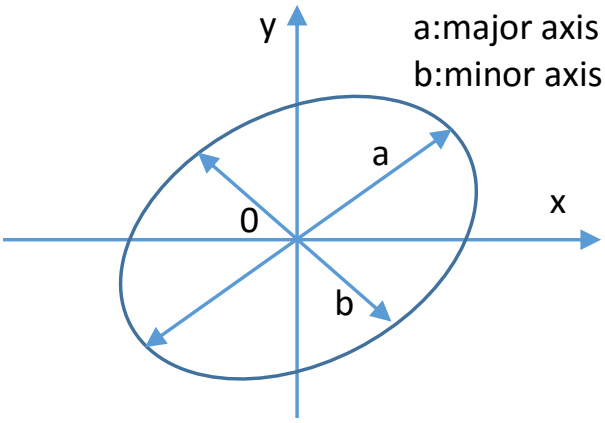

Figure 2.5: The major and minor axis of both electrical fields which draw the polarization curve[GLZ14].

fabricate. It composed of a microstrip feed on the bottom part that couples electromagnetic waves to the slot which is the radiating part. The other advantage of microstrip slot antennas is larger bandwidth more than common patch antennas. for example, a CP microstrip antenna with square slot design. The ground plane located on top layer is cut to create a square slot, while on the bottom side, microstrip lines feed network which employs a Wilkinson power divider is printed. The power divider has two different lengths of arms with a deviation of a 0.25λ, to create a 90^{o} phase discrepancy between two orthogonal modes. As an outcome, a polarization with circular orientation is produced by the antenna [GLZ14].

The rule of thumb in designing a slot antenna is the length should be a 0.5λ, whereas the shape can be a circular, crossed, triangular, square–ring, annular–ring, or triangular–ring. A CP circular wide slot excited by two orthogonal feed lines which employ a Wilkinson power divider as well to create circular polarization is reported in [GLZ14].

There is also another feed line type for CP printed slot antenna. Instead of using dual orthogonal feeds network which takes large of space on the bottom

side, a single feed can be employed to simplify the feed network. For example, a square ring slot antenna excited by a quarter-wavelength L-shaped feed line which generates two orthogonal modes [GLZ14]. Thus, a 90° phase discrepancy of both orthogonal modes also occurs which leads to CP operation. The disadvantage of this antenna comes from the radiation pattern which is bi-directional, the unwanted backward radiation occurs due to no ground plane under the feed line. To tackle this problem, a ground plane as a reflector with a height of a quarter-wavelength placed under the antenna so as to produce only the forward radiation will be generated and also improve the gain simultaneously.

2.5 Related Works

Many CP antennas have been proposed for GNSS receiver and S–band communication system antennas have been presented in the literature. Some of them are a single wideband, while the others are a dual band. Various CP antennas designed for the GNSS receivers are six–turns equiangular spiral incorporated with ground [IGB10], helix antenna with the bifilar design [SR14], and slot antenna having annular–ring shape perturbed by hat–shaped disturbance [SC11]. Some dual–band antennas are also reported to be presented for the GNSS receiver such as stacked–patch fed by a branch line hybrid incorporated with proximity probes [IGB10] and dual connected probes in parallel attached on a microstrip antenna [SZL15]. Meanwhile, the GAIA–I communication system also adopts CP antenna for their command system. Several CP antennas have been presented for a communication system in S-band such as helix with the quadrifilar design [GGTC12], [GLZ14], spiral with conical shape

[8][Hus12], and antenna with isoflux pattern[CLLL14], [CLL13].

A printed slot antenna has many advantages than the above–mentioned types for a space-based application which demands low profile, light, and CP bandwidth more than 33%. According to its feeding method, printed slot antenna has two main categories, coplanar waveguide (CPW) feed with its wider bandwidth and microstrip–line feed with its better gain. The first type is classified into wide and ring slot. Generally, a ring slot offers smaller bandwidth compared with a wide slot, but provide a more compact size. However, by enlarging the slot size, the 3–dB ARBW can be improved as much the wide slot. It is reported that a slot antenna with annular–ring shape possessing a slot size of $0.068\lambda_0$ and a hat–shaped perturbation fabricated on an RT5880 laminate successfully reaches CP bandwidth of 65% at 1638 MHz center frequency[SC11]. A slot antenna with square-ring design presenting a slot size of $0.02\lambda_0$ printed on an FR4 laminate manages to gain CP bandwidth of 6.3% at a center frequency of 1630 MHz [RW08]. On the other hand, more extensive 3–dB ARBW (68%) is performed by a CPW–fed wide slot antenna with symmetric–aperture [NCQ11]. It is also presented that a CPW–fed antenna with square slot design and three inverted–L–shape fragments secure CP bandwidth of 86.4% [FNGP11].

Meanwhile, there is few printed slot antenna design with wideband CP performance propose a wide slot or equilateral triangular-ring. One of them is an ETS antenna excited by an L–shaped fragment feeding performs CP bandwidth of 3.2% [HCR08]. 3-dB ARBW enhancement is obtained by bringing up its inner triangular patch which then becomes a parasitic patch for a wide slot performing the CP bandwidth of 31%. However, a bulky dimension and fragile construction are the drawbacks. It had been reported also a coplanar

waveguide fed ETRS antenna makes use of a stub for impedance matching cannot achieve a CP radiation [CCR05].

Basically, a ring slot without modification presents a linear polarization (LP) operation. Transformation of its polarization to circular can be conducted by introducing several modifications, for example, an insertion of a disturbance patch into the slot incorporated with a lopsided feed line [SC11], [WHC02]. A conjunction of two ring slots [CL11] and the make use of stripline hybrid coupler as a feed line [QC99] produce the similar alteration. In a similar way, the application of a slit delivers small 3–dB ARBW. As being reported, a slit introduced into an annular–ring slot fed by a curved feed line produces CP operation [SHHO07] with less than 10% 3–dB ARBW. Introduction of two slits to an annular–ring patch has produced less than 1% 3–dB ARBW [CW99]. Additionally, there is no report on the implementation of the slit in improving 3-dB ARBW of a slot antenna. Meanwhile, an asymmetrical dipole fed by microstrip feed line completed with a slit projected on the center of feed line [BAM10] has presented CP bandwidth of 23%.

Printed slot antennas exhibit bi-directional radiation with the cross–polarization radiation at the backside being unwanted and can be harmful. Many efforts have been done to suppress the backside radiation so as to get unidirectional radiation, such as installing a reflector made from sheet metal below the antenna to reflects the cross-polarization. The height of the reflector (H) is equal to a 0.25λ to obtain an in-phase wave reflected back by the reflector to create the uni-directional pattern. The form of the reflector influences the CP performance, particularly its directivity and bandwidth.

Chapter 3

Design of Wideband CP Antenna for GNSS–RO and S-Band Communication System

In this research, the GNSS receiver and S-band command communication system antenna for the GAIA–I are developed by utilizing printed circuit board (PCB) material which has a laminate material with relative permittivity ε_r, thickness h, loss tangent are 2.17, 1.6 mm, and 0.0005 respectively. The cupper on the top and bottom side of the laminate has a thickness of 0.035 mm. The advantage of this laminate is the low dissipation factor. Both antennas are developed based on ETRS design thanks to its simplicity. There are two novel techniques proposed here to alter the polarization of conventional ETRS microstrip antenna from linear to circular and also widen the CP bandwidth. The first technique introduces truncation on each ETRS corners, grounded perturbation patch, and a pair of slits then called type 1 ETS antenna due to the diminished influence of inner patch. The second one employs truncation

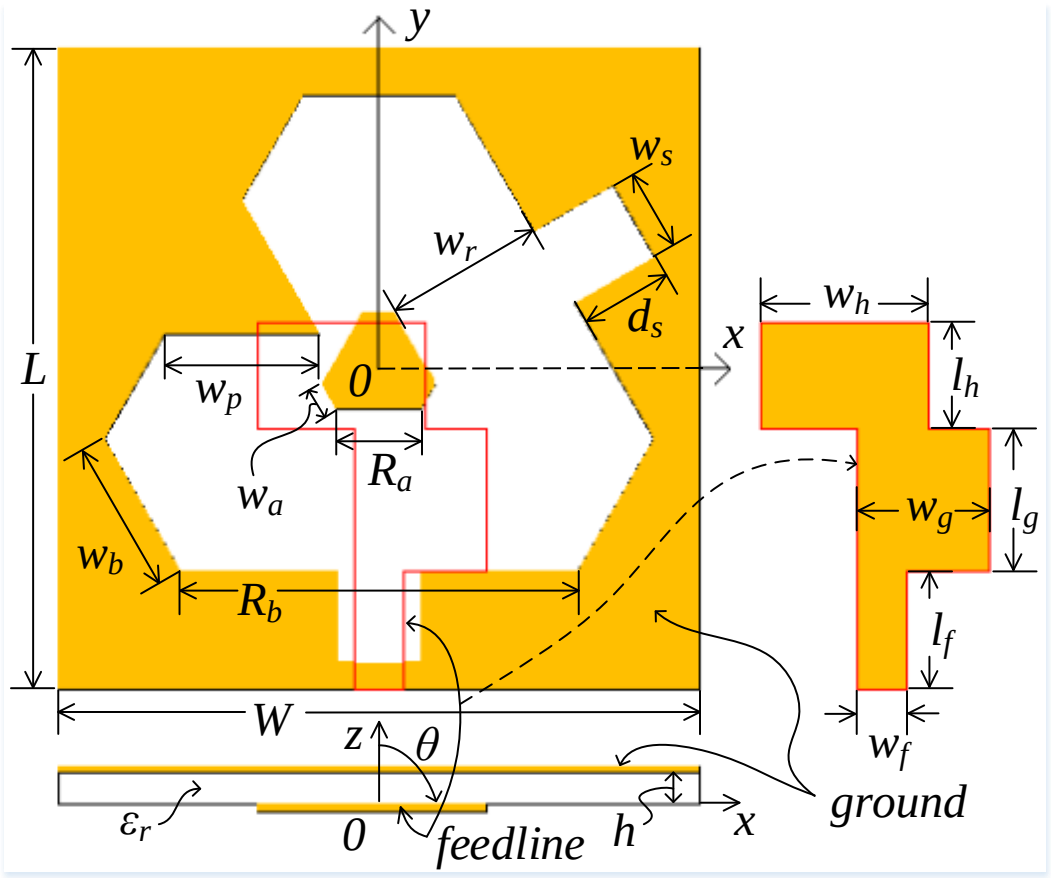

Figure 3.1: Structure of the proposed type 1 ETS. On the right side is a feed line and on the bottom part is the side view [ASSI+18].

on two ETRS corners, grounded perturbation patch and coupled diagonal line slot then called type 2 ETS antenna. Both antenna types are designed and simulated using CST Studio.

3.1 ETS With A Pair of Slits For The Command Communication System (Type 1)

The geometry of the proposed type 1 ETS is depicted in Fig. 3.1. The width and length of the feed line are projected clearly next to the main design, while

the side profile visualizing every layer is outlined below. The feed line is inserted on the bottom layer, while the ETS with its properties are constructed on the top layer. The ETRS and its inner triangular patch are truncated as much w_b and w_a respectively to create an inner patch side size R_a and a slot side size R_b, hence ETS with slot width w_r. A grounded equilateral triangular perturbation patch with side size w_p is attached to create perturbation on ETS. Those modifications on ETRS can produce a perturbation on the distribution of magnetic currents, thus create phase orthogonal resonant mode to both equal magnitude electric fields to generate CP radiation. To improve the quality of AR below 3 dB, w_p is set equal to w_b. While to improve the AR bandwidth, two equal sizes of slits with the length of d_s and width of w_s is inserted in the middle of bottom part and center of the right side. The feed line is modified as well by placing bottom branch extending to the right as much l_g with a width of w_g. The top branch with width and height of w_h and l_h respectively extends to the left side. This antenna type is developed for both command communication system and GNSS sensor receiver antennas.

CP antenna designed for the command communication system works at 2025–2125 MHz for signal receiving purpose and acts as transmitter at 2200–2300 MHz. The rule to design this type 1 antenna is started by determining a resonant frequency which related to slot width of conventional LP ETRS. Secondly, generation of CP operation is conducted by chamfering the corner of each slot and inserting a grounded perturbation. Finally, two slits is created to improve further. The achievement of this antenna is highly dependent on the difference of some parameters. Thus, a study on variation of some parameters is explained to provide a guidance in designing the slot antenna.

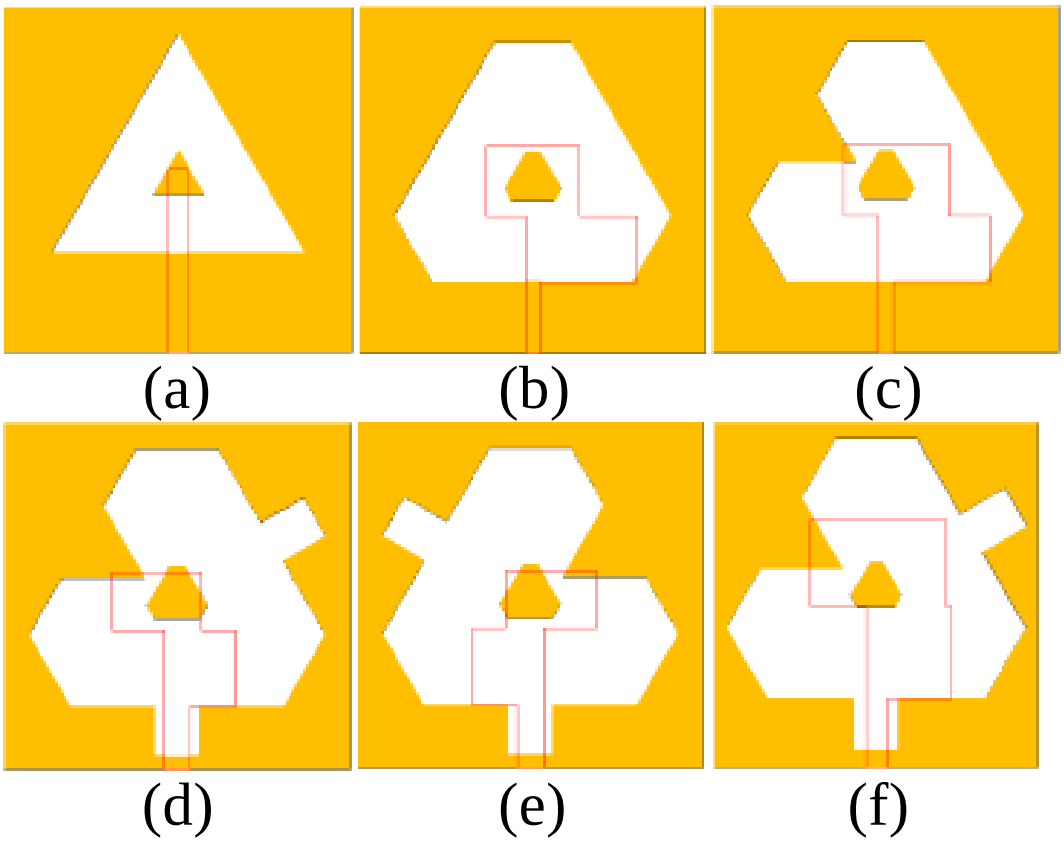

Figure 3.2: Simulated type 1 antenna (a) Conventional LP, (b) Model 1a, (c) Model 2a, (d) Model 3a, (e) LHCP Model 3a, and (f) model 4a (GNSS). The feed lines on back side are red coloured[ASSI+18]. The dimensions are tabulated in Table 3.2.

3.1.1 Conventional ETRS of Type 1 Antenna

The basic structure of the conventional ETRS type 1 antenna has smaller slot width compared to the type 2 as outlined in Fig. 3.2.a. Its center frequency depends on the slot mean perimeter which influenced by the size of the slot [WHC02]. Two types of modifications can be selected as an option to decrease the center frequency of this conventional model. Firstly, an extension of the slot size w_r and maintaining inner side length $R_1 = R_a + 2w_a$. Secondly, an expansion of the inner patch size while maintaining the slot size. The first option offers a broader bandwidth compared to the other option, but a bigger

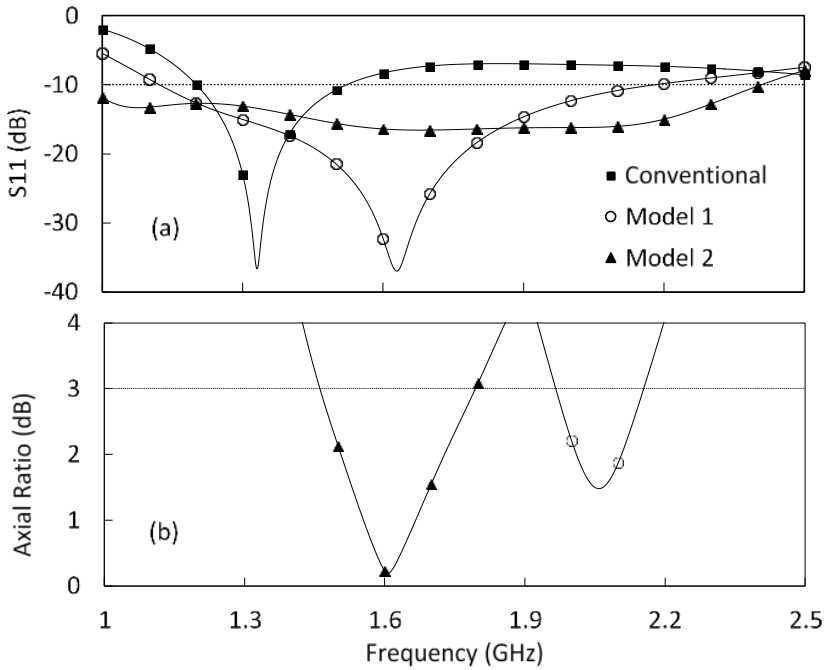

Figure 3.3: Simulated results of (a) S11, (b) axial ratios for LP ETRS, model 1a, and model 2a of type 1 ETS antennas.

antenna dimension is the shortcoming. The center frequency is also influenced by the ground plane size surrounding the slot L x W and material of the laminate [SC11]. Initial setting on inner patch side length R_1, antenna size L, and type of the laminate are decided in advance. The conventional ETRS is fed by a feed line with center on y–axis, length of $l_t = l_f + l_g + l_h = 67$ mm and width of $w_f = w_g = w_h = 3$ mm. The value of R_1 is set to 18.3 mm, L is $1.4R_2$, and the outer side length $R_2 = R_b + 2w_b$. The mean perimeter of $3R_m$ in frequency span between 1 to 3 GHz as indicated by several simulation results using mentioned dimension is about $0.86\lambda_g$ to $1.05\lambda_g$ (guided wavelength). As the center frequency is set at around 1.36 GHz, the mean perimeter of $3R_m = 3(R_1 + R_2)/2$ is simulated to be approximately $0.88\lambda_g$. Since $\lambda_g = 0.19$ m, it can be obtained that $R_m = 55.2$ mm, $R_2 = 2R_m - R_1 = 92.2$ mm, and $w_r = tan30^o$ x $(R_2 - R_1)/2 = 21.3$ mm. The simulated results indicate

the best dimension of this conventional ETRS is $L = W = 126$ mm. The yielded dimension is tabulated in Table 3.1. Fig. 3.3 shows obtained impedance bandwidth around 320.6 MHz as tabulated in Table 3.2.

3.1.2 Slot Truncation and Deformed Feed Line (Model 1a)

Change on type 1 conventional model geometry can alter the polarization become circular. Chamfered corners and branched feed line emerge as a solution, called as model 1a and outlined in Fig. 3.2.b. The corner truncations are conducted by trimming each corner as much w_b of 20 mm. As a result, the slot size becomes narrower, so does the antenna length (L) which become 90 mm. The branched feed line is constructed by pasting a pair of branches. The dimension such as w_f, w_g, w_h, l_f, l_g, and l_h should be tuned properly to obtain broader impedance bandwidth. The lowest line of the bottom branch should be in a row with the lowest line of the slot. The size of w_g provides a notable impact in adjusting the center frequency, widen the reflection coefficient bandwidth and improve the AR as described in Fig. 3.4. The smaller w_g lowers the resonant frequency and broadens reflection coefficient bandwidth, while also lessens 3–dB ARBW. A different outcome is obtained by a larger w_g. Meanwhile, the dimension of w_h, l_g, and l_h can be utilized to enhance the impedance matching and bring down (better) AR. The best outcome is achieved if the bottom branch extends to the right, while the top one is expanded to left and right equally. The dimension of the model 1a antenna as tabulated in Table 3.1 produces CP bandwidth of 188.2 MHz as depicted in Fig. 3.3 and Table 3.2. Since the impact of the inner patch to the achievement of the model 1a degraded, the ring slot changes become an ETS antenna.

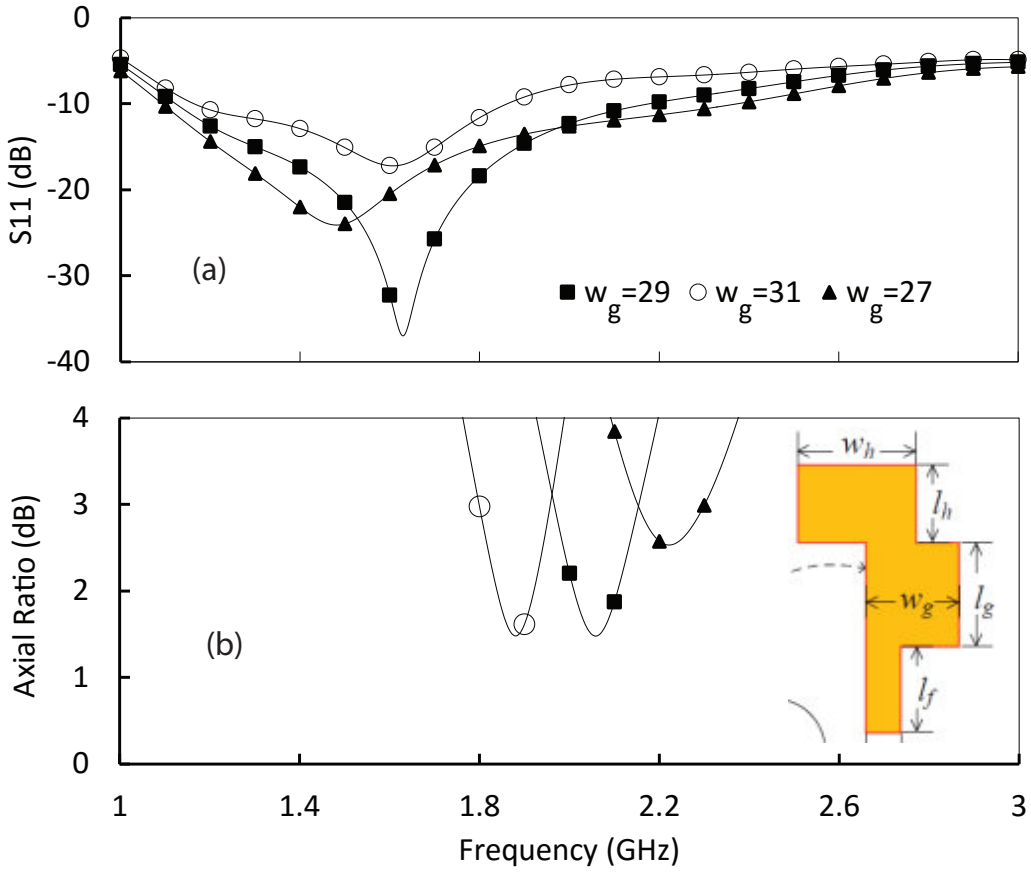

Figure 3.4: Variation of (a) S11, (b) AR for different w_g sizes of Model 1a.

3.1.3 Equilateral Triangular Disturbance (Model 2b)

The result of model 1a shows little CP bandwidth situated on the highest part of the impedance bandwidth area. Thus, an improvement and center frequency shifting are demanded. A grounded perturbation patch introduction has been evident to create two degenerate orthogonal modes as a requirement for CP radiation [SC11, WHC02]. However, the shape of disturbance patch influences 3–dB ARBW of the ETS antenna. An equilateral triangular disturbance patch created on the left side of the slot yields good 3–dB ARBW better than rectangular patch which commonly used in other ring slots. Size w_p of the equilateral triangular disturbance patch determines the 3–dB ARBW as

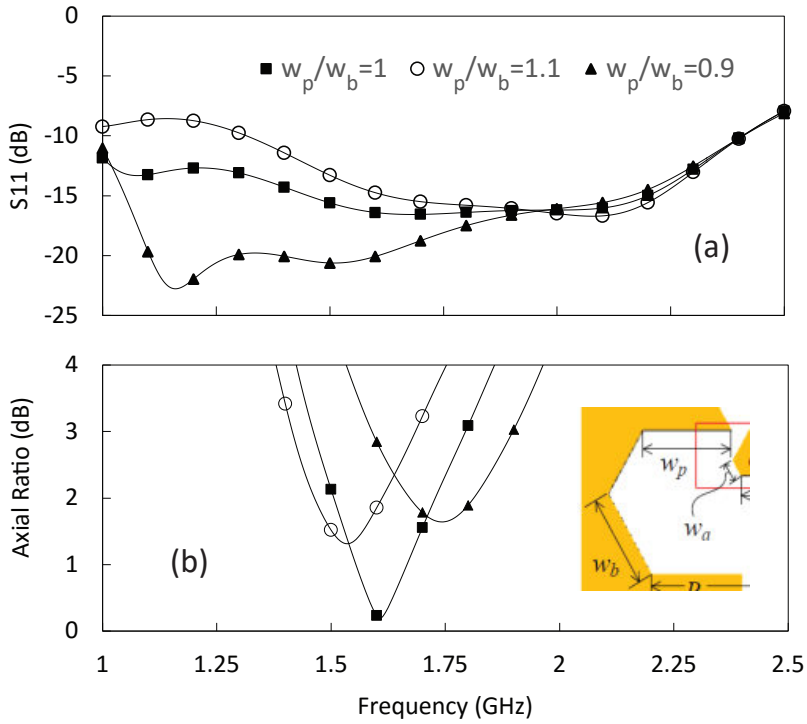

Figure 3.5: Variation of (a) S11, (b) AR for different ratio of w_p to w_b of Model 2a.

described in Fig. 3.5. A larger w_p relative to w_b moves the center frequency of AR to the smaller one. Conversely, a higher center frequency is produced. The better 3–dB ARBW is yielded if $w_p = w_b$ which lower AR its center frequency is closer to the impedance bandwidth. The best result is obtained when the branch width w_h of the feed line is expanded to 27.5 mm with its right part is extended 5.5 mm more than the left part. The model 1a incorporated with the triangular disturbance patch is called as model 2a as depicted in Fig. 3.2.c and its dimension is summarized in Table 3.1. This model offers broader impedance and ARBW compared with the model 1a by delivering 1442.5 MHz and 331 MHz respectively as described in Fig. 3.3.

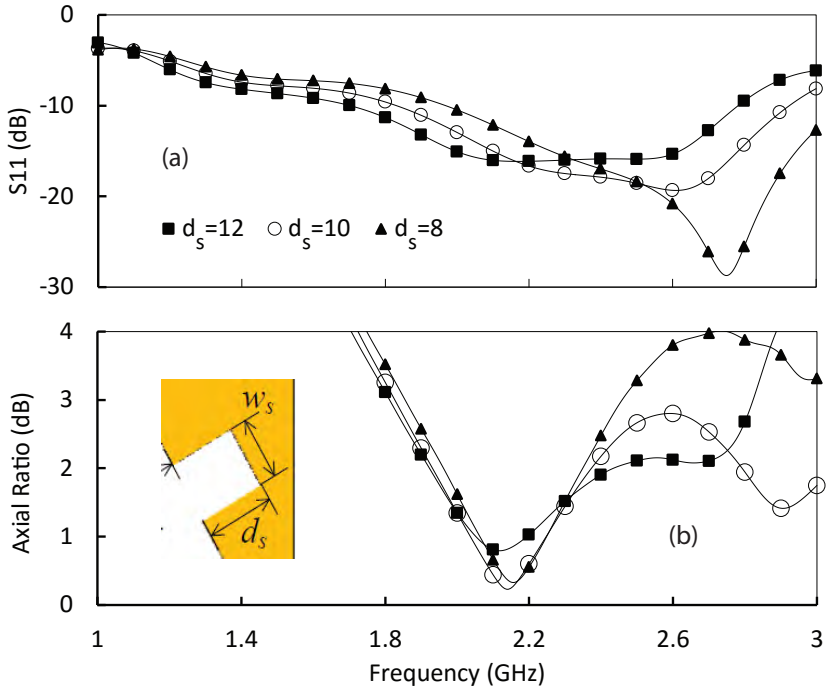

Figure 3.6: S11 and axial ratio variation of different d_s sizes with $w_s = 11$ of Model 3a.

3.1.4 Introduction of Two Equal Size Slits (Model 3a)

Reflection coefficient bandwidth of the model 2a is quite larger compared with its 3–dB ARBW, thus model 3a is proposed for further enhancement. In this new model as outlined in Fig. 3.2.d, the introduction of a pair of slits is inserted to the center of lowest side and center of the right side of the ETS to achieve a notable 3–dB ARBW enhancement. Only one slit insertion yields little improvement. The impedance and AR bandwidths can be tuned by changing the length of d_s and width of w_s as outlined in Fig. 3.6 and Fig. 3.7. Extention of slit length d_s can lower the center frequency, but must not exceed the antenna size L. Length of d_s as much 12 mm yields center frequency of 2242.45 MHz. Meanwhile, d_s of 10 mm yields broader 3–dB ARBW, yet parts of it are outside of the reflection coefficient bandwidth and near to the 3 dB limit. Shorting d_s size below 10 mm narrows 3–dB ARBW drastically.

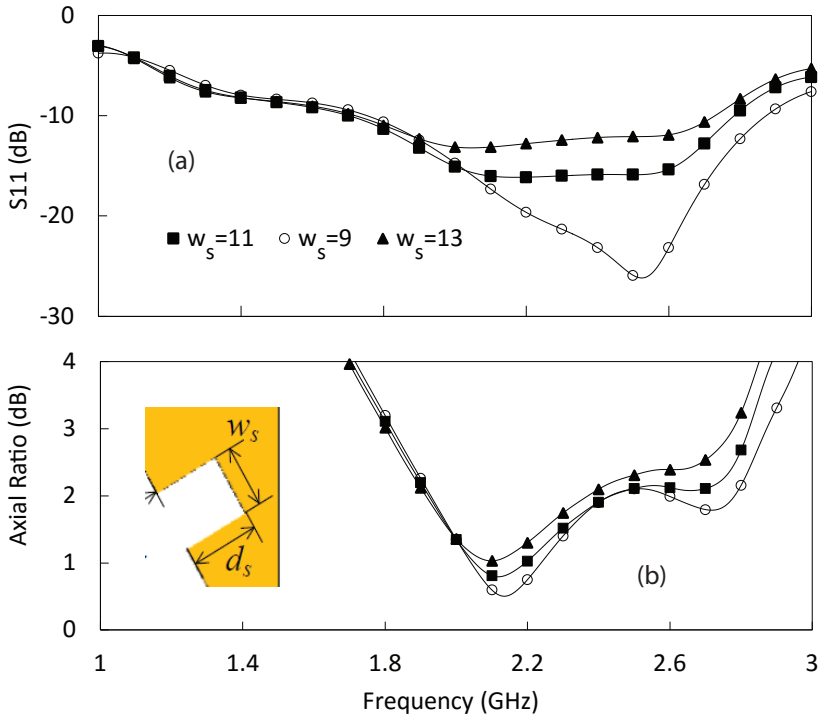

Figure 3.7: S11 and axial ratio variation of different w_s sizes with $d_s = 12$ of Model 3a.

Broadest 3–dB ARBW improvement is achieved if w_s is 9 mm as shown in Fig. 3.7, but under 50 Ω input impedance is the drawback. The w_s size of 11 mm balances the input impedance to 50 Ω, even though the 3–dB ARBW is slightly smaller than that of 9 mm. The wider w_s significantly drops the CP bandwidth. As the slits introduction modifies ETS structure, hence feed line deformation is required. The feedline parameters such as w_f, w_g, w_h, l_g and l_h are adjusted as tabulated in Table 3.1 for improvement. Lowering the antenna size to 84 mm widens the 3–dB ARBW. Above configuration produce wider 3–dB ARBW about 1010.8 MHz near to its reflection coefficient bandwidth about 1080.7 MHz. Since not all the 3–dB ARBW is located inside of the reflection coefficient bandwidth, the antenna only presents CP operation with a bandwidth of 971,2 MHz as tabulated in Table 3.2. The dimension of this model 3a is summarized in Table 3.1. It can be concluded that the pair of slit

Table 3.1: Configuration of The Designed Models Parameters.

Antenna Models	L mm	W mm	w_r mm	w_f mm	w_g mm	w_h mm	l_g mm	l_h mm	d_s mm	w_s mm
Conv Model Type 2	126	126	21.4	3	3	3	11.3	22.3	–	–
Model 1a	90	90	21.4	4	29	24	17.3	18.3	-	-
Model 2a	90	90	21.4	4	29	27.5	17.3	18.3	–	–
Model 3a	84	84	21.4	6.5	17.3	22	18.6	14	12	11
Model 4a	100	94	26.7	6	19	39	26.9	25	15	13

Table 3.2: Achievement Of The Designed Antenna Models, fcibw is Impedance Bandwidth Center Frequency, farbw is ARBW Center Frequency.

Antenna Models	fcibw MHz	Imp BW MHz, %	fcarbw MHz	3–dB ARBW MHz, %
Conv Model Type 2	1361.7	1201.4–1522 (320.6, 23.5%)	–	– –
Model 1a	1651.2	1122.2–2180.1 (1057.9, 64%)	2060.2	1966.1–2154.3 (188.2, 9.1%)
Model 2a	1686.3	965–2407.5 (1442.5, 85.5%)	1629.5	1463.9–1795.1 (331, 20.3%)
Model 3a	2242.5	1702.1–2782.8 (1080.7, 48.2%)	2317	1811.6–2822.4 (1010.8, 43.6%)
Model 4a	1400	1000–1800 (850, 60.7%)	1675	1100–2250 (1200, 71.6%)

has significant impact to double the 3-dB ARBW and decrease the antenna size.

3.1.5 Further Design Analysis

To produce CP radiation on a printed antenna, the total electric fields must have two orthogonal parts (x and y directions) with similar amplitude and 90° phase discrepancy. This will generate simultaneous generation of two orthogo-

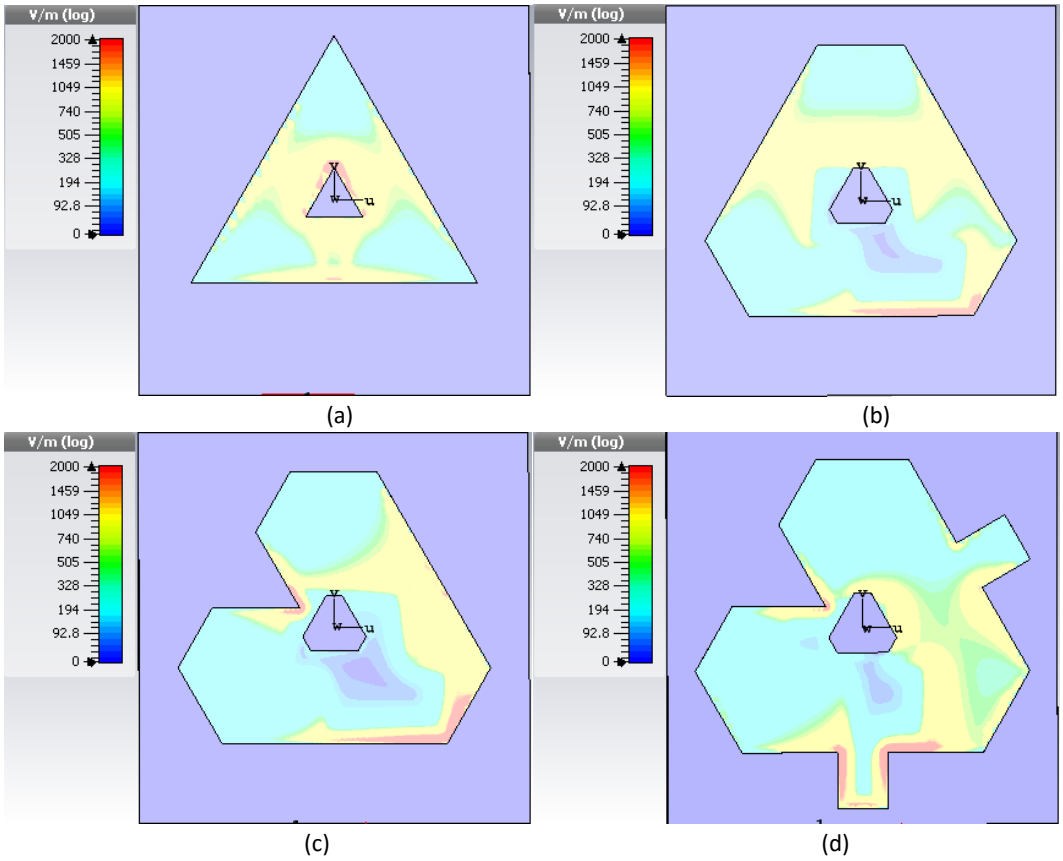

Figure 3.8: Magnetic currents distribution represented by tangential electric field of (a) conventional LP, (b) model 1a, (c) model 2a, (d) model 3a of type 1 ETS antenna.

nal degenerate resonant modes, in the form TM_{10} (x–direction) and the TM_{01} (y–direction) [GLZ14]. To produce circular polarization, a perturbation on the magnetic current distributions is required to produce two similar-magnitude resonant modes with 90° phase discrepancy [SC11]. For this purpose, a modification on the conventional structure is required. The basic model produces magnetic currents spread mostly in the center and disperse to every side of the ETS, as illustrated in Fig. 3.8.a. The truncated corner (model 1a) disturbs the distribution of magnetic currents in the center, as shown in Fig. 3.8.b. Meanwhile, Fig. 3.8.c indicates that the disturbance patch (model 2a) perturbs the magnetic currents on the left side of the ETS, thus its spreads mainly on the

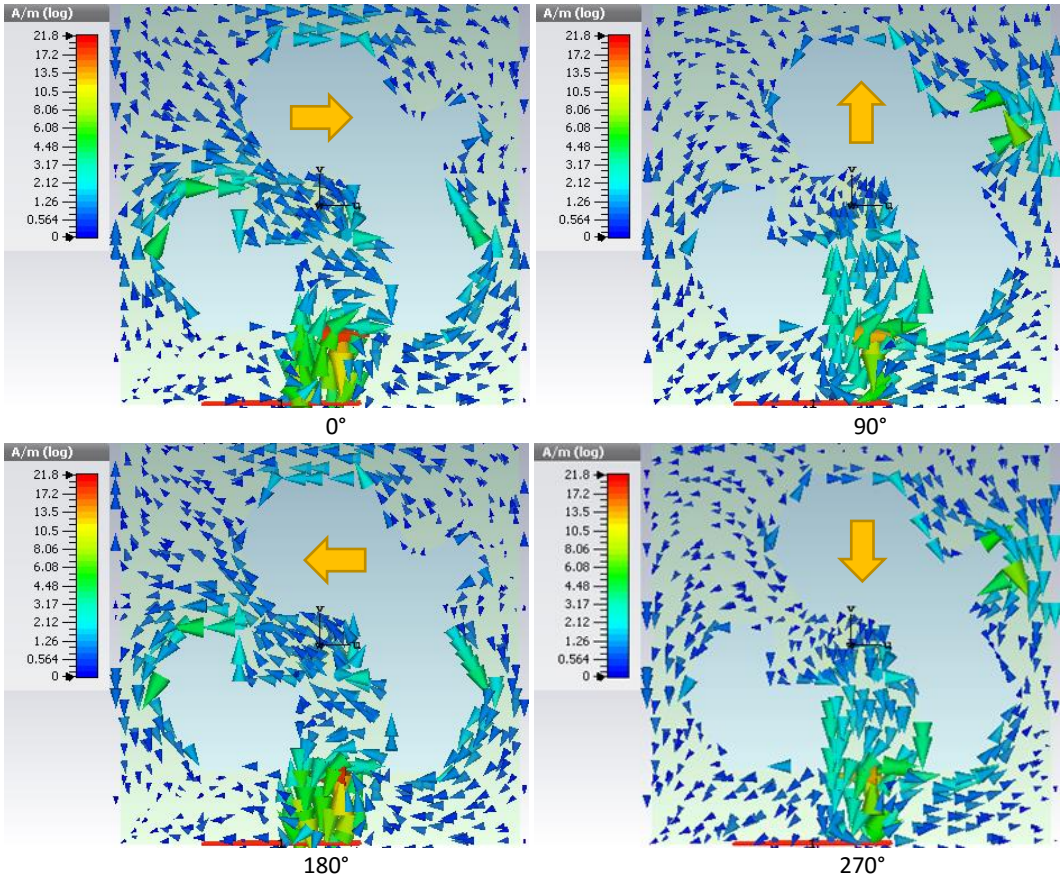

Figure 3.9: Surface currents distribution of model 3a at its center frequency. Orange arrows illustrate directions of dominant currents.

right and bottom side. Next, Fig. 3.8.d highlights the introduction of both slits (model 3a) alters the distribution in each slit region. This perturbations create two orthogonal parts that have similar amplitude and 90° phase discrepancy in a broad frequency span as described by the 3–dB ARBW.

Performance of the model 3a is described also by simulated surface currents distribution in Fig. 3.9. The ° phase reference shows that the majority of surface currents is directed to +x–axis. As for 90° phase, most of the currents flow toward the +y–axis. Further, at 180° phase, the observed majority currents is directed toward –x–axis, which is difference arrangement to the 0° phase order. At last, the 270° phase reference, the dominant currents is phase inverted than

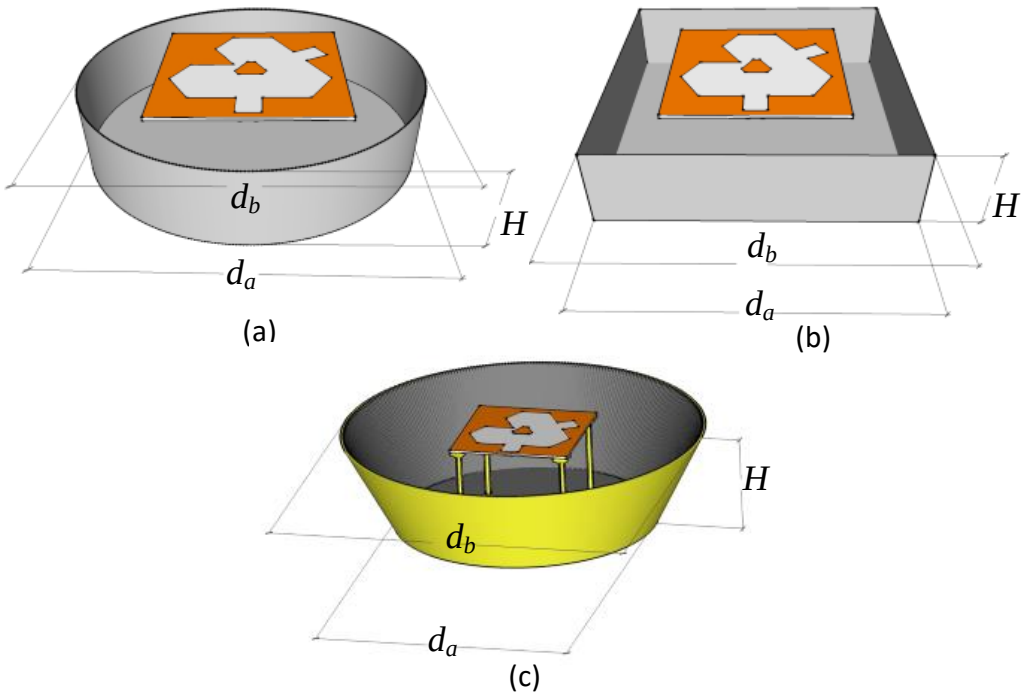

Figure 3.10: Simulated reflector for model 3a (a) cylindrical cup, (b) square cup, (c) truncated cone

the 90° as its directed to –y–axis. Therefore, the sense of the polarization is right-handed.

LHCP operation can be created from the model 3a by mirroring the position of the disturbance patch and right slit. Additionally, branches location of the feed line is shifted to their opposite side. The outline of model 3a with LHCP radiation is depicted in Fig. 3.2.e. This LHCP design presents equal CP achievement as the RHCP model.

3.2 ETS Antenna Type 1 for The GNSS–RO Receiver (Model 4b)

The GNSS–RO sensor works at range frequency from 1150 to 1611 MHz. Therefore, the center frequency of RHCP antenna is 1380 MHz with fractional bandwidth of 33.4%. The proposed model 3a delivers broader fractional bandwidth exceeding this requirement. Thus, the GNSS–RO receiver antenna can be developed by using the same design as illustrated in Fig. 3.2.f. As its operating frequency is below the model 3a coverage, the antenna size is changed. Slot size w_r, truncation size w_b, and perturbation side length w_p are enlarged to lower the operating frequency. Slits length d_s and its width w_s are expanded as well to provide similar bandwidth enhancement. These changes make the antenna length L longer compared to the width W constitute new rectangular antenna and called as the model 4a and its dimension is detailed in Table 3.1, while its simulated performance is tabulated in Table 3.2.

3.3 Unidirectional Radiation of Model 3a

Printed slot antenna delivers bi–directional radiation with the backside radiation of cross–polarization being unwanted and can be harmful. To change the radiation to uni-directional, a metal reflector is installed under the antenna to reflect the cross-polarized radiation. The height of the reflector (H) is 0.25λ to obtain an in-phase wave reflected back by the reflector to create the uni-directional pattern. The form of the reflector influences the CP performance, particularly its directivity and bandwidth. Several simulations are conducted to investigate the achievement of the cylindrical cup (cyl cup), square cup

(squ cup), and truncated cone (trunc cone) using aluminum sheet material as a ground plane for the model 3a. The 3D visualization design of each reflector is outlined in Fig. 3.10 and their sizes are tabulated in Table 3.3. Simulated achievement of trunc cone reflector shows broader reflection coefficient and AR bandwidth better than the other two types. It also delivers a better gain along frequencies under 2.25 GHz and a worst gain at higher frequencies as detailed in Table 3.4. Trunc cone performs better thanks to its capability to act as a ground plane (which receives and reflects the backside radiation) and also behave as a horn antenna which fed by the ETS antenna simultaneously. Both roles create their independent radiation that acts reciprocally to create the unidirectional pattern [DZI06]. This combination needs 0.5λ of height H to obtain in–phase wave emitted from the lowest part of the horn antenna which improves co–polarization radiation of the antenna. As a result, better front to back ratio and gain is achieved. Meanwhile, height H of quarter-wavelength yields out–phase wave that degrades the achievement by pulling up the AR to around 5 dB. A dissimilar characteristic is performed by scu cup and cyl cup which just have a function as a ground plane, thus need height H of a quarter-wavelength to obtain an in–phase wave. A smaller CP bandwidth is achieved when the height is expanded to a half-wavelength. Comparison of AR profile of trunc cone and squ cup at both different height H is described in Fig. 3.11. The squ cup delivers nearly equal achievement as the cyl cup.

The trunc cone is proposed as a reflector for model 3a thanks to its better performance and covers S–band frequency of microsatellite communication systems. Fabrication of this reflector is conducted using 3D printer technology which provides low cost and better shape close to the design. The 3D printer using Acrylonitrile Butadiene Styrene (ABS) material for printing which has a specification of low–grade electric conductivity. Therefore, a more conductive

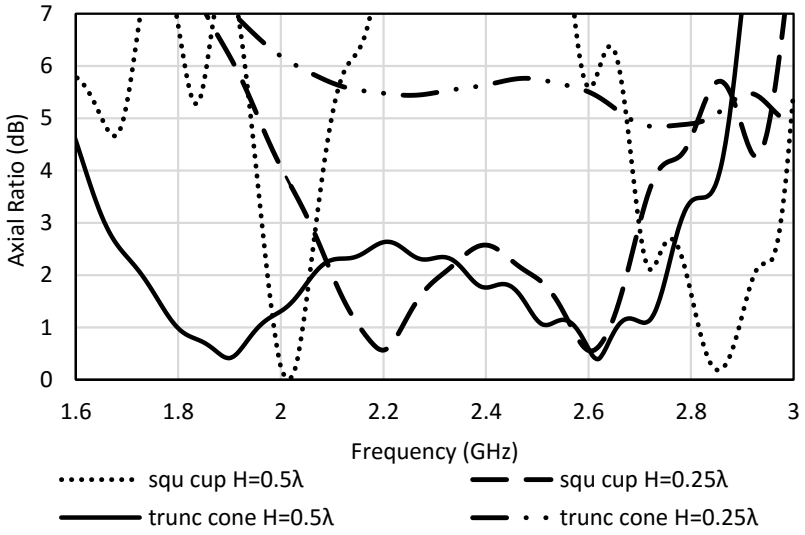

Figure 3.11: Comparison of axial ratio performance at height H of half wavelength and quarter wavelength of simulated squ cup and trunc cone.

Table 3.3: Sizes Of The Simulated Reflectors For Model 3b

Ground Planes	H mm	d_a mm	d_b mm	w_f mm	w_g mm	w_h mm	l_g mm	l_h mm	d_s mm	w_s mm
Aluminium Square Cup	34 ($\lambda/4$)	140	140	6.5	17.3	22	21.6	5	12	11
Aluminium Cylindrical Cup	34 ($\lambda/4$)	154	154	6.5	17.3	22	21.6	5	12	11
Aluminium Truncated Cone	63 ($\lambda/2$)	180	250	6.5	17.3	22	18.6	14	12	13

material is required to coat the printed result. The make use of conductive paint to coat 3D printed horn antennas have been presented and deliver equal impedance and AR bandwidth as copper [CDLR14]. This research utilizes a carbon black polyurethane with electric conductivity of 10^3 S/m to coat to the inner side of the 3D printed trunc cone with a top and bottom radius of 125 mm and 90 mm respectively. The measured performance is compared to the simulated one which has an inner part is coated with aluminum that has an electric conductivity of 3.56 x 10^7 S/m. Model 3a placed on the top of the reflector in this experiment has been changed slightly as its slit size w_s is

Table 3.4: Achievement Of The Simulated Reflectors For Models 3b ETS Antenna, fcibw Impedance Bandwidth Centre Frequency, farbw ARBW Centre Frequency.

Ground Planes	fcibw MHz	Imp BW MHz , %	fcarbw MHz	3–dB ARBW MHz , %
Aluminium Square Cup	2349.4	1962.7–2736 (773.3, 33%)	2378.4	2056.4–2700.4 (644, 27%)
Aluminium Cylindrical Cup	2337	1972.9.2–2701 (728.1, 31%)	2380.4	2052.1–2708.7 (656.6, 27.6%)
Aluminium Truncated Cone	2117	1617.8–2616.2 (998.4, 47%)	2202.7	1658.9–2746.5 (1087.6, 49.4%)

expanded as much 2 mm to achieve better 3–dB ARBW. The fabricated trunc cone as visualized in Fig. 3.10.d is completed with uncoated four pillars same as the simulated one to ensure the precise position of the antenna on top of it.

The application of truncated cone reflector to enhance the gain of model 4a has not been succeeded due to its rectangular dimension. According to simulated results, this type of reflector only works for square printed slot antenna. As a solution for future work, the gain enhancement for model 4a will be tried using array combination, electromagnetic bandgap reflector, artificial magnetic conductor reflector.

3.4 ETS Antenna With Coupled Diagonal Line Slots (Type 2)

The type 2 ETS antenna also use conventional ETRS as its basic design. The conversion of its polarization to circular is conducted also by corner truncation and perturbation insertion. The 3–dB ARBW enhancement is performed by inserting two diagonal line slots.

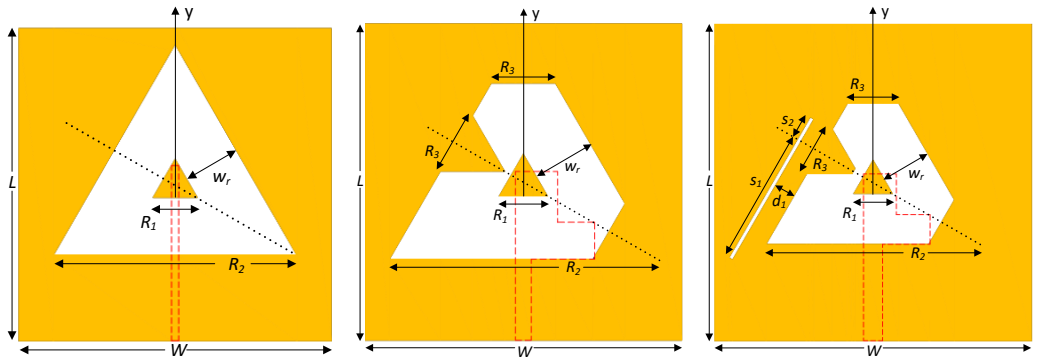

(a) Conv Type 2 ETRS (b) Model 1b ETS (c) Model 2b ETS

Figure 3.12: GeometryStructure of (a) conventional LP of type 2, (b) model 1b and (c) model 2b of ETS antenna [ASSSB16].

Table 3.5: Sizes of Type 2 ETS antenna models

Models	L mm	W mm	w_c mm	w_r mm	R_1 mm	R_2 mm	R_3 mm
Conventional	130	130	3	24	18.3	101.4	-
Model 1b	120	120	6	24	18.3	101.4	24.3
Model 2b	150	150	9	24	18.3	101.4	24.3
Model 3b	150	150	9	24	18.3	101.4	24.3
Model 3b Expanded	170	150	9	24	18.3	101.4	24.3

3.4.1 Conventional ETRS of Type 2 Antenna

Conventional ETRS of type 2 antenna as outlined in Fig. 3.12a performs LP radiation as well. Its center frequency depends on mean perimeter of the slot which related to the slot size w_r and slot side length R_1. As initial value, the inner side length R_1 is set to 18.3 mm, while outer side size R_2 is set to 101.4 mm. The slot size can be calculated as $w_r = \tan 30^{o} \mathrm{x} (R_2 - R_1)/2 = 24$ mm. While mean side length $R_m = (R_2 + R_1)/2 = 59.8$ mm. Therefore, the mean perimeter can be found as $3R_m = 179.5$ mm. The mentioned configuration with antenna size $W = L = 130$ mm produces a center frequency of 1.269 GHz and the mean perimeter is about $0.89\lambda_g$.

3.4.2 CP Generation of Type 2 ETS Antenna

Similar the type 1, CP radiation of this conventional model is produced by transforming the slot geometry and feed line. But this time, only top and bottom left corner of the ETRS are chamfered by R_3 as illustrated in Fig. 3.12b. A grounded equilateral triangular patch with length R_3 is utilized also as a disturbance which has been implemented as well other ring slot antennas [SC11, WHC02]. The size of R_3 determines the center frequency and AR. The larger size of R_3 lessens the slot width thus lower the resonant frequency. The best R_3 size of truncation and disturbance patch to obtain improved AR is 24 mm. The transformed ETRS is excited by branched feed line with a width of 6 mm completed with top and bottom branches expanding to the right. The bottom branch possesses a length of 24 mm and its lowest line must be in a row with the lowest line of ETRS. As for the top branch, its length is set to 10 mm. The length of both branches influences the reflection coefficient and AR bandwidth. A correct tuning is required to match the center frequency of the two bandwidths. Analysis on the distribution of magnetic surface currents indicates that the chamfered corners and disturbance patch produce more surface currents around the chamfered region (see Fig. 3.15a) creating equitable currents distribution than the conventional ETRS which has currents largely distributed on the bottom side of ETS and quite a small current around its upper side. This design, called as model 1b, presents much-improved reflection coefficient bandwidth compared to the conventional model and yields 3-dB ARBW of 254 MHz at 1.727 GHz center frequency. The dimension of all models of type 2 ETS antenna is described in Table 3.5.

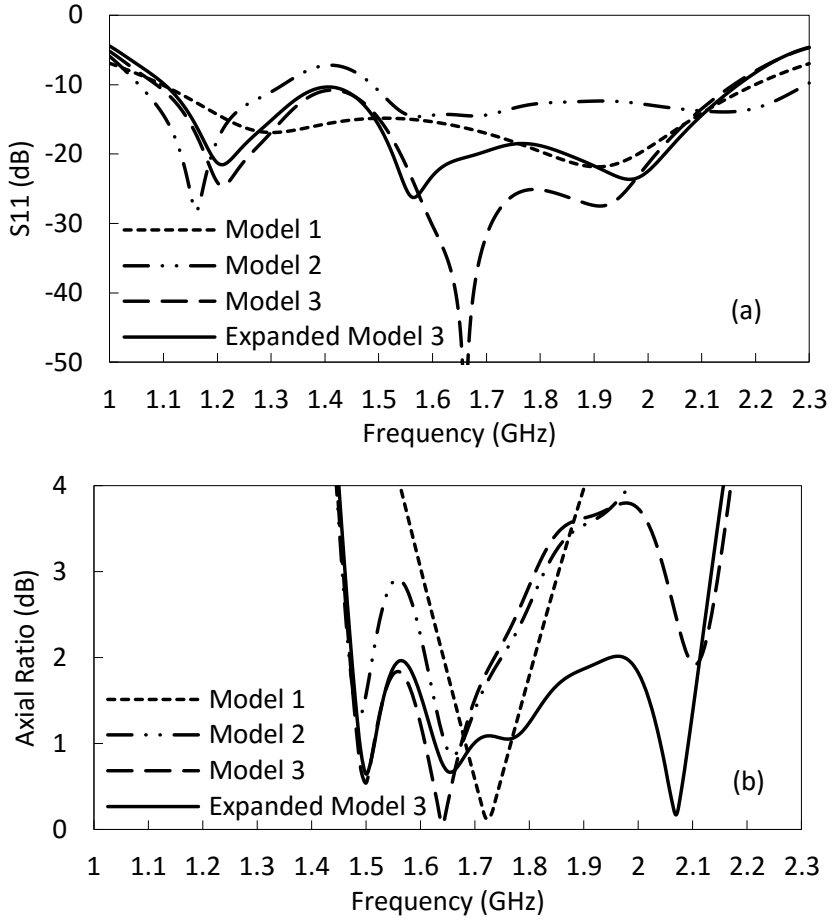

Figure 3.13: Simulated (a) S11 and (b) AR of model 1b, model 2b, model 3b and model 3b expanded of type 2 ETS antenna.

3.4.3 Coupled Diagonal Line Slot For Lower Frequency

Enhancement to the performance of model 1b type 2 ETS antenna is indispensable due to its much smaller 3-dB ARBW than its reflection coefficient bandwidth. The proposed solution is insertion of diagonal line slot as it has proved to excite two degenerate orthogonal modes on patch antenna to perform CP operation [SG83]. However, its application to widen the CP bandwidth has not been presented in the literature. The modified model is called as model 2b and depicted in Fig. 3.12c. The length of narrow line slot determines its first resonant frequency which is equal to $0.5\lambda_g$ similar to a magnetic dipole

Table 3.6: Achievement of model 1b, model 2b, model 3b and model 3b expanded of Type 2 ETS antenna

Models	$f_c ibw$ MHz	Impedance BW MHz , %	$f_c arbw$ MHz	3-dB ARBW MHz , %
Conventional	1269	1100-1438 338 , 26.6%		
Model 1b	1648.5	1097-2200 1103 , 67%	1727	1600-1854 254 , 14.7%
Model 2b	1891	1488-2294 806 , 42.6%	1642	1456-1828 372 , 22.7%
Model 3b	1623	1087-2159 1072 , 66%	1634.5 & 2098	1458-1811 & 2048-2148 353 , 21.6% & 100 , 4.8%
Model 3b exp	1635	1102-2168 1066 , 65.2%	1798	1461-2135 674 , 37.5%

[BS05]. Thus the length of diagonal line slot inserted into the antenna use similar length. Performance of the line slot to widen CP bandwidth is influenced by mutual coupling between it and the ETS. Center position and length of both slots, also field distribution surround the slot are very much govern the results [MP87]. As the line slot delivers little 3-dB ARBW, center frequency of the left line slot is adjusted to be equal to the lowest frequency of model 1b 3-dB ARBW. The slant angle of line slot affects its CP performance and angle of 30^o produces the best result.

Since the CP lowest frequency performed by model 1b is 1.6 GHz, the length of correspond line slot is founded to be approximately 80 mm. Thus, size of each s_1 and s_2 separated by a dotted line and constitute the length of line slot, and distance d_1 influence the mutual coupling between both slots. Thus, an appropriate adjustment is necessary to obtain the highest mutual coupling yielding better axial ratio. Simulated outcome described in Fig. 3.14a show that length of 80 mm constituted by s_1 and s_2 of 66.6 mm and 13.5 mm

respectively, produces broader bandwidth, yet bad AR above 3-dB is yielded. Another s_1 length of 65 mm incorporated with s_2 of 12 mm constitute the slot line length of 77 mm yield smaller bandwidth, yet good AR below 3-dB is achieved. The smaller line slot delivers much smaller 3-dB ARBW as well. Position of the line slot with respect to y–axis created by changing on s_1 and s_2 length as outlined in Fig. 3.14b is influential. Upper position more than s_1 of 65 mm and s_2 of 12 mm rises the bandwidth, yet shift AR worst than 3-dB, while the lower place conduces opposite result. Further, adjustment on d_1 distance by shifting 2 mm farther or closer increase (bad) the AR as highlighted in Fig. 3.14c. The feed line of model 2b is also modified by setting $w_c = 9$ mm and set the length of the top and bottom branches to 22.5 mm and 6.5 mm.

After conducting some simulations, the left line slot length of 77 mm constituted by $s_1 = 65$ mm and $s_2 = 12$ mm with spacing $d_1 = 10$ mm has delivered better performance. These configuration yields 1.45-1.79 GHz bandwidth of AR as outlined in Fig. 3.13 and tabulated in Table 3.6. Fig. 3.15b illustrates the surface currents distribution which shows that mutual coupling between both slots produces more currents in the left line slot compared to model 1b. As a result, two degenerate orthogonal modes of CP operation are generated. Introduction of the left line slot has significantly extended the 3-dB ARBW by covering the lower frequencies and recorded enhancement of 118 MHz or 8% better than model 1b. Mutual admittance of both slots changes the radiation pattern as well, similar to the prediction in [OPZ+13]. The direction of the main beam also turned from 4° by model 1b shifted to -6° by model 2b. It improves the RHCP gain by recording enhancement from 4.55 dBic at 1.7 GHz by model 1b increased to 4.84 dBic at 1.7 GHz and 5.23 dBic at 2 GHz by model 2b. The comparison of radiation pattern and gain of model 1b and

model 2b are described in Fig. 3.16a and Fig. 3.16b respectively.

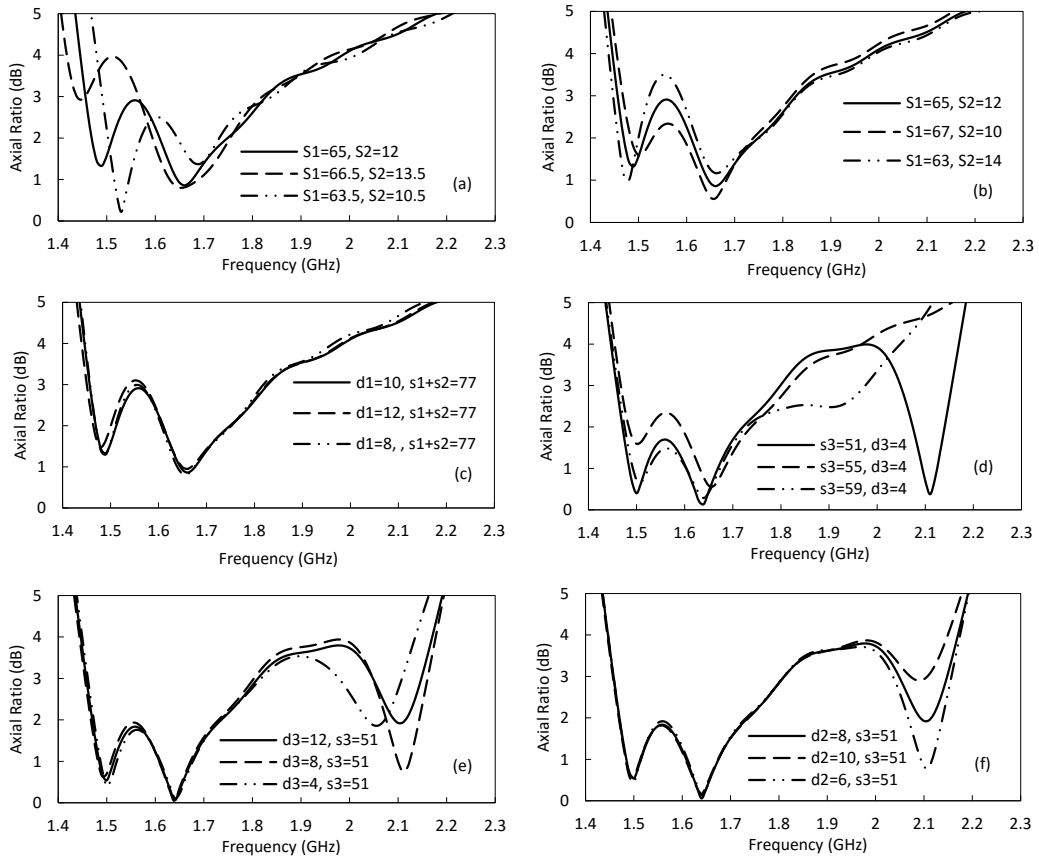

Figure 3.14: Comparison of 3-dB ARBW related to (a) left line slot length with $d_1 = 10$ mm for model 2b, (b) left line slot height position with $d_1 = 10$ mm for model 2b, (c) d_1 with left line slot length = 77 mm for model 2b, (d) right line slot length with $d_2 = 8$ mm for model 3b, (e) right line slot height position with $d_2 = 8$ mm for model 3b, (f) d_2 with $d_3 = 12$ mm for model 3b.

3.4.4 Coupled Diagonal Line Slot For Higher Frequency

Further improvement on CP bandwidth of the model 2b is proposed by introducing additional line slot to the right side of ETS near the truncated corner, then called model 3b. The center frequency of this line slot is adjusted to be approximately highest CP frequency which around 1.828 GHz. However, as the AR achieve 4 dB at 2.16 GHz, quite higher than 1.828 GHz, but seem

possible to enhance 3-dB ARBW from this frequency. Therefore, the appropriate length corresponding to this frequency is around $0.5\lambda_g = 59$ mm. Mutual admittance between both slots determines the CP performance in the new frequencies. It can be tuned by changing the slot length s_3, spacing d_2, and distance d_3. Fig. 3.14.d indicates that the length of 59 mm, which constituted by s_3 of 59 mm d_3 of 4 mm, with distance $d_3 = 8$ mm has successfully widened 3-dB ARBW becomes 520 MHz or 30% fractional bandwidth at 3-dB ARBW center frequency of 1720 MHz. Further, shorter s_3 improves AR bandwidth as well. S_3 size of 51 mm with d_3 of 12 mm produce dual 3-dB ARBW where a new 3-dB ARBW emerges at 2.1 GHz, see Fig. 3.13 and Table 3.6. To achieve a wideband performance, AR values between both bands must be improved to be under 3-dB. As an effort, adjustment on d_2 and d_3 distances while maintaining the s_3 size of 51 mm have been carried out. Shifting the right line slot to a lower position by decreasing d_3 distance narrows the bandwidth, see Fig. 3.14.e. Meanwhile, closer or farther d_2 distance has the small influence to change the bandwidth profile, as illustrated in Fig. 3.14f. Thus, d_2 and d_3 sizes remain at 8 mm and 12 mm. Feed line size of model 3b remains the same as model 2b, but its position is moved 3 mm directed to $+x$.

The mutual admittance successfully produces more surface currents to the area surrounding the right line slot, while lessens currents on the upper right side of ETS to generate two similar-magnitude in-phase quadrature modes, as can be seen in Fig. 3.15.c). The direction of the model 2b main beam is influenced by the right line slot as it slightly shifted as much -1°. However, another drawback is the slight reduction of RHCP gain which becomes 4.7 dBic at 1.7 GHz and 4.9 dBic at 1.9 GHz. The bi–directional radiation and gain performance of model 3b are described in Fig. 3.16a and Fig. 3.16b.

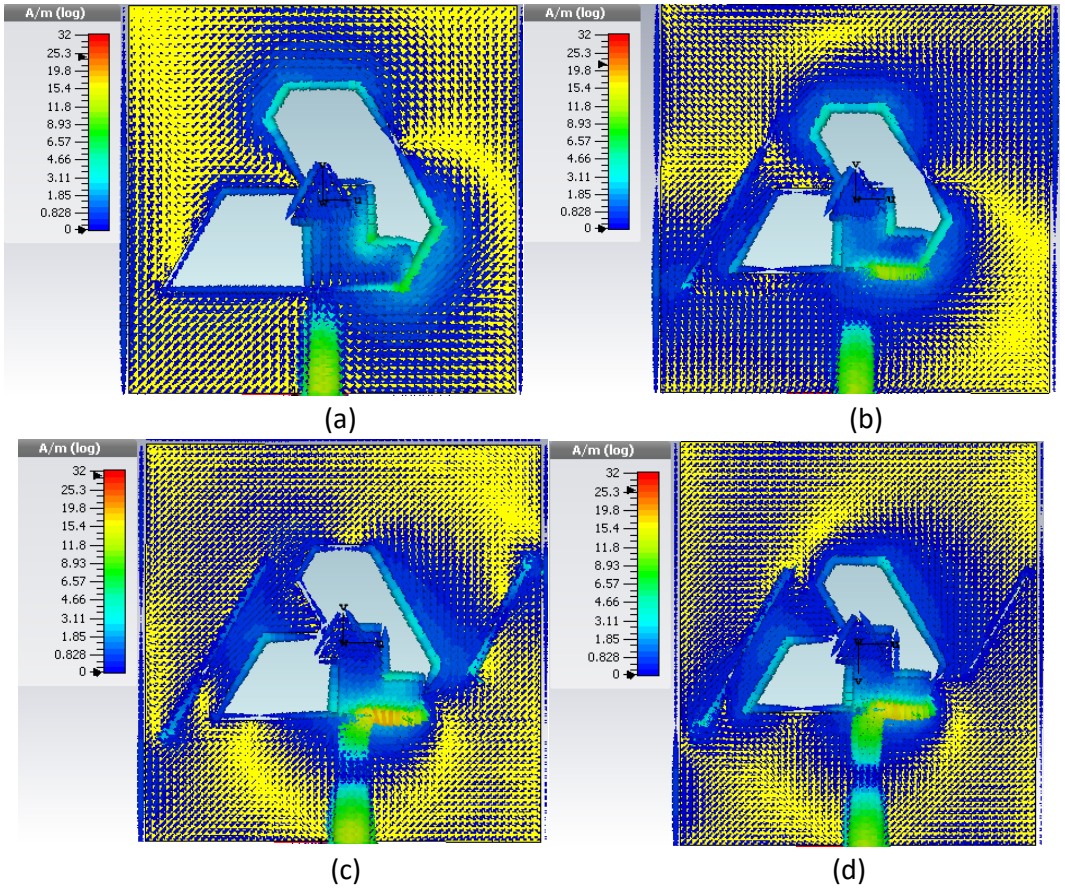

Figure 3.15: Simulated surface currents distribution at 1.8 GHz on (a) model 1b, (b) model 2b, (c) model 3b and (d) model 3b expanded of ETS antenna.

3.4.5 Antenna Length Expansion (Model 3b Expanded)

Adjustment of d_2 and d_3 distances to combine two 3-dB ARBW yielded by model 3b for achieving single wideband performance have been unsuccessful. As a solution, expansion to the length L of the antenna ground proves to solve this problem. Simulated surface currents distributions shows that expansion of 10 mm directed to $+y$ and 10 mm directed to $-y$ provide a wideband performance as the integration of both bands. The expanded model is then called expanded model 3b as illustrated in Fig. 3.17. Sizes of all type 2 ETS models are summarized in Table 3.5. The expanded ground size produces more currents spread on the upper side of ETS to deliver 90 phase discrepancy as

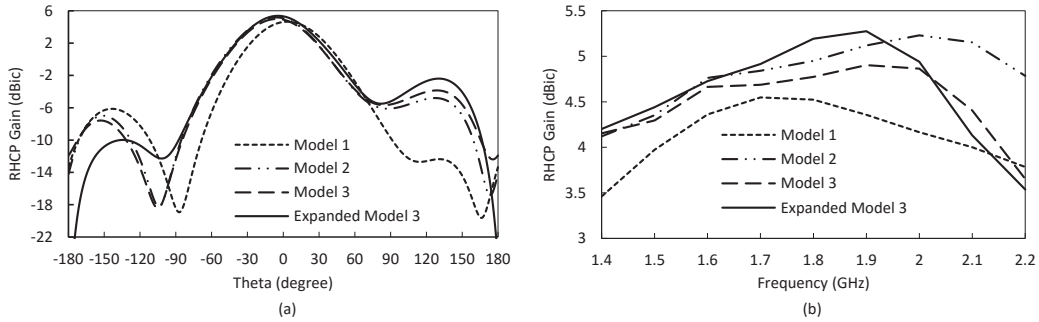

Figure 3.16: Comparison of (a) gains and (b) radiation patterns at 1.8 GHz exhibited by model 1b, model 2b, model 3b and model 3b expanded of ETS antenna.

illustrated in Fig. 3.15d. As an outcome, a wideband CP operation ranging from 1.461 to 2.135 GHz is achieved, as can be seen in Fig. 3.13 and tabulated in Table 3.6. Ground size expansion moves main beam direction by -1°, as highlighted in Fig. 3.16a. It also improves RHCP gain by delivering 4.9 dBic at 1.7 GHz and the better on of 5.28 dBic at 1.9 GHz, as depicted in Fig. 3.16b.

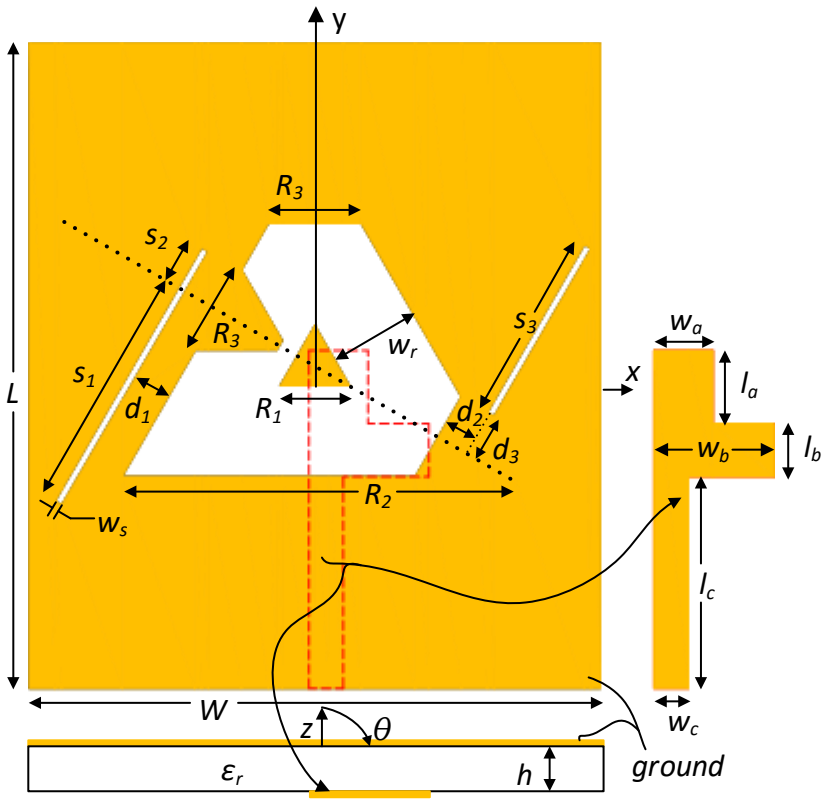

Figure 3.17: Geometry of model 3b expanded of type 2 ETS antenna. Microstrip feed line is projected on the right side and side view is visualized in the bottom part [ASSSB16].

Chapter 4

Experimental Results

This chapter contains the experimental setup, measurement results, and discussion. The measured results will be compared to the simulated one to know whether the fabricated antenna performance meets the requirements.

4.1 Antenna Fabrication and Experimental Setup

After conducting design and simulation to get the best performance prediction of the antenna, the next step is antenna fabrication. The method to manufacture the simulated design by using chemicals is illustrated in Fig. 4.1. To create a layout for fabrication, Draftsight software is required to edit the DXF file imported from CST Studio software. A photosensitive film is prepared to print the layout on both copper side of a printed circuit board by using UV light. The chemicals employed for layout development and etching are GEN-L solution and EB-750 Etchant respectively.

To verify the simulation results, the manufactured model 3a of type 1 ETS

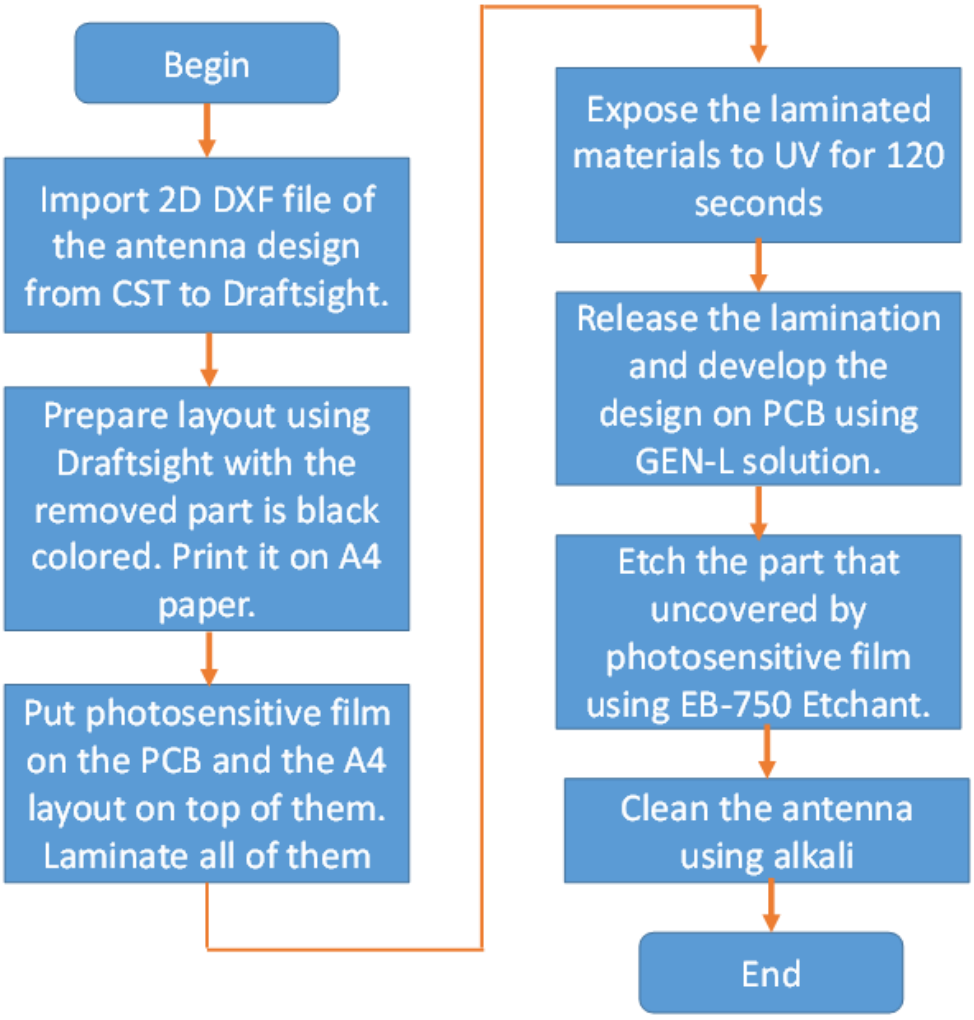

Figure 4.1: Experimental setup of antenna measurement using VNA in anechoic chamber.

and model 3b of type 2 ETS antennas are measured by employing RF Vector Network Analyzer (VNA) (Agilent, E5062A, ENA–L). The measurement is conducted to get data of reflectance coefficient (S_{11}), axial ratio, radiation pattern, and CP gain. The S11 data is obtained by connecting the port of antenna under test (AUT) to port 1 of VNA and measuring the reflection coefficient of the determined frequencies.

The AR is observed by radiating the AUT by RHCP and LHCP tester antennas

respectively over the certain frequency span inside an anechoic chamber. In this case, the port of AUT is connected to port 2 of VNA as a receiver (Rx) and the port of tester antenna is attached to port 1 of VNA as transmitter. The axial ratio value can be calculated using Equation 4.1.

$$AR(dB) = 20log((P_{RHCP} + P_{LHCP})/(P_{RHCP} - P_{LHCP})) \tag{4.1}$$

where AR is axial ratio and P is received power by the AUT as measured by VNA.

To obtain the radiation pattern, the fabricated antennas were illuminated by RHCP and LHCP tester antennas respectively at their x–z ($\theta = 0$) and y–z ($\phi = 90$) planes. During this measurement, the AUT is rotated from 0 until 359 degrees to scan each angle point. The port configuration is similar to the axial ratio measurement. The results are RHCP and LHCP radiation pattern at x–z and y–z planes.

The gain measurement is conducted by radiating the AUT and a standard dipole antenna reference respectively by an RHCP or LHCP tester antennas. The RHCP or LHCP gain of the antenna can be calculated using Equation 4.2 or Equation 4.3 respectively.

$$G_{RHCP}(dBic) = (P_{RHCP}(dB) - P_{Dipole}(dB) + 2.15 - 3) \tag{4.2}$$

$$G_{LHCP}(dBic) = (P_{LHCP}(dB) - P_{Dipole}(dB) + 2.15 - 3) \tag{4.3}$$

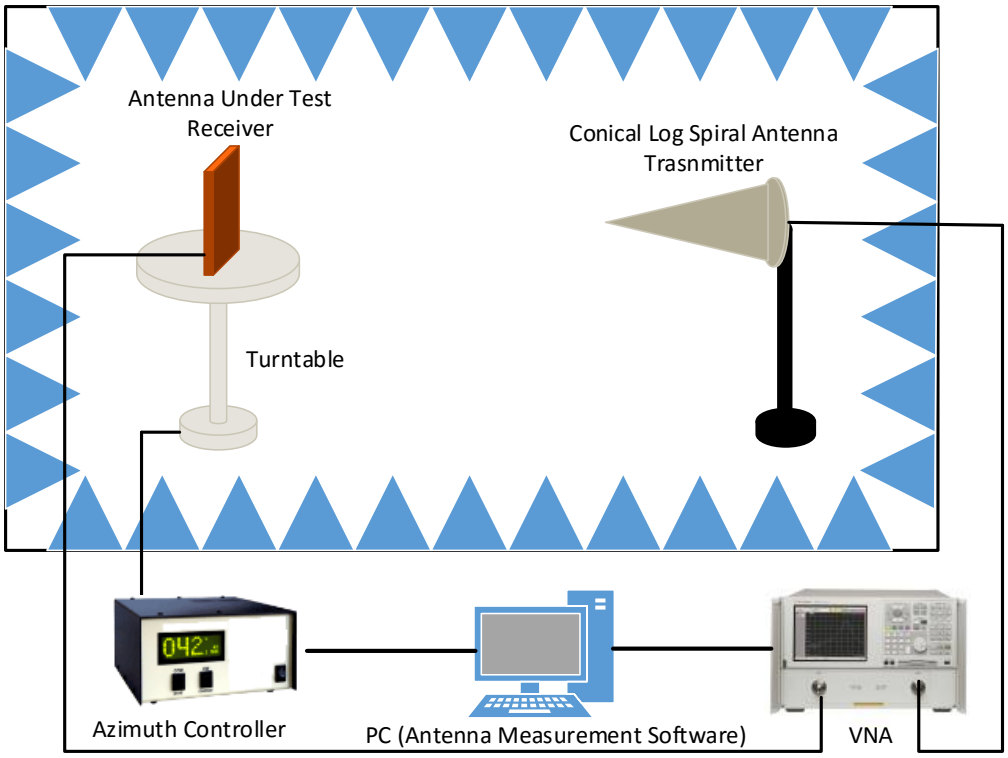

Figure 4.2: Experimental setup of antenna measurement using VNA in anechoic chamber.

where G is a gain of the AUT, 2.15 dB is a half-wave dipole antenna power gain, while -3 dB is gain correction value if CP antenna is compared to dipole antenna over an isotropic source. The illustration of experimental setup can be seen in Fig. 4.2 and Fig. 4.3.

4.2 Measured Results of Type 1 ETS Antenna

The model 3a antenna has been fabricated and its photograph can be seen in Fig. 4.4. While its uni-directional version equipped with the 3D printed trunc cone reflector is shown in Fig. 4.5. The manufactured antenna is measured by employing VNA to examine the simulated results. Fig. 4.6 indicates that S_{11}

Figure 4.3: Photograph of the experimental setup of antenna measurement in an anechoic chamber.

of the simulated (Sim) compared with the measured (Mea) results shows good agreement. Meanwhile, AR of both data shows a dissimilar performance. The measured one delivers 3–dB ARBW of 52.27% better than 43.6% of shown by the simulated. The discrepancy because the fabricated one has wider slot width w_r of several micrometers than that of the simulated. However, the results conclude that bandwidth for CP operation of the manufactured antenna encompasses transmitting and receiving communication systems frequency requirement of the GAIA–I microsatellite.

Meanwhile, measured results of the fabricated model 4a deliver an RHCP operation at 1068–1629 MHz, see Fig. 4.7, and meets the coverage of GNSS–RO frequencies. The measurement of 3–dB ARBW shows two bands dissimilar with the simulated. This discrepancy is caused by fabrication tolerance that influences the feeding magnitude and phase. However, the frequency coverage preserves more than 40% 3–dB ARBW fractional bandwidth similar to the

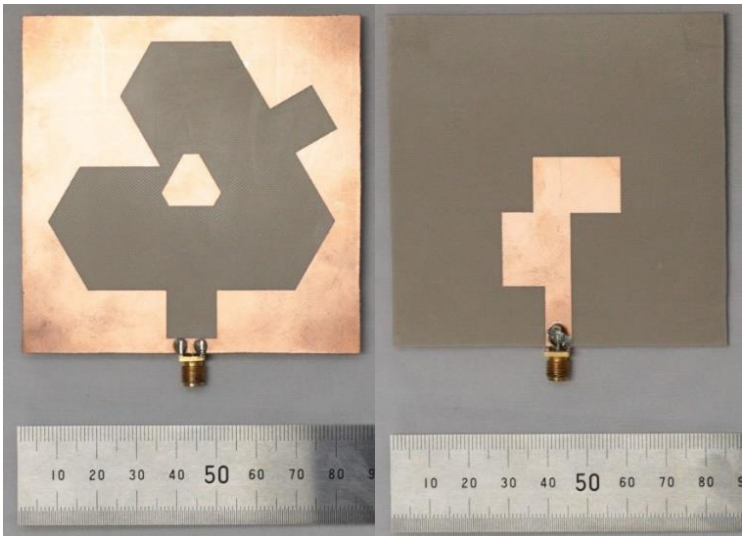

Figure 4.4: Manufactured antenna (a) top side, (b) bottom side of Model 3a.

Figure 4.5: 3D printed truncated cone reflector with model 3a antenna attached on top.

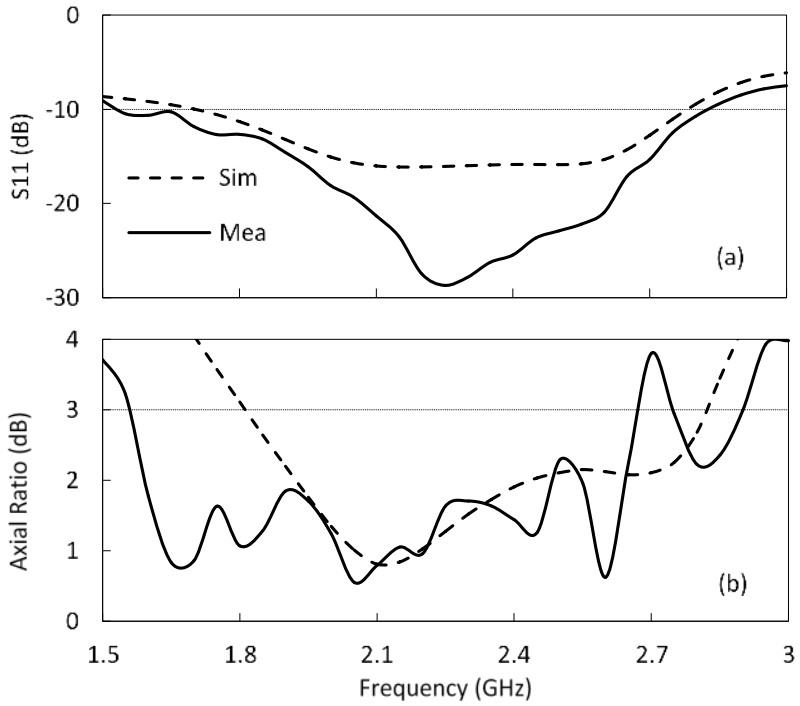

Figure 4.6: Simulation and measurement results of (a) S_{11}, (b) AR of model 3a antenna.

model 3b.

Sizes and performance of the fabricated model 3a are collated with CP slot antennas presented in the literature as tabulated in Table 4.2. The proposed model 3a is classified as a wide slot due to no influence performed by the inner triangular patch on the antenna bandwidth and gain performance. It only affects the resonant frequency in the conventional model. CP operation achievement and sizes of the model 3a surpass wide slot antennas mentioned in Table 4.2, especially equilateral triangular wide slot presented in [HCR08]. The CP bandwidth is only surpassed by [BGS08] thanks to its three times bigger dimension. Compared to ring slot antennas, the performance of the proposed antenna is proportional to [SC11] only if manufactured on FR4 laminate with 0.4 mm thickness which delivers 3-dB ARBW of 49.4% at a center frequency of 1620 MHz. Meanwhile, the CPW antennas provide much broader 3-dB

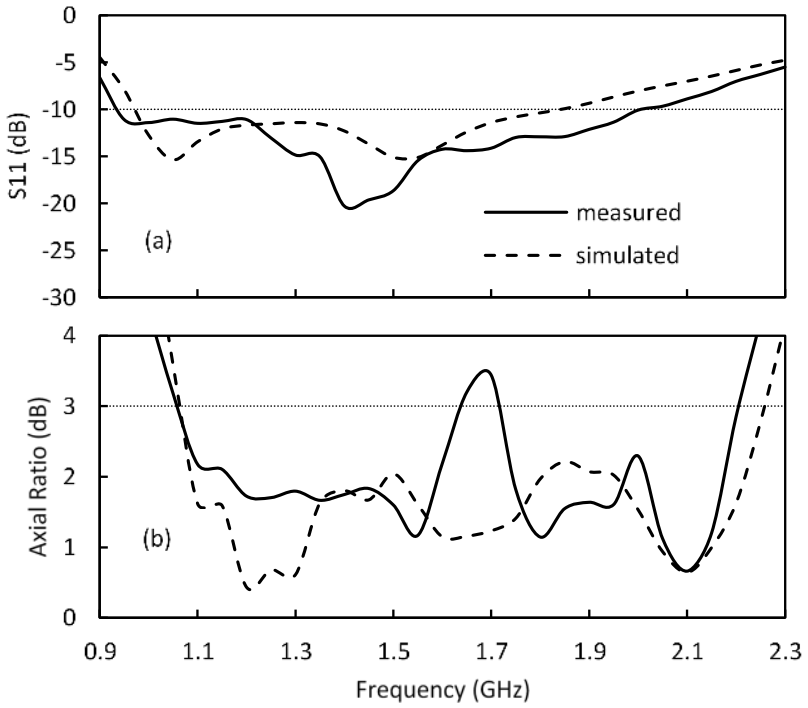

Figure 4.7: Simulation and measurement results of (a) S_{11} and (b) AR of model 4a (GNSS Receiver) antenna.

ARBW as presented in [NCQ11, FNGP11] and show smaller dimension thank their higher operational frequency. Nevertheless, they perform smaller average gain, commonly under 4 dBic compared to 4.5 dBic of the microstrip–line fed.

The unidirectional antenna records wider measured S11 compared to the simulated results, whereas the AR is smaller due to the existence of antenna cable on the top side, dissimilar coating paint and small misalignments of the model 3a antenna placement on top of the reflector, as described in Fig. 4.9. Influence of the antenna cable to 3–dB ARBW performance of the unidirectional structure is illustrated in Fig. 4.8. The existence of the cable decreases the 3–dB ARBW and some of its values close to 3 dB.

Fig. 4.10 indicates the RHCP gain delivered by the simulated and fabricated

Table 4.1: Achievements Of The Simulation And Measurement Results of Type 1 Models, fcibw is Impedance Bandwidth Center Frequency, farbw is ARBW Center Frequency.

Antenna Models	fcibw MHz	Imp BW MHz , %	fcarbw MHz	3–dB ARBW MHz , %
Model 3a	2242.5	1702.1–2782.8 (1080.7, 48.2%)	2317	1811.6–2822.4 (1010.8, 43.6%)
Measured Model 3a	2180.5	1528–2833 (1305, 59.85%)	2116	1563–2669 (1106, 52.27%)
Model 4a	1400	1000–1800 (850, 60.7%)	1675	1100–2250 (1200, 71.6%)
Measured Model 4a	1472.2	940.6–2003.8 (1063.2, 72.2%)	1348.8	1068.2–1629.4 (561.2, 41.6%)

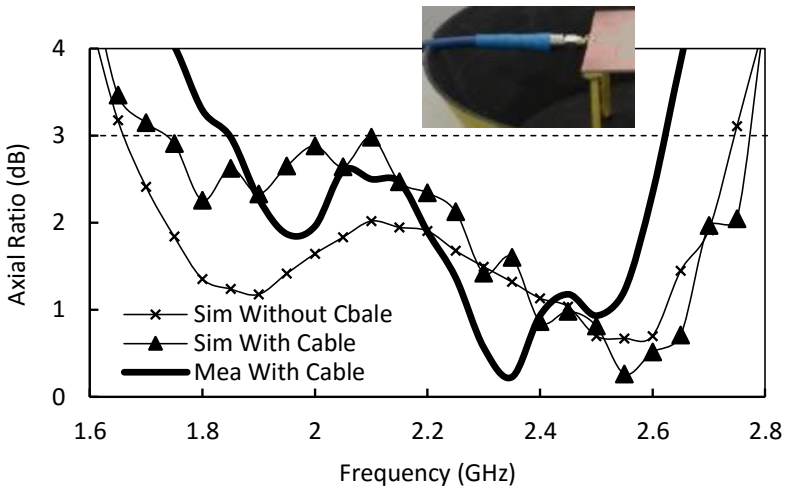

Figure 4.8: Influence of the antenna cable to the CP bandwidth of the unidirectional antenna.

Table 4.2: Comparison of CP achievements of Several Slot Antennas, P is proposed model 3a, CPW is coplanar waveguide, WS is wide slot, RS is ring slot, IBW is impedance bandwidth.

Ref.	type	f_c MHz	3–dB ARBW %	IBW %	Dimension mm
[NCQ11]	CPW	3625	68	107	60x60x1.6
[FNGP11]	CPW	3575	86.4	110	60x60x0.8
[WHC02]	RS	1500	4.3		80x80x1.6
[Row05]	RS	1590	6.3	14.7	54x54x1.6
[SC11]	RS	1638	65	89	100x100x0.6
[HCR08]	WS	3200	31		100x100x15.1
[TH08]	WS	3740	44	38	100x100x1.6
[RW08]	WS	3320	45	45	100x100x1.6
[BGS08]	WS	1650	88.9	77.8	300x300x0.8
[JNF11]	WS	3390	42.5	47.5	–
P	WS	2116	52.3	59.9	84x84x1.6

Table 4.3: Achievements Of Simulation And Measurement Results of Refelectors For Models 3a ETS Antenna, fcibw Impedance Bandwidth Centre Frequency, farbw ARBW Centre Frequency.

Ground Planes	fcibw MHz	Imp BW MHz , %	fcarbw MHz	3–dB ARBW MHz , %
Aluminium Truncated Cone	2117	1617.8–2616.2 (998.4, 47%)	2202.7	1658.9–2746.5 (1087.6, 49.4%)
Measured Truncated Cone	2206	1612–2800 (1188, 53.9%)	2237	1848–2626 (778, 34.8%)

antennas. Measured model 3b antenna presents average gain around the center frequency shows good agreement with the simulated one. Yet the higher gain appears at frequencies between 1.5 and 1.8 GHz thanks to the better 3–dB ARBW and drops drastically at frequencies higher than 2.7 GHz due to the worst 3–dB ARBW, as can be seen in Fig. 4.6. Meanwhile, the manufactured trunc cone ground plane successfully pulls up CP gain of the printed antenna by presenting highest gain at 11.9 dBic.

Measured radiation patterns at far–field of the proposed model 3a show bi–directional pattern with co–polarized RHCP at the forward radiation (+z–direction) and cross–polarized LHCP directed at –z–direction. The simulation and measurement results x–z plane and y–z plane at frequencies between 1.65 and 2.65 GHz are depicted in Fig. 4.11. The much smaller cross–polarization delivered by the printed model 3a at 1.65 GHz proves its better RHCP gain and improved 3–dB ARBW at the same points. Good agreement shown by both data verifies that CP performance of the printed model 3a antenna is as expected.

Fig. 4.12 presents the measurement and simulation results of radiation pattern at a far–field region on both x–z plane and y–z planes of the model 3a ETS antenna equipped with a truncated cone reflector. This antenna and reflector combination is investigated at transmitting and receiving frequency of the command communication systems. Measurement on y–z plane shows that beamwidth of 3–dB axial ratio at 2.075 and 2.25 GHz are more than 30^{o} and directed toward the positive angle. Meanwhile, on x–z plane, the equal beamwidth angle occurs at 2.25 GHz, while at 2.075 GHz it radiates around 25^{o} directed toward the negative angle. Therefore, the beamwidth pattern performed by the combination of the truncated corner reflector and printed

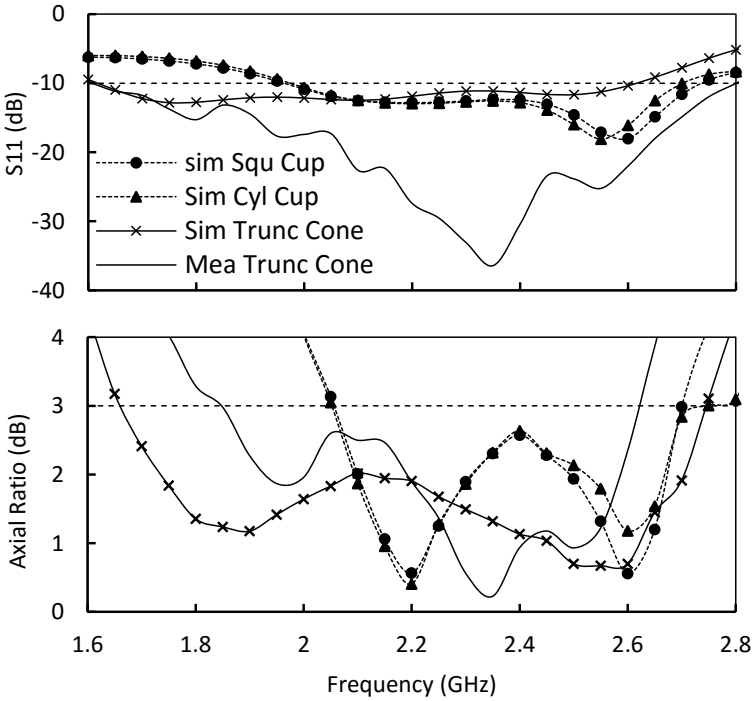

Figure 4.9: Simulation and measurement results of (a) S_{11}, and (b) AR of unidirectional model 3a.

modified model 3a requires an improvement.

4.3 Measured Results of Type 2 ETS Antenna

Simulated model 3b expanded type 2 ETS antenna must be examined to prove the results by conducting fabrication and measurement. Photograph of the printed model 3b can be seen in Fig. 4.13. The measurement of reflection coefficient bandwidth as depicted in Fig. 4.14a records 790 MHz of reflection coefficient bandwidth from 1.39 to 2.18 GHz and shows good agreement with the simulated model. The 3-dB ARBW delivered by the manufactured antenna shows a bandwidth of 680 Mhz from 1.5 to 2.18 GHz almost equal with the simulation results as described in Fig. 4.14b. As the 3-dB ARBW is fully covered by the reflection coefficient bandwidth, the CP bandwidth is similar

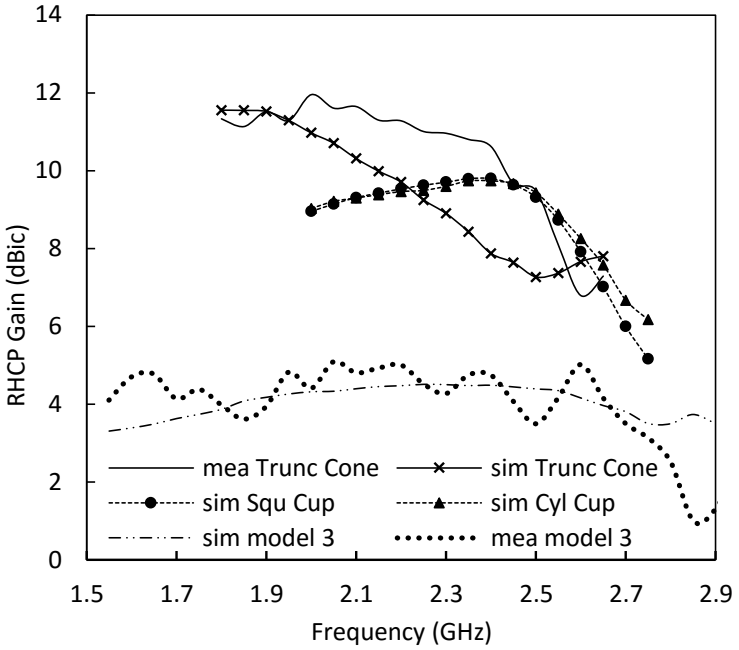

Figure 4.10: Simulation and measurement RHCP gains of model 3b without a ground plane and model 3a with several types of ground planes.

with the 3-dB ARBW, as summarized in Table 4.4.

Fig. 4.16 presents the measurement results of radiation pattern at the far–field for the model 3b expanded ETS antenna after radiated by LHCP and RHCP signals at x-z and y-z planes in an anechoic chamber. The antenna performs bi-directional pattern with LHCP at the backside (–z–direction) (θ=180°) and RHCP as the main beam directed at +z (θ=0°). Measurement of far field radiation patterns on x-z and y-z planes at 1.5 GHz, 1.65 GHz, 1.8 GHz, 1.95 GHz and 2.1 GHz indicates good agreement that verifies the simulation outcome at the similar frequencies. This confirms that the presented antenna performs CP operation as expected at both measurement planes. Fig. 4.15 shows the measurement and simulation results of RHCP gain of the proposed antenna. It shows average gain is approximately 4.9 dBic almost similar to the simulated one with the lowest gain under 4 dBic appear from 2.1 to 2.2 GHz. This confirms that the two diagonal line slots significantly enhances the gain

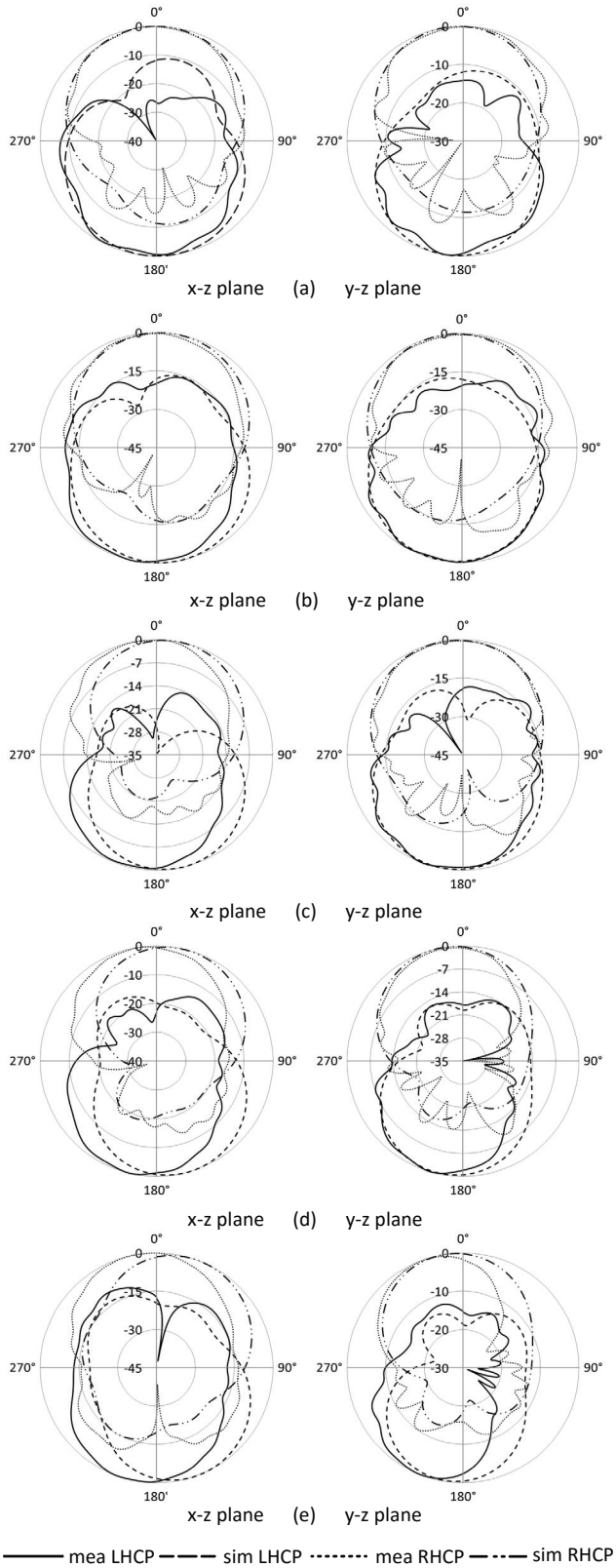

Figure 4.11: Radiation patterns at far-field of the model 3a without ground plane in x–z plane (left side) and y–z plane (right side) at (a) 1.65 GHz, (b) 1.9 GHz, (c) 2.15 GHz, (d) 2.4 GHz and (e) 2.65 GHz.

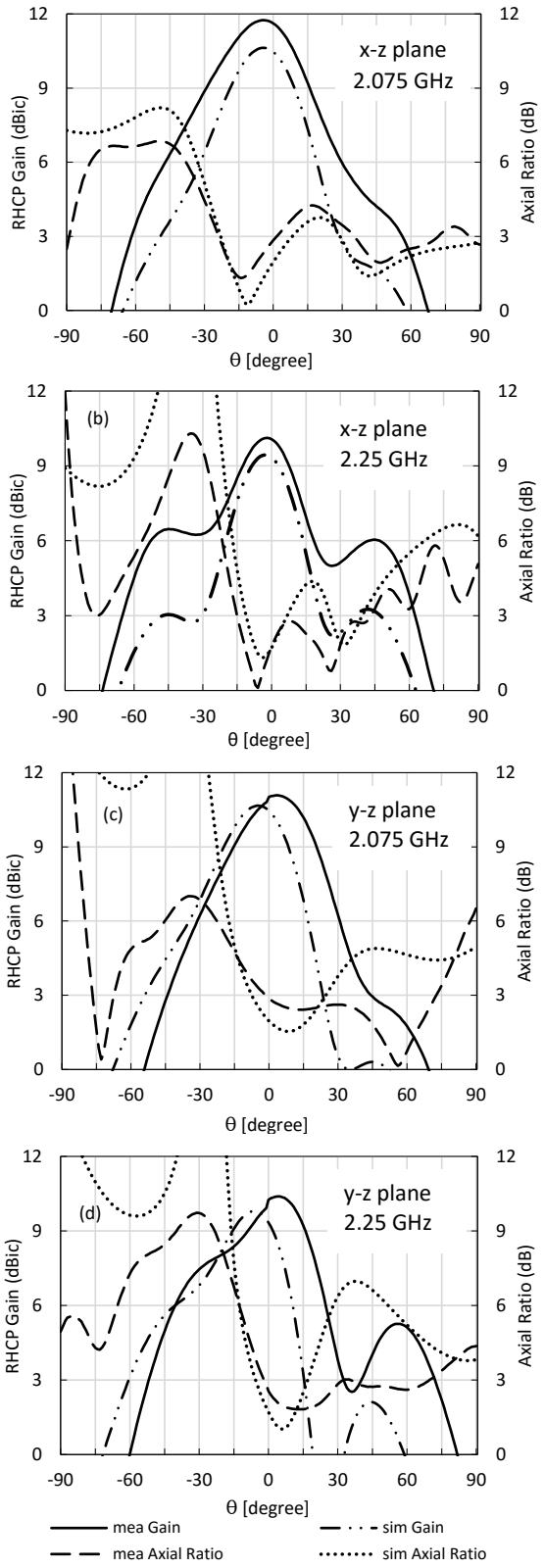

Figure 4.12: RHCP gain and AR of unidirectional model 3a antenna at (a) 2.075 GHz and x–z plane, (b) 2.25 GHz and x–z plane, (c) 2.075 GHz and y–z plane, (d) 2.25 GHz and y–z plane.

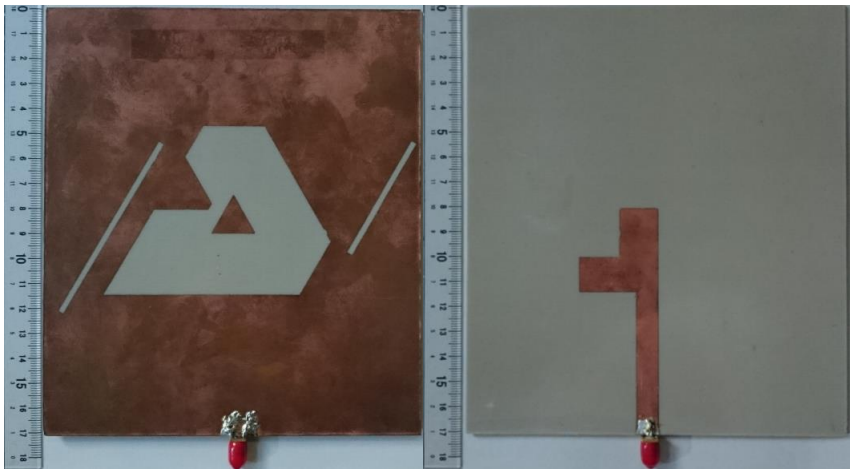

Figure 4.13: Fabricated model 3b expanded ETS antenna.

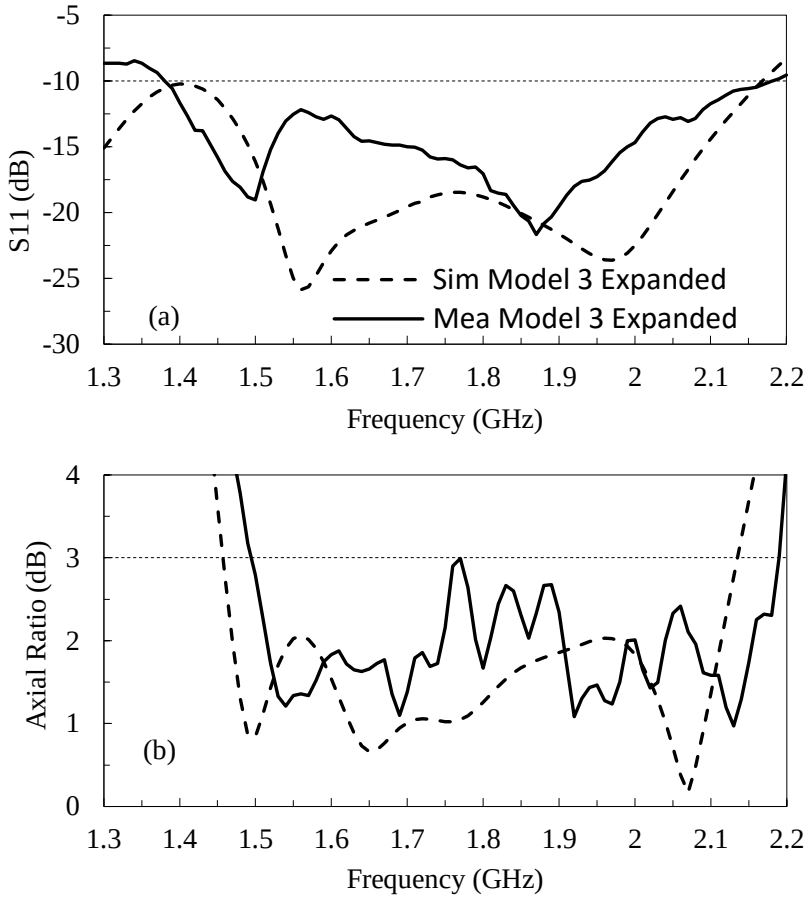

Figure 4.14: Simulation and measurement results of (a) S_{11} and (b) AR of model 3b expanded of ETS antenna.

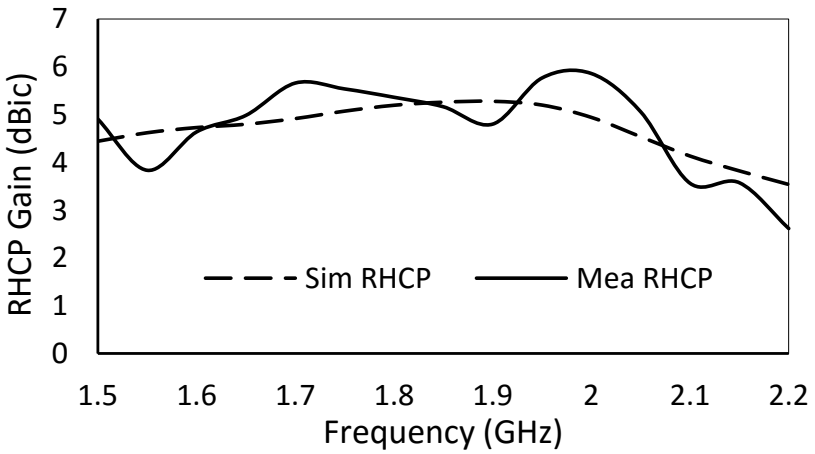

Figure 4.15: RHCP gain of simulation and measurement results of model 3b expanded of ETS antenna.

Table 4.4: Achievements of model 1b, model 2b, model 3b, and model 3b expanded of Type 2 ETS antenna

Models	$f_c ibw$ MHz	Impedance BW MHz , %	$f_c arbw$ MHz	3-dB ARBW MHz , %
Model 3b exp	1635	1102-2168 1066 , 65.2%	1798	1461-2135 674 , 37.5%
Measured Model 3b exp	1785	1390-2180 790 , 44.3%	1840	1500-2180 680 , 37%

of type 2 ETS antenna.

Achievements and sizes of the measured model 3b expanded are collated with several CP microstrip slot antennas as summarized in Table 4.5. The presented ETS antenna type 2 equipped with two diagonal line slots offers wider 3-dB ARBW, smaller CP gain and larger size (on dissimilar resonant frequency) compared to equilateral triangular wide slot incorporated with parasitic patch [HCR08] that shows much larger size. Meanwhile, the proposed antenna offers higher peak and average gain than other mentioned slot antennas.

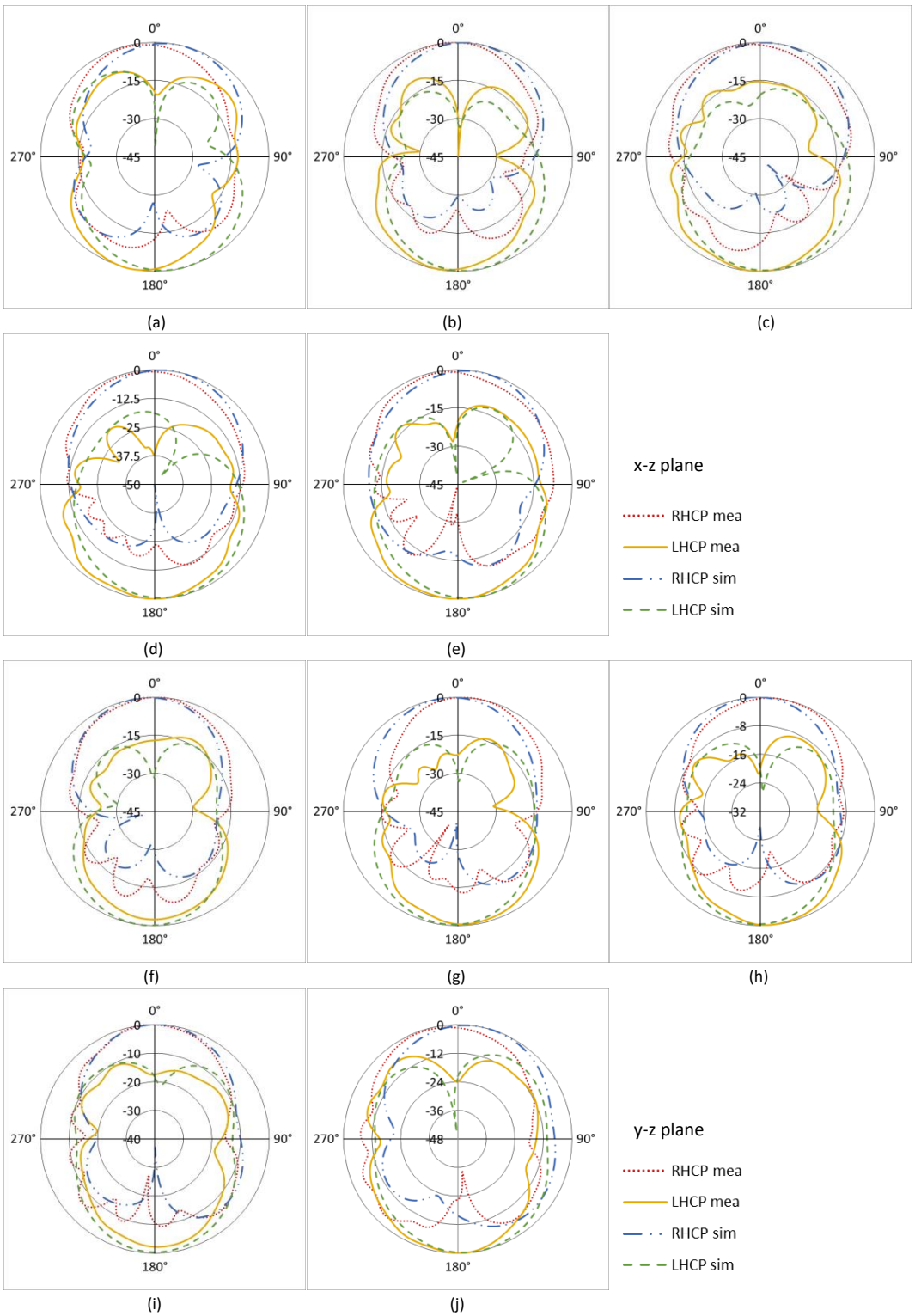

Figure 4.16: Measurement and simulation of radiation patterns results on x-z plane shown by model 3b expanded ETS antenna at (a) 1.5 GHz, (b) 1.65 GHz, (c) 1.8 GHz, (d) 1.95, (e) 2.1 GHz, and y-z plane at (f) 1.5 GHz, (g) 1.65 GHz, (h) 1.8 GHz, (i) 1.95, (j) 2.1 GHz

Table 4.5: Comparison Of CP Microstrip Slot Antenna Achievement

Ref.	f_c (MHz)	3-dB ARBW (%)	Impedance BW (%)	Gain (dBic)	Sizes (mm)
[SHCC10]	2745	48	51	2.6 to 4.2	60x60x0.8
[NCQ11]	3625	68	107	3 to 4	60x60x1.6
[Row05]	1590	6.3	14.7	peak 3.6	54x54x1.6
[WHC02]	1500	4.3		3.5 to 4.3	80x80x1.6
[SC11]	1638	65	89	3.3 to 5.1	100x100x0.6
[WWW99]	2375	12	39	4 to 5.5	120x120x33
[TH08]	3740	44	38	4 to 5	100x100x1.6
[HCR08]	3200	31		average 6.7	100x100x15.1
Proposed	1840	37	44	3 to 5.8	150x170x1.6

Chapter 5

Conclusion and Future Work

5.1 Conclusions

In this research, two types of wideband CP ETS antennas have been developed. Both types make use of a conventional model of ETRS as their initial design. After several modifications, the antennas are classified as a wide slot as their inner patch has no influence on CP performance. The inner patch has an important role only in the basic model as to determine the resonant frequency. However, due to their ring slot shape, they employ CP excitation method implemented for a ring slot. The first type generates CP radiation by implementing truncation on all ETS corner, the introduction of triangular disturbance patch, and deformed feed line. To improve the 3–dB ARBW become similar to the impedance bandwidth, it requires the introduction of a pair of slits. It can be confirmed that the pair of the slits has a significant impact to double the 3-dB ARBW and decrease the antenna size. The LHCP design of the RHCP antenna can be created by shifting the disturbance patch, the slit on the right side, and the branches of the feed line to the opposite

position. This design is developed for the command communication systems and GNSS–RO sensor of GAIA–I. The measured results of the antenna for a communication system (model 3a) confirm good performance with CP bandwidth around 52.27%. The 3–dB ARBW and sizes of this antenna exceed other microstrip–line–fed wide slot antennas and proportional to annular–ring slot with wider slot size and hat–shaped perturbation patches. The proposed ETS antenna for the GNSS–RO receiver can be created by tuning the slot size and feed line dimension of model 3a become larger. The design successfully attains 3–dB ARBW of 41.6% and fully covers GNSS frequencies. The unidirectional radiation pattern is produced by installing 3D printed truncated cone reflector with a height of 0.5λ underneath. The reason for the height is to obtain an in–phase wave emitted back from the lowest part of the reflector acting as a horn antenna to enhance the forward radiation. This configuration improves antenna performance by reaching peak RHCP gain of 11.9 dBic. Yet, the beamwidth of the 3-dB axial ratio shows by this unidirectional radiation requires improvement to radiate on the similar angle at the S-band communication frequencies.

Meanwhile, for the second type, the polarization of the conventional ETRS antenna is altered to circular by implementing truncations on two corners and insertion of disturbance patch, resulting in an ETS antenna. However, this modified design (model 1b) yields smaller 3-dB ARBW than to its reflection coefficient bandwidth. The improvement can be created by introducing dual diagonal line slots with their center frequency related to the lowest and highest CP frequencies of the ETS antenna. The dual diagonal line slots in expanded model 3b have significantly enhanced 3-dB ARBW by performing 680 MHz or 37% than 254 MHz or 14.7% produced by model 1b. It has been verified also that the dual line slots have enhanced the RHCP gain by reaching the average

of 4.9 dBic. Therefore, the proposed antenna can be applied to wideband CP antenna application such as GNSS receiver and communications systems of the satellite.

5.2 Contributions

This dissertation makes novel contributions to the field of wideband CP antenna by discovering methods to broaden CP bandwidth and gain of ETS antenna.

The specific contributions presented in this research are summarized as follows:

1. We have designed and developed a pair of slits to enhance CP bandwidth of the truncated corners and perturbed ETS antenna. It can be confirmed that the pair of the slits has a significant impact to double the 3-dB ARBW and decrease the antenna size.

2. We have designed and developed the coupled two diagonal line slots to enhance CP bandwidth of the truncated corners and perturbed ETS antenna. The longer diagonal line slot widens the CP bandiwdth to the lower frequencies, while the shorter one broadens to the higher region.

3. We have designed and developed a truncated cone reflector to enhance CP gain of ETS antenna with a pair of slits exceeding CP gain achieved by cylindrical and square cup reflector.

5.3 Future Works

The results presented in this thesis may be extended in a variety of ways. Following is a list of some possible works:

1. Development of low profile reflector by employing electromagnetic band gap (EBG) or artificial magnetic conductor (AMC) technique to enhance CP bandwidth in almost equal gain in the GNSS frequency.

2. Development of array ETS antenna to obtain improved gain and better side lobe.

Bibliography

[AEH+08] R.A. Anthes, D. Ector, D.C. Hunt, Y-H. Kuo, C. Rocken, W.S. Schreiner, S.V. Sokolovskiy, S Syndergaard, T-K. Wee, Z. Zeng, P.A. Bernhardt, K.F. Dymond, Y. Chen, H. Liu, K. Manning, W.J. Randel, K.E. Trenberth, L. Cucurull, S.B. Healy, S-P. Ho, C McCormick, T.K. Meehan, D.C. Thompson, and N.L. Yen. The COSMIC/FORMOSAT-3 Mission: Early Results. *Bulletin of the American Meteorological Society*, 89:313–333, 2008.

[ASSI+18] Asif Awaludin, Josaphat Tetuko Sri Sumantyo, Koichi Ito, Steven Gao, M.Z. Baharuddin, and Cahya Edi Santosa. Equilateral Triangular Slot Antenna For Communication System And GNSS RO Sensor Of GAIA-I Microsatellite. *IEICE TRANSACTIONS on Communications*, E101-B(3):–, 2018.

[ASSSB16] Asif Awaludin, Josaphat Tetuko Sri Sumantyo, Cahya Edi Santosa, and M.Z. Baharuddin. Axial Ratio Enhancement of Equilateral Triangular-Ring Slot Antenna Using Coupled Diagonal Line Slots. *Progress In Electromagnetics Research C*, 70:99–109, 2016.

[BAM10] X.L. Bao, M.J. Ammann, and P. McEvoy. Microstrip–fed Wideband Circularly Polarized Printed Antenna. *IEEE Trans. Anten-*

nas Propag., 58(10):3150–3156, 2010.

[BGS08] L. Bian, Y.X. Guo, and X.Q. Shi. Wideband circularly polarised slot antenna. *IET Microwaves, Antennas and Propag.*, 2(5):497–502, 2008.

[BS05] N. Behdad and K. Sarabandi. A Wide-band Slot Antenna Design Employing A Fictitious Shot Circuit Concept. *IEEE Trans. Antennas Propag.*, 53(1):475–482, 2005.

[CCR05] T.Y. Chen, L.Y. Chu, and J.S. Row. Studies of CPW–Fed Equilateral Triangular–Ring Slot Antennas and Triangular-Ring Slot Coupled Patch Antennas. *IEEE Trans. Antennas Propag.*, 53(7):2208–2211, 2005.

[CDLR14] J.C.S. Chieh, B. Dick, S. Loui, and J.D Rockway. Development of a KuBand Corrugated Conical Horn Using 3D Print Technology. *IEEE Antennas and Wireless Propag. Let.*, 13:201–204, 2014.

[CL11] T.N. Chang and J.M. Lin. Circularly Polarized Antenna Having Two Linked Slot-Rings. *IEEE Trans. Antennas Propag.*, 59(8):3057–3060, 2011.

[CLL13] Eun-cheol Choi, Jae W. Lee, and Taek-Kyung Lee. Modified S–Band Satellite Antenna With Isoflux Pattern and Circularly Polarized Wide Beamwidth. *IEEE Antennas and Wireless Propagation Letters*, 12:1319 – 1322, 2013.

[CLLL14] Eun-cheol Choi, Jae W. Lee, Taek-Kyung Lee, and Woo-Kyung Lee. Circularly Polarized S–Band Satellite Antenna With Parasitic Elements and Its Arrays. *IEEE Antennas and Wireless Propagation Letters*, 13:1689 – 1692, 2014.

[CW99] H.M. Chen and K.L. Wong. On the circular polarization operation of annular–ring microstrip antennas. *IEEE Trans. Antennas Propag.*, 47(8):1289–1292, 1999.

[DZI06] A.R. Djordjevic, A.G. Zajic, and M.M. Ilic. Enhancing The Gain of Helical Antennas by Shaping The Ground Conductor. *IEEE Antennas and Wireless Propag. Let.*, 5(1):138–140, 2006.

[FNGP11] Nader Felegari, J. Nourinia, C. Ghobadi, and J. Pourahmadazar. Broadband CPW–Fed Circularly Polarized Square Slot Antenna With Three Inverted–L–Shape Grounded Strips. *IEEE Antennas and Wireless Propagation Letters*, 10:274–277, 2011.

[GGTC12] Ivan Gonzalez, Josefa Gmez, Abdelhamid Tayebi, and Felipe Ctedra. Optimization of a Dual-Band Helical Antenna for TTC Applications at S Band. *IEEE Antennas and Propagation Magazine*, 54(4):63 – 77, 2012.

[GLZ14] Steven Gao, Qi Luo, and Fuguo Zhu. *Circularly Polarized Antennas*. John Wiley '&' Sons, Ltd, nov 2014.

[HCR08] T.Y. Han, L.Y. Chu, and J.S. Row. Unidirectional circularly–polarized slot antennas with broadband operation. *IEEE Trans. Antennas Propag.*, 56(6):1777–1780, 2008.

[Hus12] K.F.A Hussein. Conical linear spiral antenna for tracking, telemetry and command of low earth orbit satellites. *Progress In Electromagnetics Research C*, 29:97–107, 2012.

[IGB10] William A. Imbriale, Steven Gao, and Luigi Boccia. *Space Antenna Handbook*. John Wiley '&' Sons, Ltd, may 2010.

[JCX13] Shuanggen Jin, Estel Cardellach, and Feiqin Xie. *Theory of GNSS Radio Occultation*. Springer, Dordrecht, aug 2013.

[JNF11] R. Joseph, S. Nakao, and T. Fukusako. Wideband circularly polarised slot antennaBroadband Square Slot Antenna for Circular Polarization with Separated L-Probes and Stubs in the Slot. *IEICE TRANSACTIONS on Communications*, E94-B(4):951–959, 2011.

[MAM+08] A.J. Mannucci, C.O. Ao, T.K. Meehan, B.A. Iijima, A. Komjathy, T.P. Yunck, M.K. Pestana, and B.D. Wilson. GPS Radio Occultation as Part of the Global Earth Observing System. In *Geoscience and Remote Sensing Symposium, 2008. IGARSS 2008*, pages 308–311. IEEE, jul 2008.

[MP87] G. Mazzarella and G. Panariello. On the Evaluation of Mutual Coupling Between Slots. *IEEE Trans. Antennas Propag.*, AP-35(11):1289–1293, 1987.

[MSSA+16] Takahiro Miyazaki, Josaphat Tetuko Sri Sumantyo, Takumi Abe, Tomoyuki Nakazono, and Koh-Ichiro Oyama. Controlling the Electric Potential of the Low-Earth Orbit Microsatellite in Ionosphere Observation via Langmuir Probe. *Journal of Instrumentation, Automation and Systems*, 3(1):7 – 13, 2016.

[NCQ11] Nasimuddin, Zhi Ning Chen, and Xianming Qing. Symmetric–Aperture Antenna for Broadband Circular Polarization. *IEEE Trans. Antennas Propag.*, 59(10):3932–3936, 2011.

[OPZ+13] I.M. Ortego, M.S. Perez, M. Zhang, J. Hirokawan, and M. Ando. Mutual Coupling In Longitudinal Arrays Of Compound Slots. *Progress In Electromagnetics Research B*, 46:59–78, 2013.

[QC99] X.M. Qing and Y.W.M. Chia. Circularly Polarized Circular Ring Slot Antenna Fed By Stripline Hybrid Coupler. *Electronics Letters*, 35(25):2154–2155, 1999.

[Row05] Jeen-Sheen Row. The design of a squarer–ring slot antenna for circular polarization. *IEEE Trans. Antennas Propag.*, 53(6):1967–1972, 2005.

[RSW+13] J. Rosello, P. Silvestrin, R. Weigand, S. dAddio, A. Garcia Rodriguez, and G. Lopez Risueno. Next generation of ESA's GNSS receivers for Earth Observation satellites. In *6th ESA Workshop on Satellite Navigation Technologies (NAVITEC) 2012*, pages 1–10. IEEE, feb 2013.

[RW08] J.S. Row and S.W. Wu. Circularly–polarized wide slot antenna loaded with a parasitic patch. *IEEE Trans. Antennas Propag.*, 56(9):2826–2832, 2008.

[SC11] Jia-Yi Sze and Wei-Hung Chen. Axial-Ratio-Bandwidth Enhancement of a Microstrip-Line-Fed Circularly Polarized Annular-Ring Slot Antenna. *IEEE Transactions on Antennas and Propagation*, 59(7):2450 – 2456, 2011.

[SG83] P. Sharma and K. Gupta. Analysis and optimized design of single feed circularly polarized microstrip antennas. *IEEE Trans. Antennas Propag.*, 31(6):949–955, 1983.

[SHCC10] J.Y. Sze, C.I.G. Hsu, Z.W. Chen, and C.C. Chang. Broadband CPW-fed circularly polarized square slot antenna with lightening-shaped feed-line and inverted-L grounded strips. *IEEE Trans. Antennas Propag.*, 58(3):973–977, 2010.

[SHHO07] J.Y. Sze, C.G Hsu, M.H. Ho, and Y.H. Ou. Design of Circularly Polarized Annular–Ring Slot Antennas Fed by a Doble–Bent Microstripline. *IEEE Trans. Antennas Propag.*, 55(11):3134–3139, 2007.

[SR14] Brandan T. Strojny and Roberto G. Rojas. Bifilar Helix GNSS Antenna for Unmanned Aerial Vehicle Applications. *IEEE Antennas and Wireless Propagation Letters*, 13:1164 – 1167, 2014.

[SSI15] Josaphat Tetuko Sri Sumantyo and Nobuyoshi Imura. Development of GNSS-RO and EDTP sensors onboard microsatellite for ionosphere monitoring. In *2015 IEEE International Geoscience and Remote Sensing Symposium*, pages 4886–4889. IEEE, jul 2015.

[SZL15] Chao Sun, Huili Zheng, and Ying Liu. Compact dual-band circularly polarised GNSS antenna. *Electronics Letters*, 51(20):1559 – 1560, 2015.

[TH08] L.Y. Tseng and T.Y. Han. Microstrip–fed circular slot antenna for circular polarization. *Microw. Opt. Technol. Lett.*, 50(4):1056–1058, 2008.

[TYM12] Dmitry Turbiner, Larry E. Young, and Tom K. Meehan. Phased Array GNSS Antenna for the FORMOSAT-7/COSMIC-2 Radio

Occultation Mission. In *ION GNSS 2012 Conference*, pages 1–3. Institute of Navigation; Washington, DC, United States, sep 2012.

[WHC02] K.L.C. Wong, C. Huang, and W.S. Chen. Printed ring slot antenna for circular polarization. *IEEE Trans. Antennas Propag.*, 50(1):75–77, 2002.

[WWW99] K.L. Wong, J.Y. Wu, and C.K. Wu. A circular-polarized patch loaded square slot antenna. *Microw. Opt. Technol. Lett.*, 23(6):363365, 1999.

[YFC+10] Nick L. Yen, Chen-Joe Fong, Chung-Huei Chu, Jiun-Jih Miau, Yuei-An Liou, and Ying-Hwa Kuo. *Global GNSS Radio Occultation Mission for Meteorology, Ionosphere and Climate.* InTech, jan 2010.

Acknowledgements

First of all, I would like to express my gratitude to my academic supervisor, Profesor Josaphat Tetuko Sri Sumantyo, for his guidance in conducting this research so that I can complete my doctoral program in time. I would like also to thank my laboratory mates in the Josaphat Microwave Remote Sensing Laboratory for their helpful assistances. Like wise, I would like also to thank my wife, children, families, and colleagues in LAPAN Indonesia for their continuous support during my study in Japan.

I am very thankful to the Ministry of Research, Technology, and Higher Education Indonesia for the doctoral program scholarship under Program for Research and Innovation in Science and Technology (RISET-Pro).

This research is supported in part by the Japan Science and Technology Agency (JST) – Japan International Cooperation Agency (JICA) FY2010 – 2016 Science and Technology Research Partnership for Sustainable Development (SATREPS); the European Space Agency (ESA) Earth Observation Category 1 under Grant 6613; the 4th Japan Aerospace Exploration Agency (JAXA) ALOS Research Announcement under Grant 1024; the 6th JAXA ALOS Research Announcement under Grant 3170; the Japanese Government National Budget – Ministry of Education and Technology (MEXT) FY2015–2017 under Grant 2101; Chiba University Strategic Priority Research Promotion Program FY2016–FY2018; Taiwan National Space Organization (NSPO); and Indonesian National Institute of Aeronautics and Space (LAPAN).

Appendix A

Publications List

A.1 Peer–reviewed journal papers

1. Asif Awaludin, Josaphat Tetuko Sri Sumantyo, Cahya Edi Santosa, Mohd Zafri Baharuddin, Axial Ratio Enhancement of Equilateral Triangular-Ring Slot Antenna using Coupled Diagonal Line Slots, Progress In Electromagnetics Research C (PIERC), Vol. 70 ¿ pp. 99-109, 7 December 2016 [Link] ISSN 1937-8718, DOI:10.2528/PIERC16102508

2. Asif Awaludin, Josaphat Tetuko Sri Sumantyo, Koichi Ito, Steven Gao, Achmad Munir, Mohd Zafri Baharuddin, and Cahya Edi Santosa, Equilateral Triangular Slot Antenna For Communication System And GNSS RO Sensor Of GAIA-I Microsatellite, IEICE Transactions on Communications, Vol.E101-B,No.3,pp.-,Mar. 2018, 1 September 2017. DOI http://doi.org/10.1587/transcom.2017EBP3183

A.2 Conference papers

1. Asif Awaludin, Josaphat Tetuko Sri Sumantyo, Steven Gao, Cahya Edi Santosa, and Mohd Zafri Baharuddin. Wideband circularly polarized triangular-ring slot antenna for GAIA-I microsatellite, 11th European Conference on Antennas and Propagation (EUCAP), 19-24 March 2017, DOI: 10.23919/EuCAP.2017.7928040

Appendix B

Software For Antenna Design and Simulation

CST MICROWAVE STUDIO® (CST MWS) provides several effectice solver modules. Morover, beside its prominent time domain solver primely presenting the PERFECT BOUNDARY APPROXIMATION (PBA)®, CST MWS also inserted modules based on a lot of disctinction methods such as finite element method (FEM), method of moments (MoM), multilevel fast multipole method (MLFMM) and shooting boundary ray (SBR), each providing different benefites in their particular domains.

CST MWS offers numerous simulation approach enables the user to easyly chose the most suitable solver to solve their design problems, such as transient solver, frequency domain solver, eigenmode solver, resonant solver, integral equation solver, asymptotic solver, and TLM solver.

Below is the example of step by step design and simulation of microstrip equilateral triangular ring slot antenna using CST MWS

1. Select New Project on CST MWS, this below form will appear and then select MW & RF & OPTICAL, the right side menu will show up. Select Antenna option and click Next button.

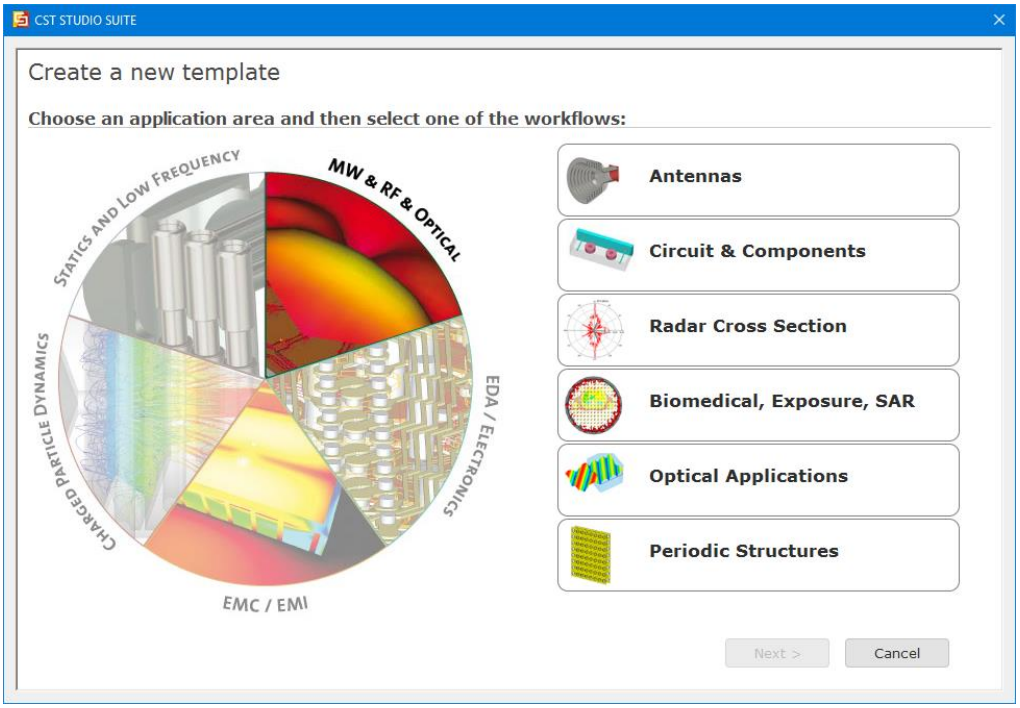

2. The new form will appear, select Planar (Patch, Slot, etc.) and click Next button.

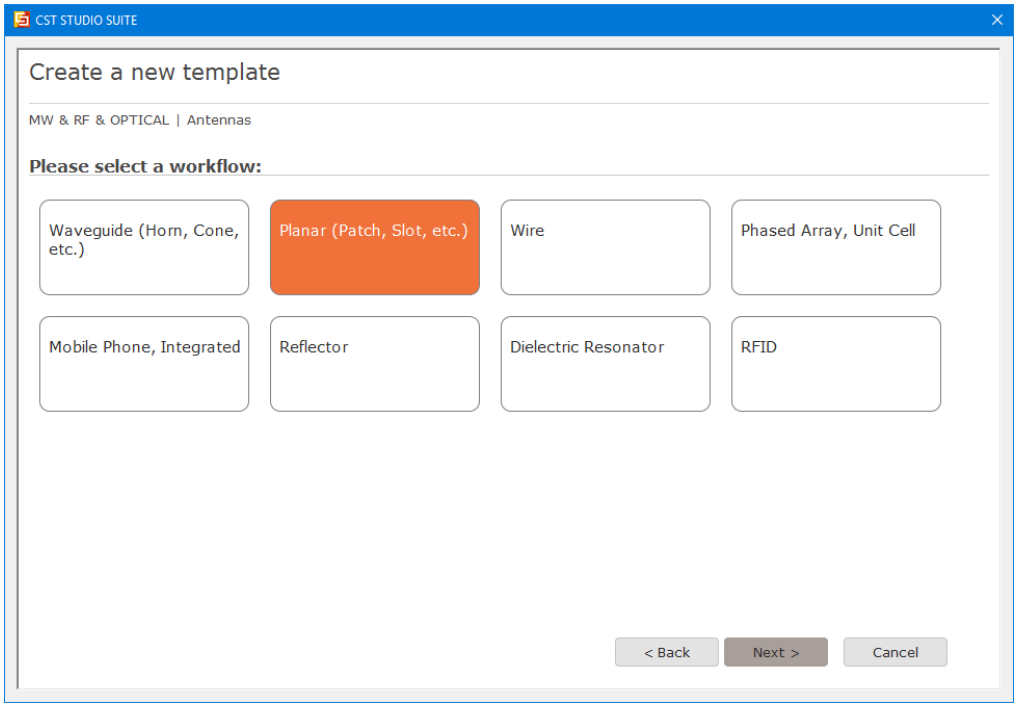

3. Next, choose Time Domain for wideband or multiband antennas and click Next button.

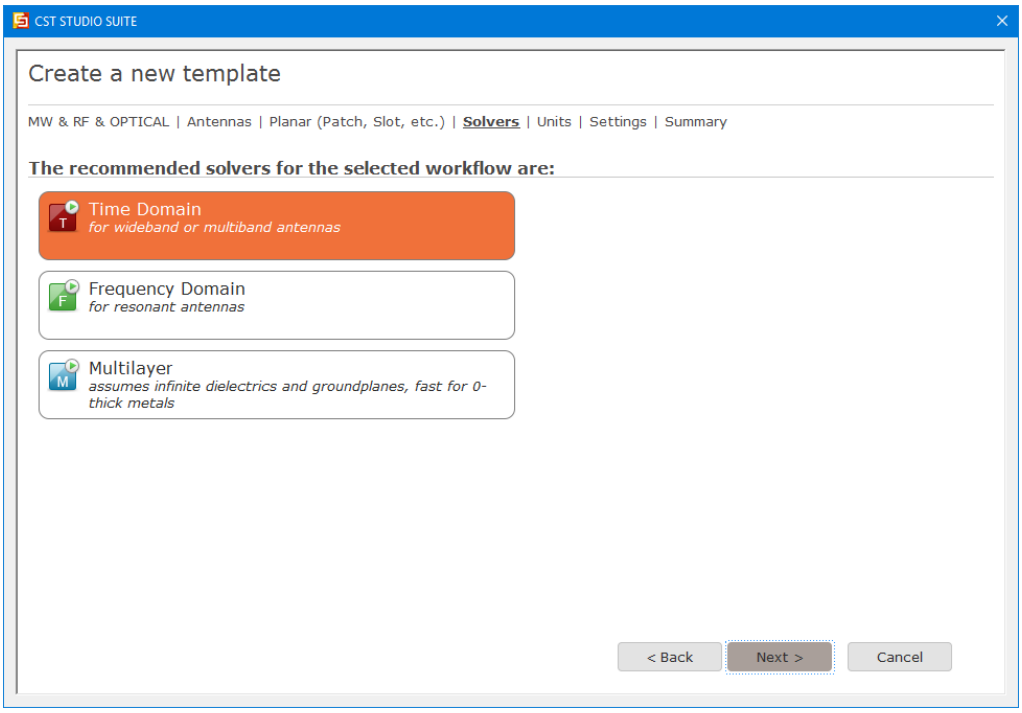

4. A new menu to select the preferred units will show up, just click Next button.

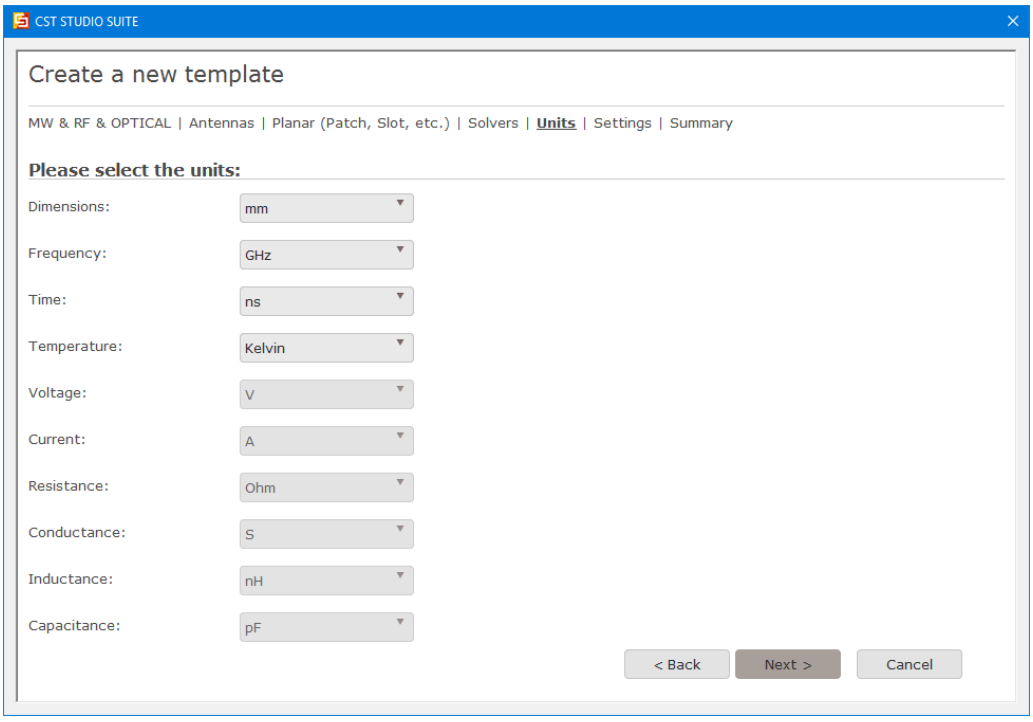

5. Choose the minimum and maximum frequency coverage for simulation. The main parameter to be monitored is the Farfield, but the user can add several available

parameters. On the last setting for the new template, define the frequency for monitoring the Farfield. In this case, because the GNSS frequencies will be monitored, so the selected frequencies are 1, 1.38, and 2 GHz are selected.

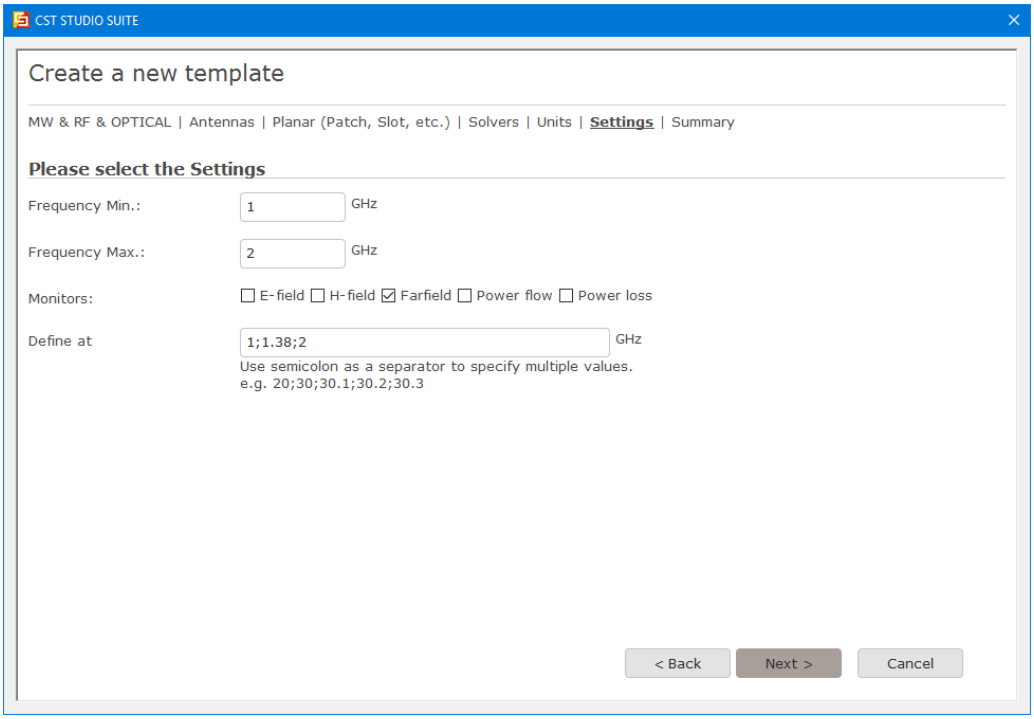

6. In the next form, give the template name, for example, Wideband GNSS, then click finish button.

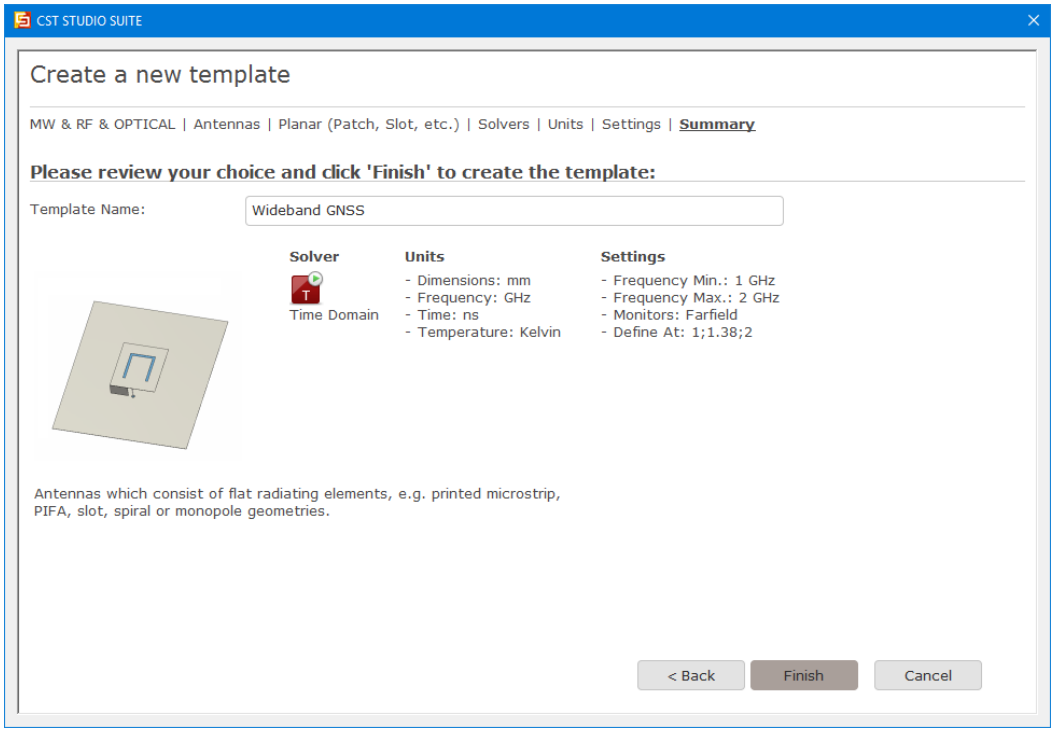

7. A new empty template will appear as following, and Save As the file into any folder and drive.

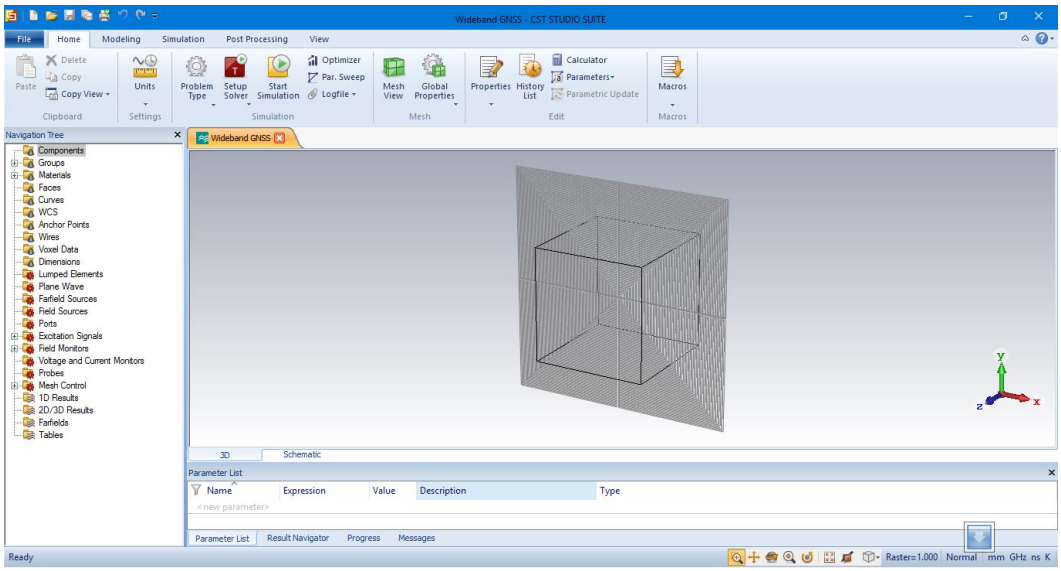

8. Create a square patch by selecting a brick button on Modelling Tab.

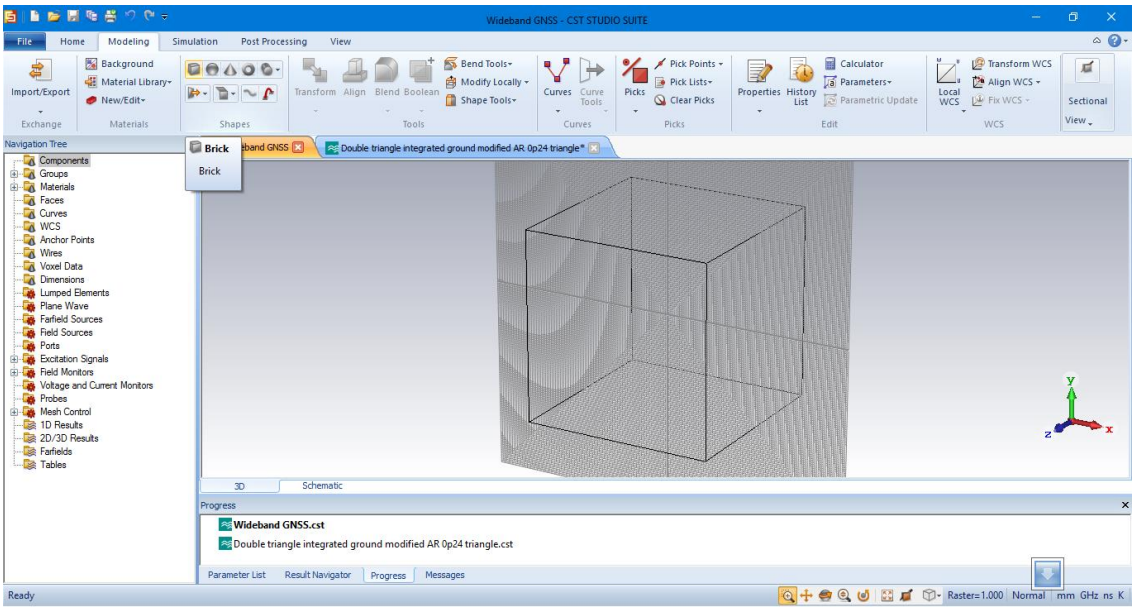

9. Then press ESC to show a dialog box as below. Fill each box in X, Y, and Z coordinates by writing (parameters) variables to draw a square box as written in the right dialog box. As for the material, select Load from Material Library option and the choose Copper (pure) from the List. Click OK button.

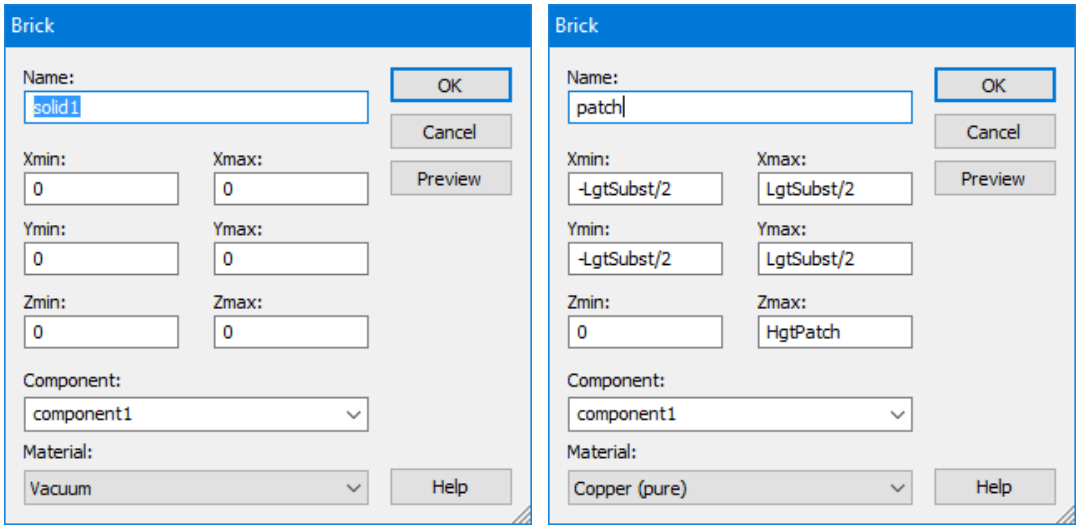

10. A New Parameter dialog box will appear to ask the value of each parameter as shown below. Put 126 for the LgtSubst, and 0.035 for HgtPatch. Click OK.

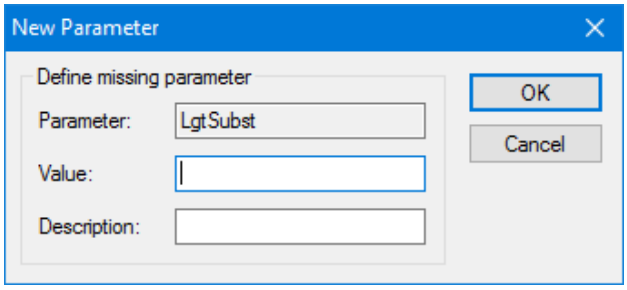

11. As a result, a square patch will appear on the 3D primary window of CST MWS. Both parameters are written also in the Parameter List below the 3D view.

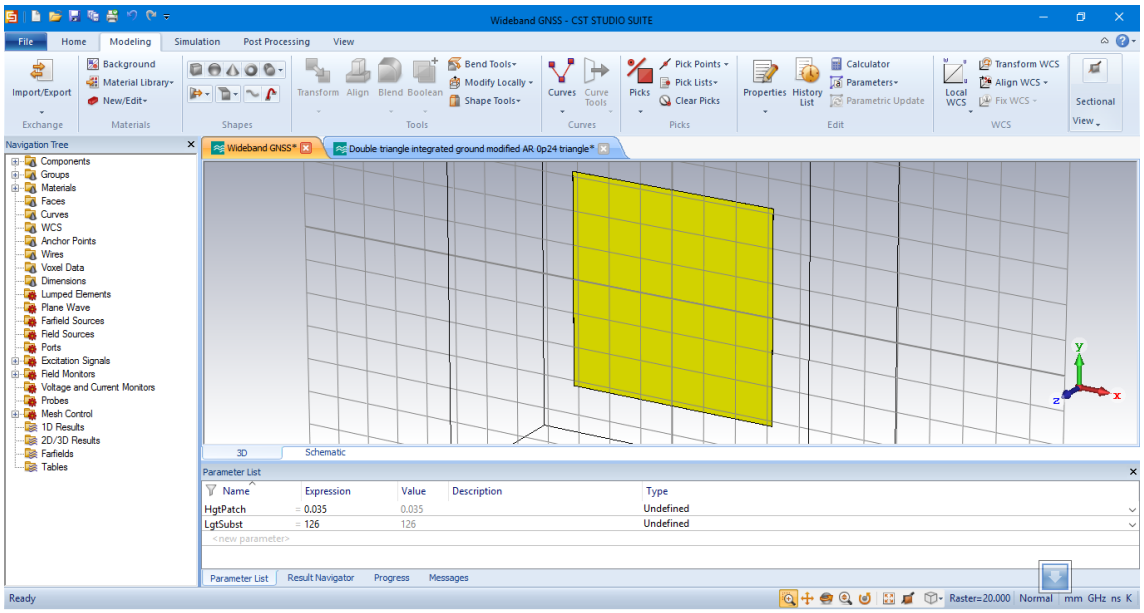

12. Click Pick Face on the Modeling Tab, then double click on the surface of the square patch. This will create many dots on the surface of the square patch as shown below.

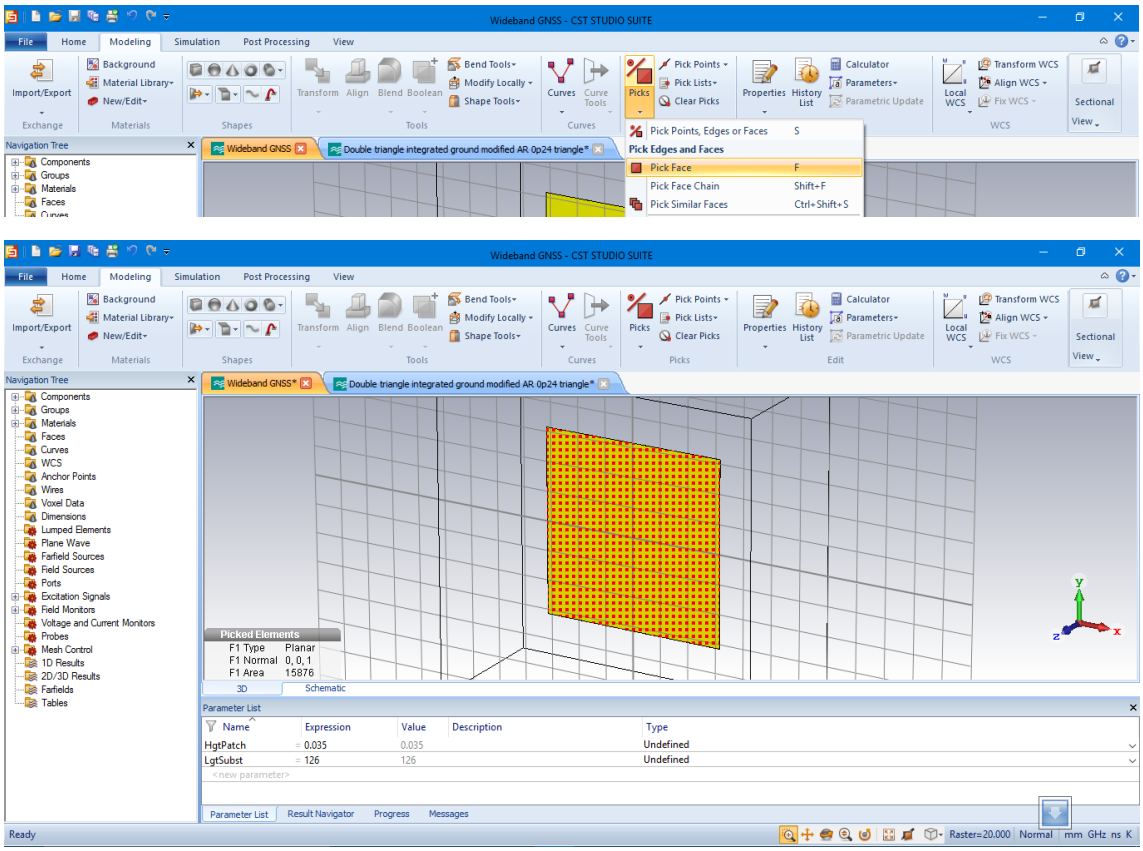

13. Click Local WCS on the Modeling Tab (as indicated by yellow menu) to create local u, v and w. This will make the center of the square patch as the reference point (0,0,0) of the local coordinate. Then click Clear Picks menu on the same tab to clear the dots on the surface.

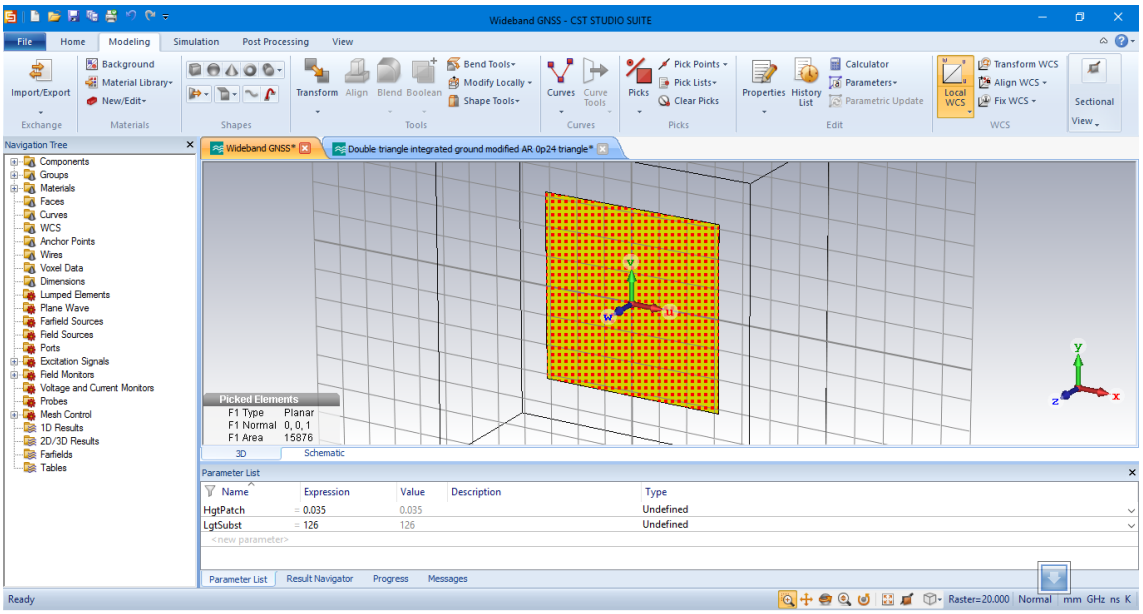

14. Click Polygon menu on Modeling tab to create a triangular shape, then press ESC button on the keyboard. The below dialog menu will appear and put the values of three u and v point to draw a triangular, for example as shown in the right dialog menu.

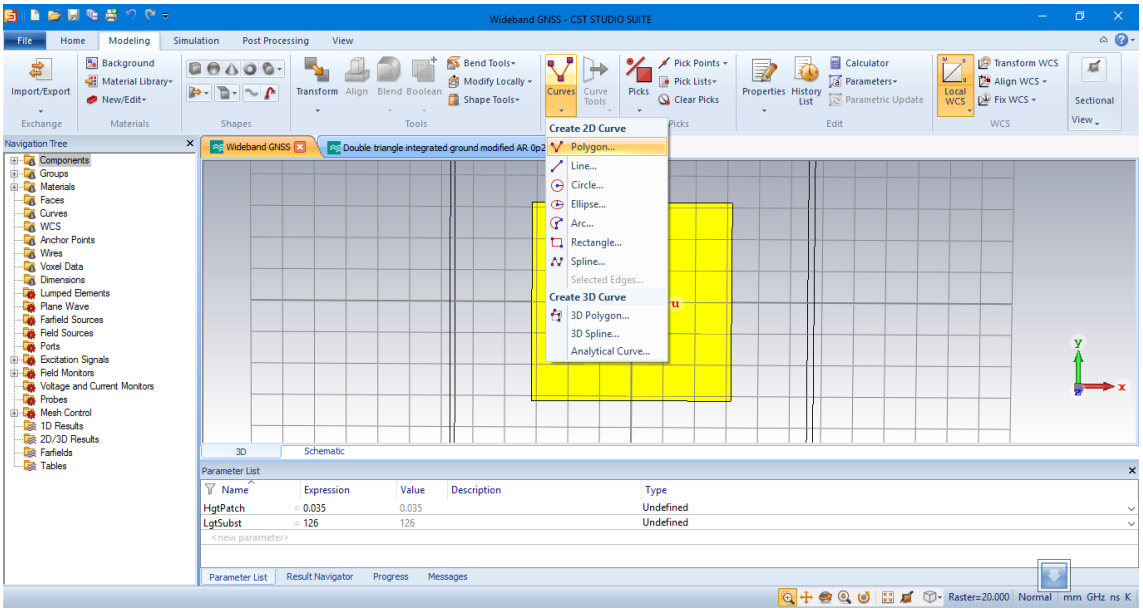

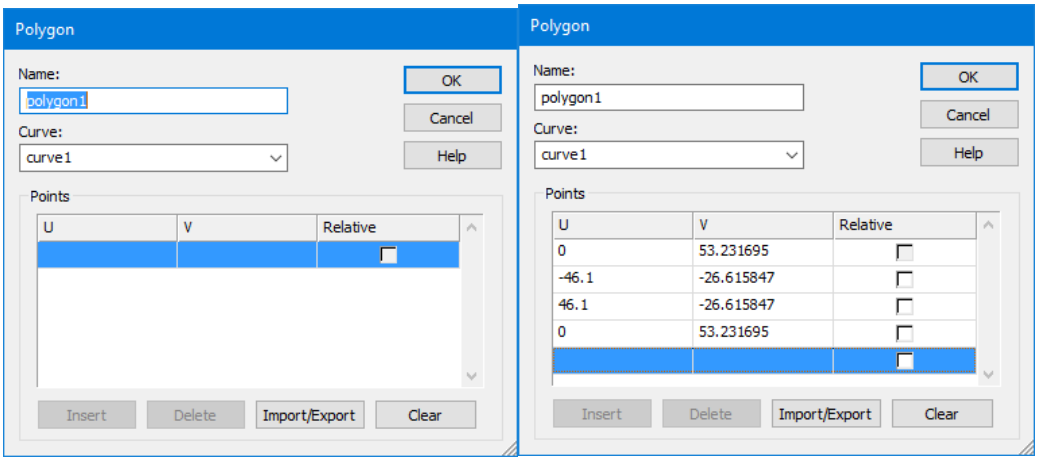

15. The result is a triangular curve. To make this curve become a solid triangular box, select Extrude Curve menu, double-click polygon1 in the curve1 located in the Navigation Tree, then press ENTER button on the keyboard.

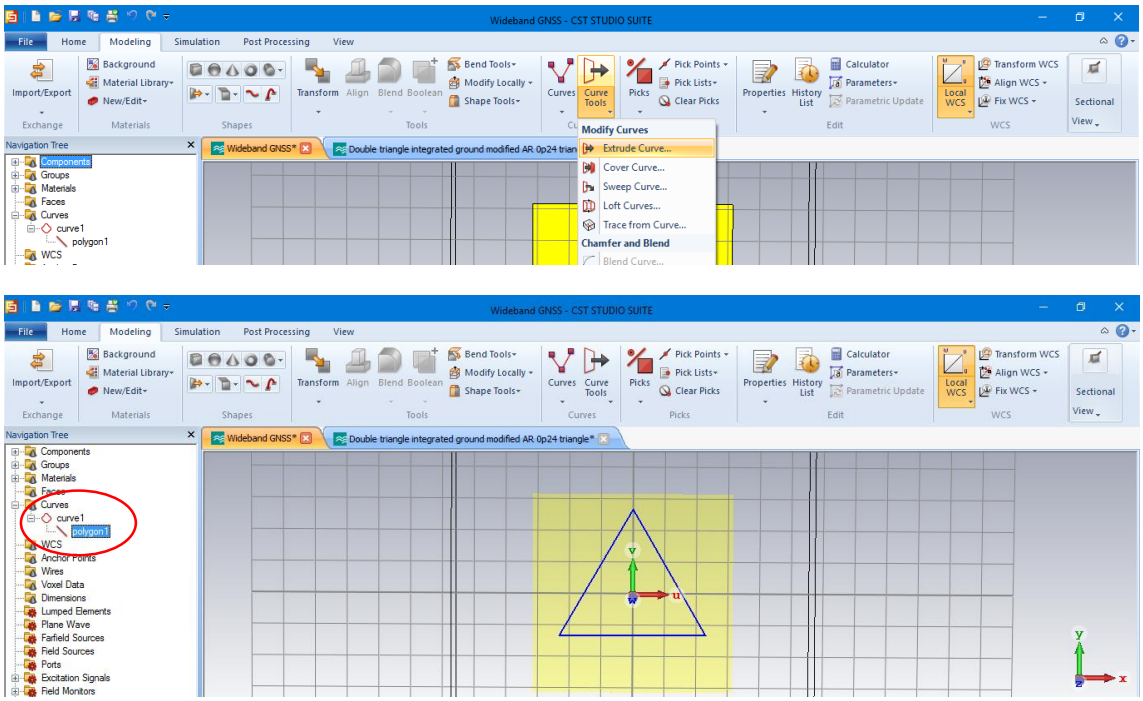

16. An Extrude Planar Curve dialog menu will appear and fill the box, for example as shown in the right dialog menu. After that, click OK button, new triangular component appears.

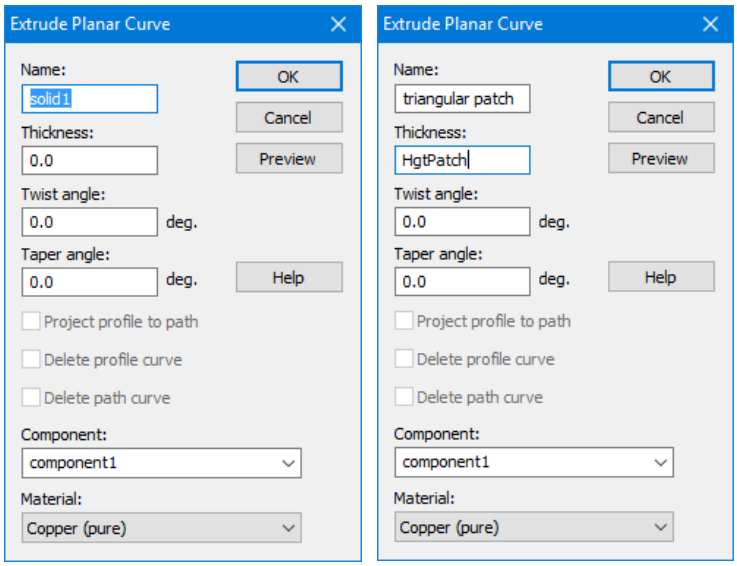

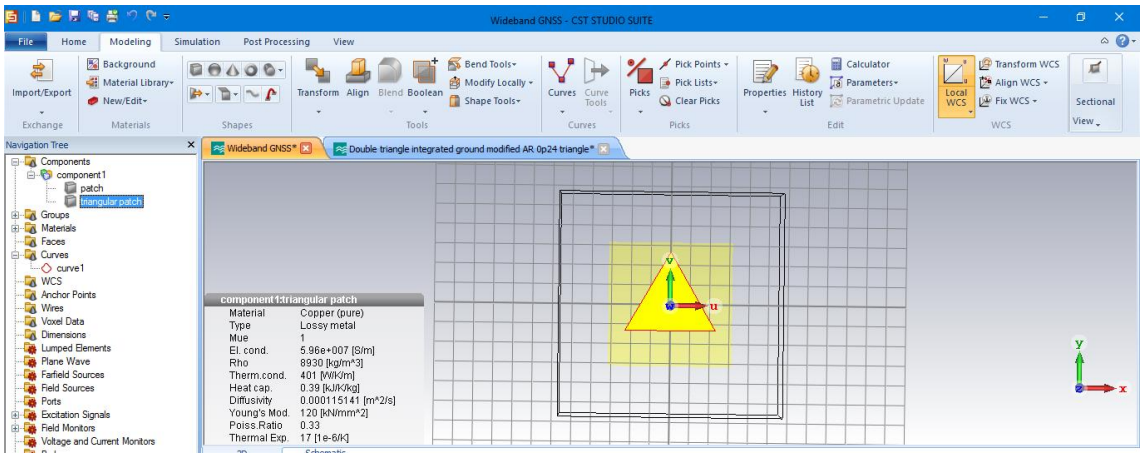

17. The next step is to create a triangular slot. For this purpose, select “patch” in component1 located in the Navigation Tree. Then click Subtract option in the Boolean menu, after that select “triangular patch” in component1 located in the Navigation Tree, and press ENTER button. A triangular slot will be created and “triangular patch” in component1 disappears as it integrated with the “patch” component.

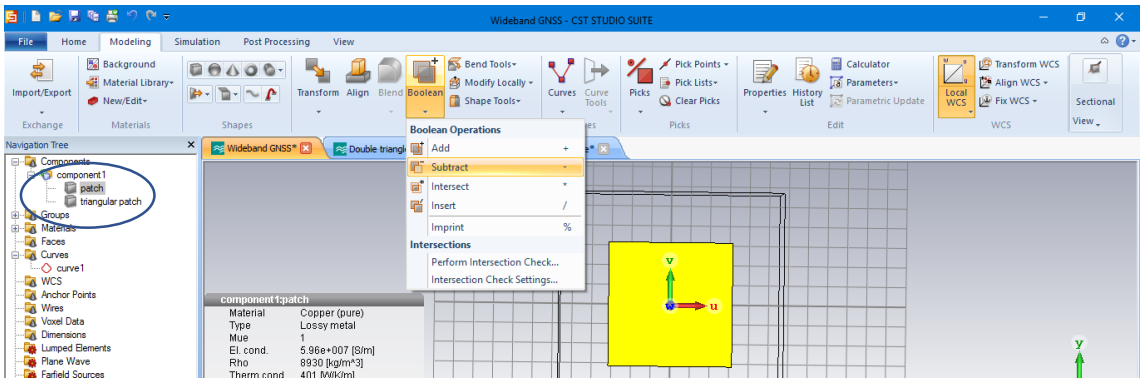

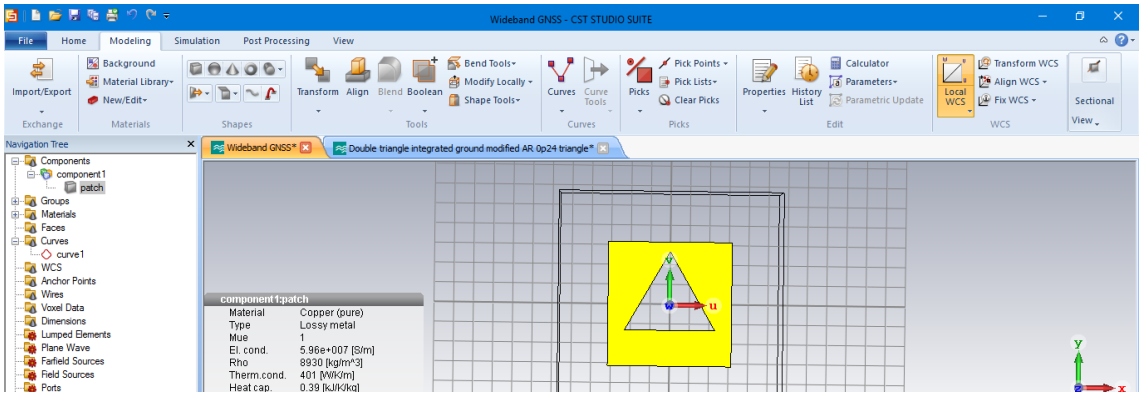

18. The triangular slot requires an inner triangular patch to create a triangular ring slot. Therefore, a new smaller triangular patch will be created in the center of the slot. For this purpose, the method is similar with the previous creation process by using Curves → Polygon menu. The values of u and v points for the triangular polygon are as follow.

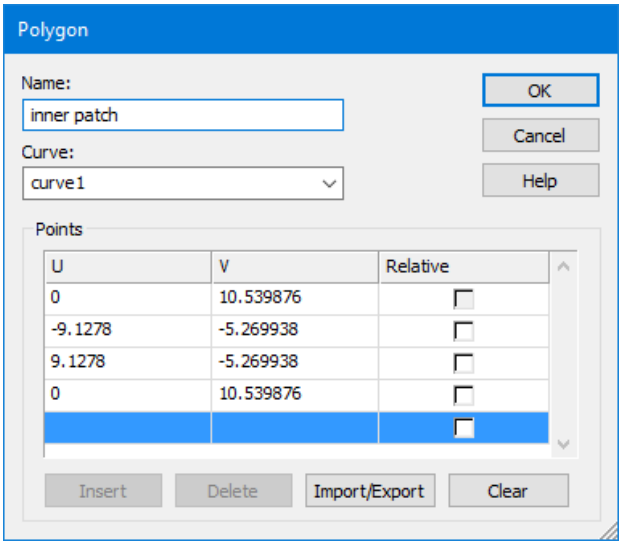

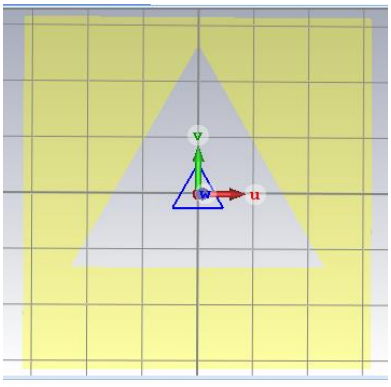

19. To change the curve become a solid component, Curve Tools → Extrude Curve menu is used and select the “inner patch” in the curve1 located in the Navigation Tree. Fill the box of Extrude Planar Curve dialog box as follow and a triangular patch will be created.

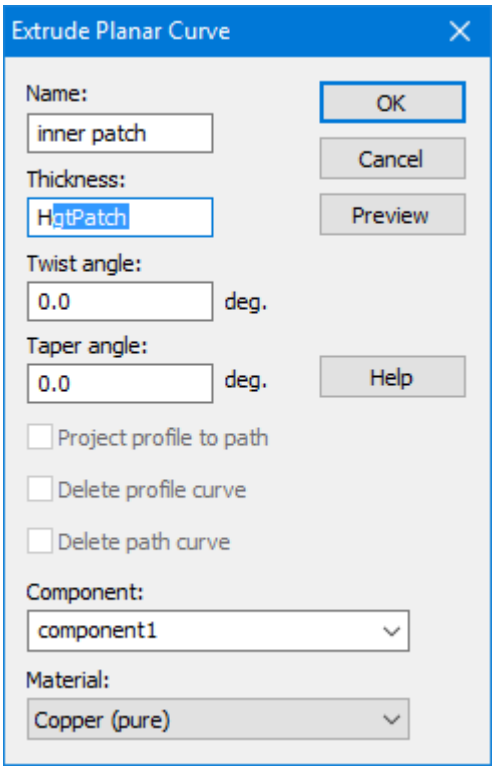

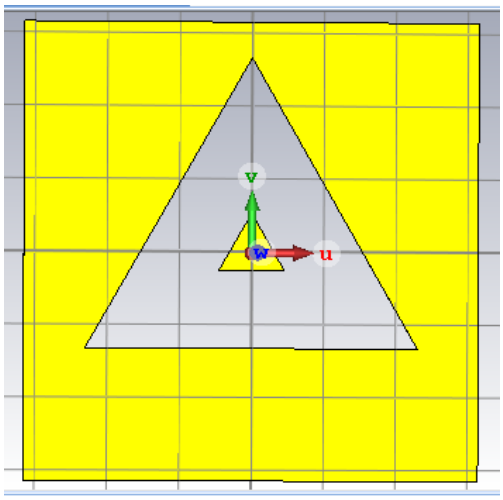

20. The equilateral triangular ring slot has been created. However, this design requires a substrate and feed line. To build a substrate, the method is similar with the patch creation by using Modeling → Brick menu. Brick dialog box will appear and fill with the values as shown by below example. The material for the substrate is NPC-H220A with thickness HgtSubst of 1.6 mm., dielectric constant of 2.17, and dissipation factor of 0.0005. The result is shown in the below CST 3D window, the substrate has a blue color.

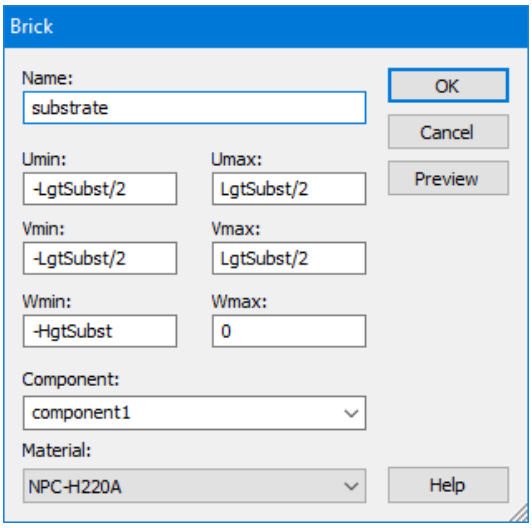

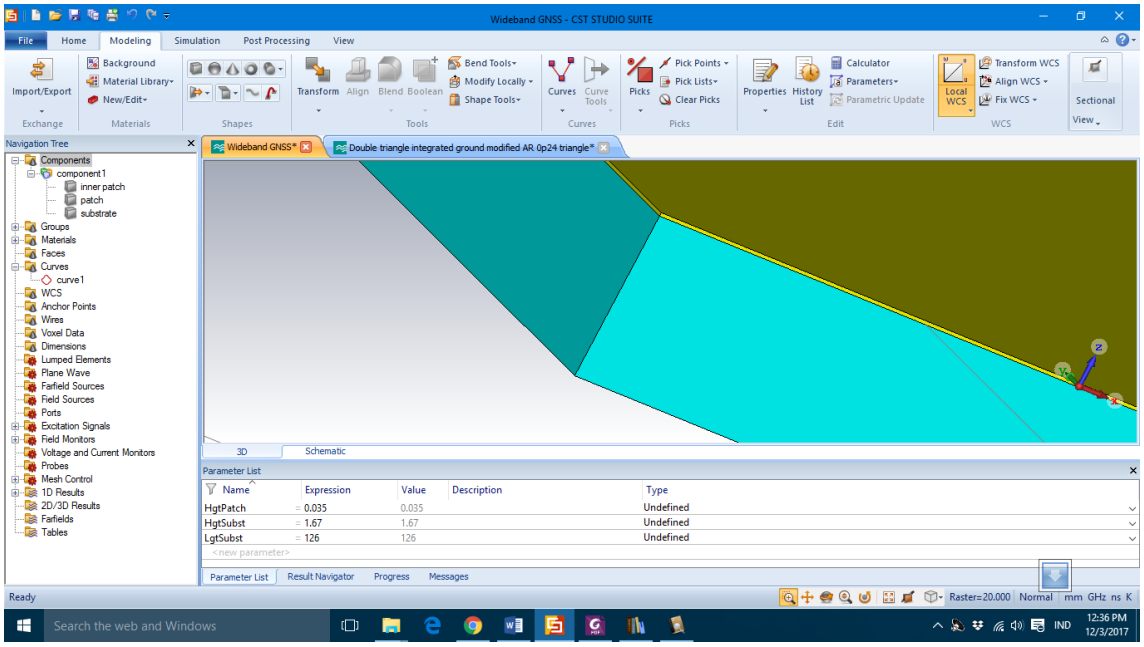

21. To build a feed line, the method is similar with the patch and substrate creation by using Modeling → Brick menu. Brick dialog box will appear and fill with the values as shown by below example. The value of Wmin is –HgtSubst-HgtPatch. The created feed line (yellow line) is located in the bottom layer and centered to the middle of the slot.

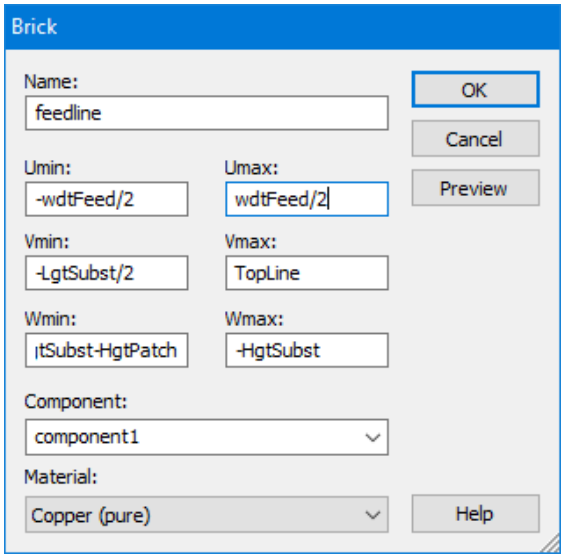

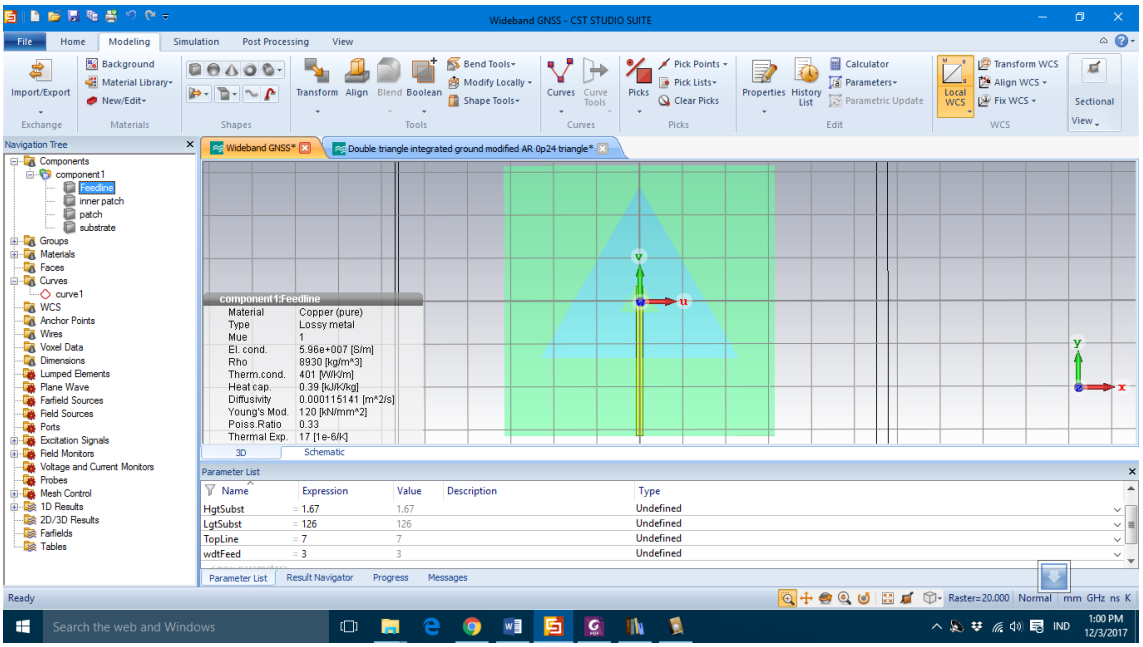

22. The design of equilateral triangular ring slot antenna has been created. To simulate the design, the antenna requires a port as a source of electromagnetic wave. To create a port, zoom the bottom part of the feed line and select Picks → Pick Face menu. Then double-click on the surface of the feed line bottom part to select the surface of the bottom part. Many red points will appear as shown below.

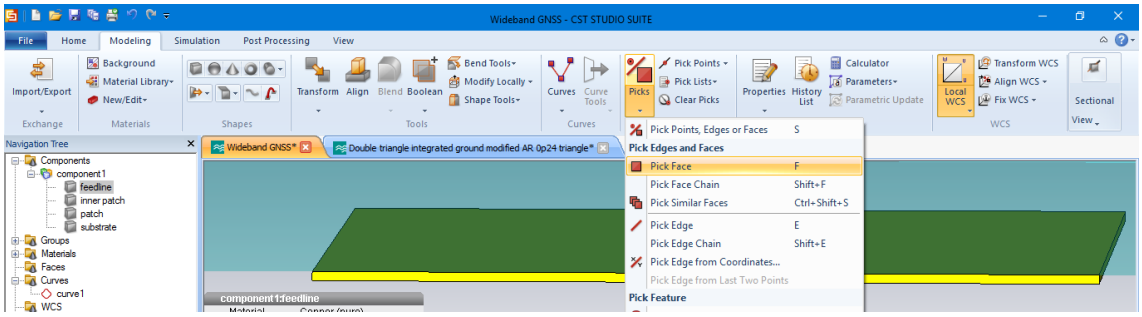

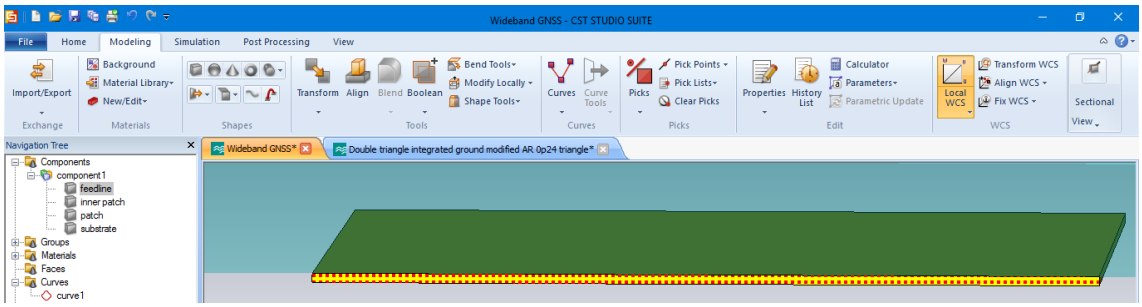

23. Select tab Home and click Macros menu. Click Solver → Ports → Calculate port extension coefficient. A dialog box of calculate port extension coefficient will show up and click Calculate button, the value of k will be calculated and shown the result. Then click Construct port from picked face. A port named port1 will appear in Ports folder in the Navigation Tree.

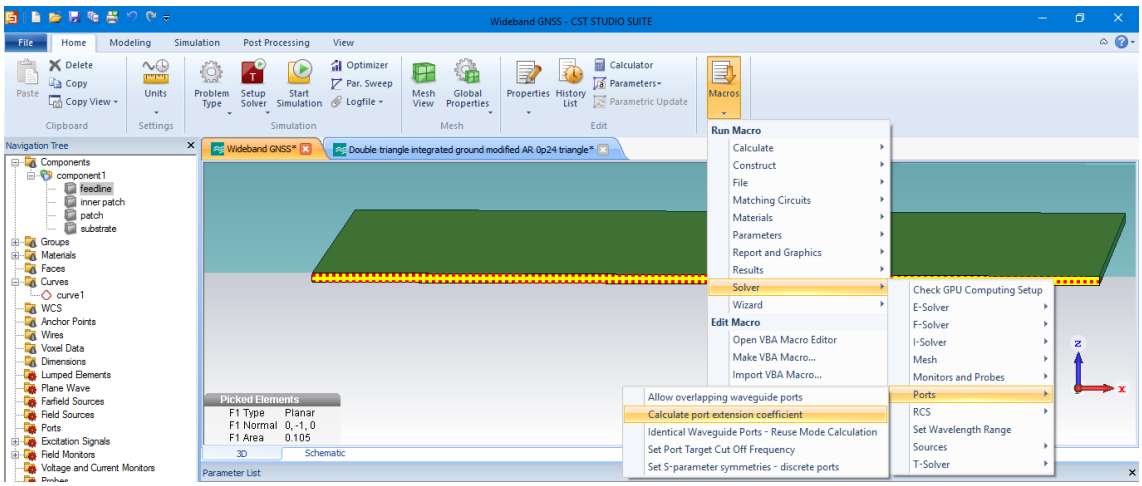

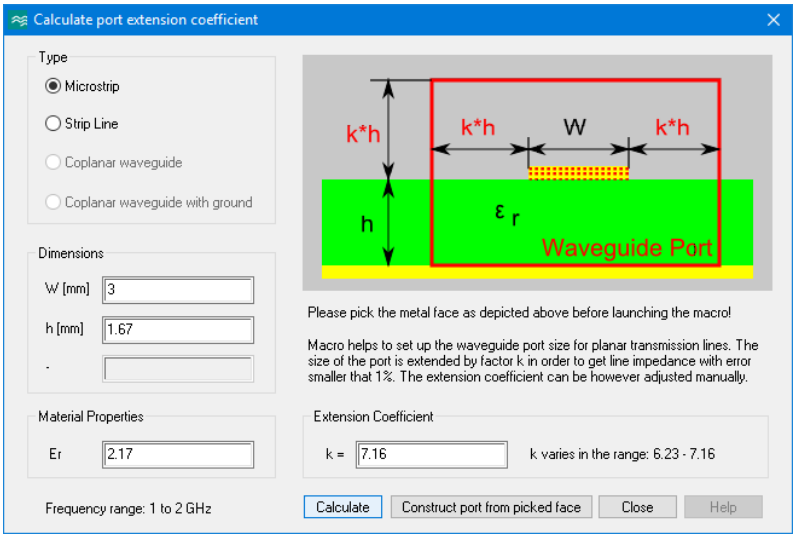

24. If the "port1" in the Ports folder is clicked, the port (red and rectangular) will appear as illustrated below. To start the simulation process, click the Start Simulation button.

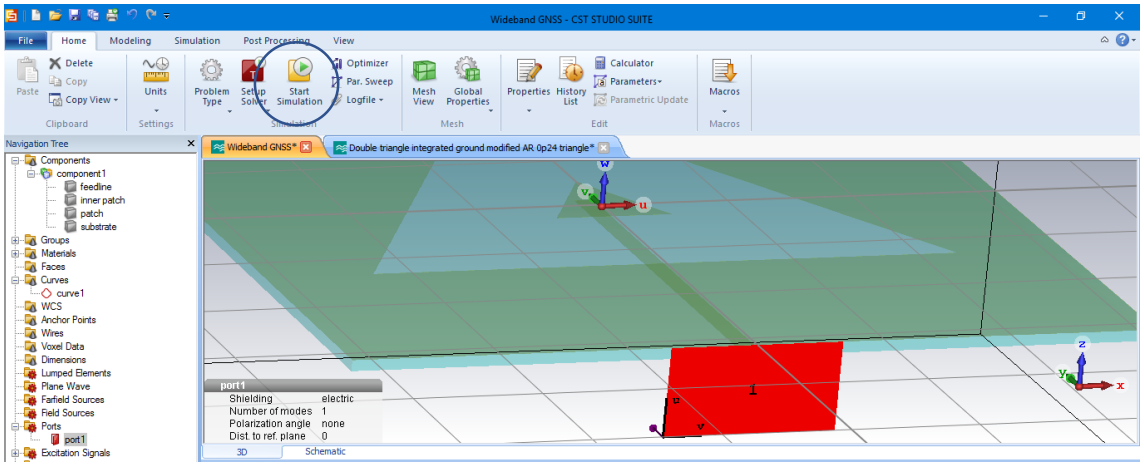

25. As the result of the simulation process, several parameter and graphs will be created. For example, the reflection coefficient (S11) graph can be shown by clicking the "S1,1" in "1D Results/S Parameters" folder located in the Navigation Tree. S11 graph shows the working frequency of the antenna which are all frequencies located ≤ 10 dB.

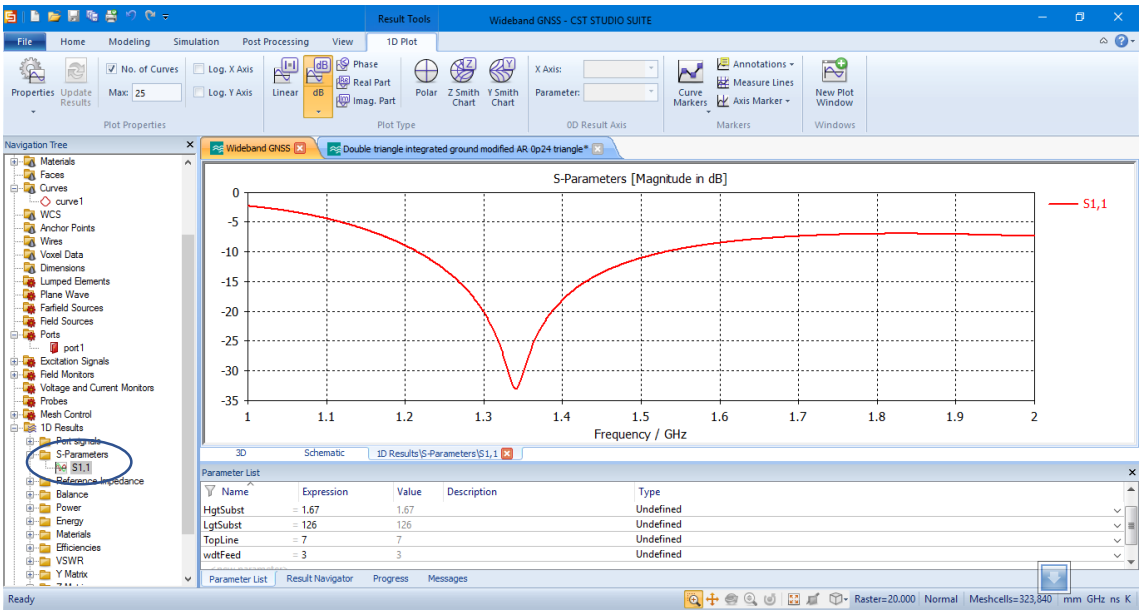
Wideband GNSS - CST STUDIO SUITE
Result Tools
File
Home
Modeling
Simulation
Post Processing
View
1D Plot
Properties
Update Results
No. of Curves
Max: 25
Log. X Axis
Log. Y Axis
Plot Properties
Linear
dB
Phase
Real Part
Imag. Part
Polar
Z Smith Chart
Y Smith Chart
Plot Type
X Axis:
Parameter:
0D Result Axis
Curve Markers
Annotations
Measure Lines
Axis Marker
Markers
New Plot Window
Windows
Navigation Tree
Materials
Faces
Curves
curve1
WCS
Anchor Points
Wires
Voxel Data
Dimensions
Lumped Elements
Plane Wave
Farfield Sources
Field Sources
Ports
port1
Excitation Signals
Field Monitors
Voltage and Current Monitors
Probes
Mesh Control
1D Results
Port signals
S-Parameters
S1,1
Reference Impedance
Balance
Power
Energy
Materials
Efficiencies
VSWR
Y Matrix
Wideband GNSS
Double triangle integrated ground modified AR 0p24 triangle*
S-Parameters [Magnitude in dB]
S1,1
0
-5
-10
-15
-20
-25
-30
-35
1
1.1
1.2
1.3
1.4
1.5
1.6
1.7
1.8
1.9
2
Frequency / GHz
3D
Schematic
1D Results\S-Parameters\S1,1
Parameter List
Name
Expression
Value
Description
Type
HgtSubst = 1.67 1.67 Undefined
LgtSubst = 126 126 Undefined
TopLine = 7 7 Undefined
wdtFeed = 3 3 Undefined
Parameter List
Result Navigator
Progress
Messages
Ready
Raster=20.000
Normal
Meshcells=323,840
mm GHz ns K